Semiconductors, Vol. 37, No. 12, 2003, pp. 1363–1366. Translated from Fizika i Tekhnika Poluprovodnikov, Vol. 37, No. 12, 2003, pp. 1409–1413.

ATOMIC STRUCTURE AND NONELECTRONIC PROPERTIES OF SEMICONDUCTORS

Redistribution of Ytterbium and Oxygen in Annealing of Silicon Layers Amorphized by Implantation

O. V. Aleksandrov*, Yu. A. Nikolaev, N. A. Sobolev**, R. Asomoza***, Yu. Kudriavtsev***, A. Villegas***, and A. Godines***

**St. Petersburg State University of Electrical Engineering, St. Petersburg, 197376 Russia*
e-mail: aleksandrov@svs.ru
***Ioffe Physicotechnical Institute, Russian Academy of Sciences, St. Petersburg, 194021 Russia*
****Seccion de Electronica del Estado Solido, Cinvestav-IPN, Av. IPN # 2508 Mexico D.F.*
Submitted April 29, 2003; accepted for publication April 30, 2003

Abstract—The redistribution of ytterbium and oxygen was studied in silicon layers that were implanted with 1-MeV Yb^+ ions at a dose of 1×10^{14} cm^{-2}, which exceeds the amorphization threshold, and 135-keV O^+ ions at a dose of 1×10^{15} cm^{-2} and that were subsequently annealed at 620 and 900°C. The redistribution of Yb is due to segregation at the interface between the amorphous and single-crystal layers in solid-phase recrystallization of the buried amorphized layer. The redistribution of oxygen and its accumulation in regions with the highest concentration of Yb is associated with oxygen diffusion and the formation of YbO_n complexes with n varying from 1 to 6. The parameters characterizing the dependence of the Yb segregation coefficient on the thickness of the recrystallized layer and the formation of YbO_n complexes were determined. © *2003 MAIK "Nauka/Interperiodica".*

1. INTRODUCTION

Admixtures of various rare-earth elements (REE) introduced into a silicon matrix make it possible to develop an element base for device structures with luminescence over a wide spectral range for the further development of silicon optoelectronics. Therefore, studying the behavior of REEs in technological processes of device fabrication is of significant interest and will in future enable one to fabricate high-efficiency light-emitting structures.

In solid-phase epitaxial (SPE) crystallization of amorphized silicon layers, the redistribution of such REE impurities as Er, Ho, and Pr occurs [1–5]. The redistribution of REE impurities Er and Ho is satisfactorily described by the model [2, 5] with a coordinate-dependent segregation coefficient determined by the conditions of REE implantation. The presence of an oxygen impurity strongly affects the REE segregation in SPE crystallization, which has a significant effect on the concentration profile. Implantation of oxygen ions into an amorphized silicon layer changes the nature of the redistribution of REE impurities and increases the rate at which the equilibrium coefficient of REE segregation increases from the initial 2×10^{-3}–2×10^{-2} to final values of 0.6–1.5 [3, 5].

The redistribution of the oxygen impurity in the annealing of silicon layers containing REE impurity Er was studied in [6]. A correlation was revealed between the concentration profiles of erbium and oxygen upon annealing, which the authors attributed to the formation of oxygen–erbium complexes. Complexes formed by Er and O impurities in implanted silicon layers have been revealed by EXAFS [7, 8], Mössbauer spectroscopy [9], and ESR spectroscopy [10]. In [11], the change in the concentration profile of oxygen coimplanted with Er was attributed to the egress of oxygen to a region with increased defectiveness, where precipitates formed. In [12], an attempt was made to calculate various atomic configurations of Er–O complexes. Photo- and electroluminescence centers in erbium-doped silicon have been related to Er–O complexes or clusters. [9, 13].

In the present study, the joint redistribution of ytterbium and oxygen impurities upon annealing of silicon layers amorphized by implantation was analyzed in order to determine their mutual influence.

2. EXPERIMENTAL

Polished Czochralski-grown *p*-type (100)Si wafers with a resistivity of 20 Ω cm were used as substrates. According to IR absorption data, the oxygen concentration in the starting silicon was ~1×10^{18} cm^{-3}. Implantation of 1 MeV Yb^+ ions was performed on a High Voltage Engineering Europe K2MV installation at a dose of 1×10^{14} cm^{-2} exceeding the amorphization threshold. O^+ ions were additionally implanted into some of the samples at a dose of 1×10^{15} cm^{-2} and energy of 135 keV, ensuring approximately the same mean projective range as that for Yb^+ ions ($Rp(O^+)$ = 0.39 μm, $Rp(Yb^+)$ = 0.33 μm). Two-stage annealing was performed at 620°C for 1 h and at 900°C for 30 min

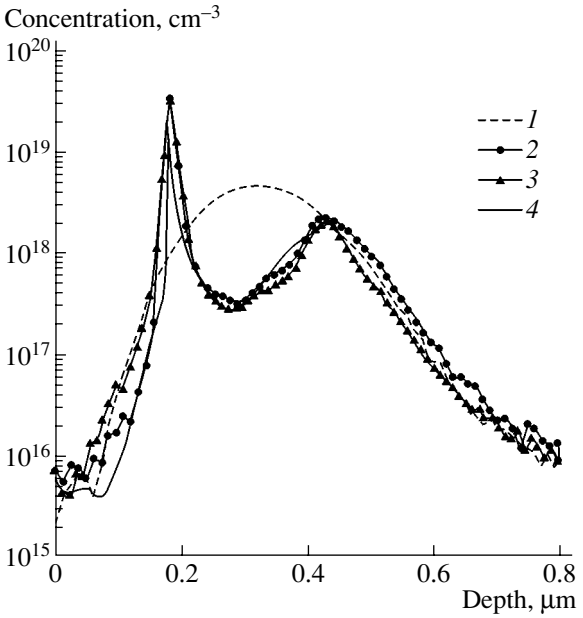

Fig. 1. Yb concentration profiles after (*1*) implantation of Yb^+ ions, (*2*) annealing at 620°C, and (*3*) additional annealing at 900°C; (*4*) calculation for $L_1 = 23$ nm, $L_2 = 70$ nm, $l_1 = 30$ nm, $l_2 = 27$ nm, $K_0 = 2 \times 10^{-3}$, and $K_m = 1.3$.

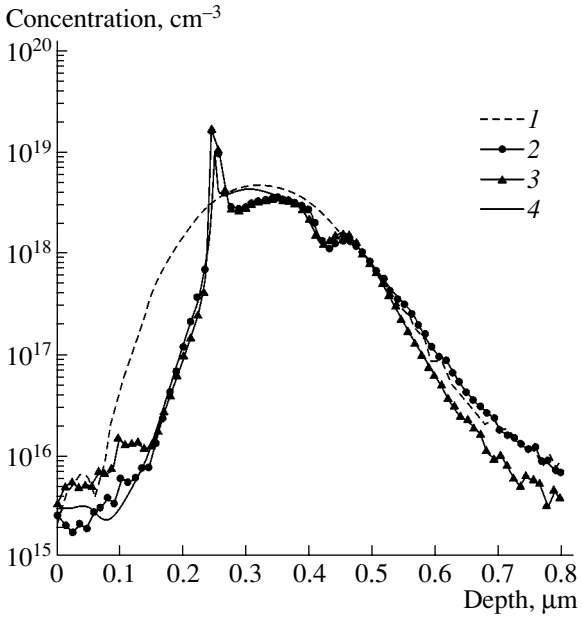

Fig. 2. Yb concentration profiles after (*1*) joint implantation of Yb^+ and O^+ ions, (*2*) annealing at 620°C, and (*3*) additional annealing at 900°C; (*4*) calculation for $L_1 = 40$ nm, $L_2 = 9$ nm, $l_1 = 27$ nm, $l_2 = 12$ nm, $K_0 = 2 \times 10^{-3}$, and $K_m = 0.6$.

in a chlorine-containing atmosphere. The distribution of ytterbium and oxygen across the sample thickness was determined by secondary ion mass spectrometry (SIMS) on a Cameca IMS 6f installation.

3. EXPERIMENTAL RESULTS AND DISCUSSION

3.1. Redistribution of Ytterbium

At the Yb^+ implantation dose of 1×10^{14} cm^{-2} used in the study, as well as in the case of Er [4], a buried amorphized layer is formed. The concentration profiles obtained after implantation of Yb^+ ions and subsequent annealing at 620°C are shown in Fig. 1 (curves *1*, *2*). It can be seen that thermal treatment gives rise to a sharp Yb peak at a depth of $x_m = 0.18$ μm, which is due to segregation of Yb at crystallization fronts moving toward each other from the initial boundaries of the buried *a* layer, $x_{a1} \approx 0.08$ and $x_{a2} \approx 0.43$ μm. The Yb concentration profiles in the case of joint implantation of Yb^+ and O^+ ions before and after annealing at 620°C are shown in Fig. 2 (curves *1*, *2*). In this case, the change in the Yb concentration profile and the appearance of a peak at a depth $x_{n1} = 0.25$ μm upon annealing is also due to Yb segregation at crystallization fronts moving toward each other from the initial boundaries of the buried *a*-layer at $x_{a1} \approx 0.05$ and $x_{a2} \approx 0.46$ μm. It is noteworthy that, in the case of joint implantation of Yb^+ and O^+ ions, the peak position x_m is shifted deeper inside the sample as compared with the implantation of Yb only (from 0.18 to 0.25 μm). This may indicate a slower rate of crystallization of the lower part of the *a* layer, which is more heavily doped with oxygen. In both cases, subsequent annealing at 900°C does not lead to any further change in the Yb profile (Figs. 1, 2, curves *3*).

The redistribution of the impurity Yb will be described, as was done previously for REE impurities Er and Ho [2, 5], by the dependence of the effective (K_{ef}) and equilibrium (K_{eq}) segregation coefficients on the thickness W of the crystallized layer:

$$K_{ef}(W) = C/C_a = (b + K_{eq}h/V)/(1 + h/U), \quad (1)$$

$$K_{eq}(W) = K_0K_m/[K_0 + (K_m - K_0)\exp(-W/L)], \quad (2)$$

where C and C_a are the concentrations of the REE impurity at the interface in the single-crystal *c*-Si and amorphized *a*-Si, respectively; b, the ratio of the atomic volumes of *a*- and *c*-Si ($b = 1.027$); U, the rate of SPE crystallization; h, the mass-transfer coefficient, $h(W) = h_0\exp(W/l)$, where h_0 is the initial value of the mass-transfer coefficient, and l is the characteristic length of the rise in h; K_0 and K_m, the initial and final values of the segregation coefficient; and L, the thickness of the transition layer or the characteristic length of the rise in K_{eq}.

The calculated concentration profiles for separate implantation of Yb^+ ions and joint implantation with O^+ ions are shown in Figs. 1 and 2 (curves *4*). The obtained parameters characterizing the coordinate dependence of the segregation coefficient and mass-transfer rate, which are given in the figure captions, are approximately equal to those previously determined by the authors for REE impurities Er and Ho [3–5]. In joint implantation with O^+ ions, the thickness of the transition layer (in the case in question, parameter L_2 corresponding to the lower part of the amorphized layer with

the maximum concentration of oxygen) decreases from 70 to 9 nm (for REE impurities Er and Ho, L decreases from 40–70 to 13–20 nm [3–5]).

3.2. Redistribution of Oxygen

When silicon implanted with Yb^+ ions is annealed, a change in the oxygen distribution is observed both for oxygen present in the substrate (Fig. 3, curves *1*, *2*) and for that implanted additionally (Fig. 4, curves *1–3*). In both these cases, the SIMS signal of oxygen increases in places with the highest Yb concentration: in the vicinity of the Yb concentration peak at x_m and near the lower initial boundary of the *a* layer at x_{a2}. Accumulation of oxygen occurs even at 620°C and becomes more pronounced upon subsequent annealing at 900°C, which is clearly seen from the SIMS profiles of oxygen in Figs. 3 (curves *1*, *2*) and 4 (curves *2*, *3*).

The redistribution of the oxygen impurity, which is observed upon annealing, may be attributed to the relatively high mobility of oxygen atoms at the annealing temperature (diffusion coefficient of oxygen in silicon, $D_{ox} = 7 \times 10^{-16}$ cm^2/s at 620°C and $D_{ox} = 2 \times 10^{-12}$ cm^2/s at 900°C [14]), while the accumulation of oxygen in regions with the highest Yb concentration may be related to the binding of mobile O atoms to immobile Yb atoms via complexation. The maximum number of oxygen atoms that can be bound by an REE atom into a complex is six for REE Er [7, 8]. Therefore, it is assumed in modeling the oxygen redistribution that Yb–O complexes have the composition YbO_n, with n varying from one to six. It is also assumed that more composite complexes are formed from simpler ones via subsequent addition of an oxygen atom by the reaction

$$YbO_{n-1} + O \longleftrightarrow YbO_n, \quad (3)$$

where n = 1–6. According to [15], the rate of solid-phase crystallization is ~2.7×10^{-3} μm/s at 620°C. Therefore, a 0.45-μm-thick *a* layer crystallizes in a much shorter time than that taken for the annealing; i.e., the redistribution of oxygen mainly occurs after recrystallization of the *a* layer, when the Yb concentration profile is already formed. Diffusion-kinetic equations taking into account the diffusion of oxygen to immobile ytterbium atoms to form complexes by reaction (3) have the form

$$\frac{\partial C_{ox}}{\partial t} = D_{ox}\frac{\partial^2 C_{ox}}{\partial x^2} - \sum_n (k_{fn} C_{ox} C_{kn-1} - k_{rn} C_{kn}), \quad (4)$$

$$\frac{\partial C_{kn}}{\partial t} = k_{fn} C_{ox} C_{kn-1} - k_{rn} C_{kn} - k_{fn+1} C_{ox} C_{kn} + k_{rn+1} C_{kn+1}, \quad (5)$$

where t is the annealing time; x, the depth; C_{ox}, the concentration of unbound oxygen; C, that of unbound Yb; k_{fn}, the rate constants of forward reactions of complexation; k_{rn}, those of reverse reactions of decomplexation; C_{kn}, the concentration of YbO_n complexes; n, the number of oxygen atoms in the complexes; and n = 1–6 ($C_{k0} = C$). In the first approximation, the following is assumed: the rate constants of forward and reverse reactions are equal for all values of n; $k_{fn} = k_f = 4\pi r D_{ox}$, where r is the radius of oxygen atom capture by the complex; $k_{rn} = k_r = \nu \exp(-(E_b + E_m)/kT)$, where ν is the frequency of atomic vibrations in the lattice of silicon, $\nu \approx 10^{13}$ s^{-1}; E_b, the binding energy; E_m, the migration

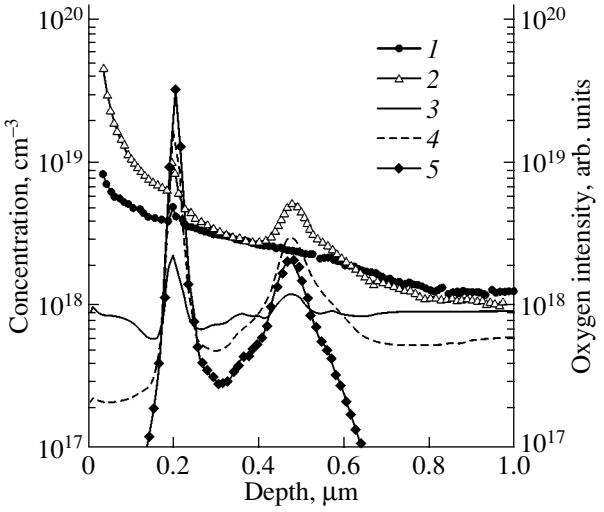

Fig. 3. Distribution of (*1*, *2*) SIMS signal intensity for oxygen and concentrations of (*3*, *4*) oxygen and (*5*) Yb after implantation of Yb^+ ions, (*1*, *3*, *5*) annealing at 620°C, and (*2*, *4*) additional annealing at 900°C; (*3*, *4*) calculation.

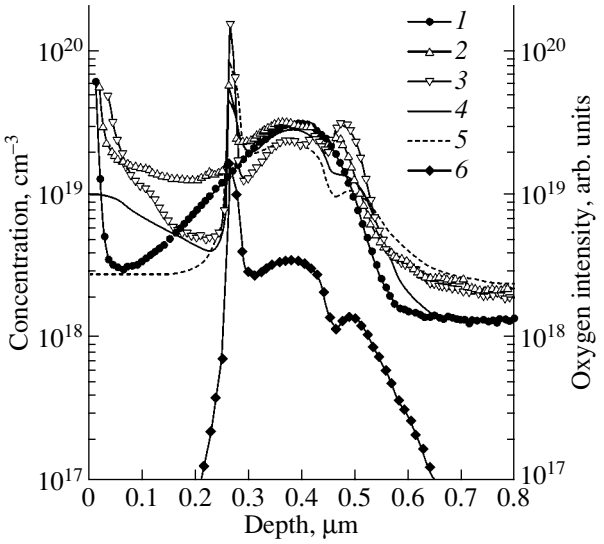

Fig. 4. Distribution of concentrations of (*1*, *4*, *5*) oxygen and (*6*) yttrium and (*2*, *3*) SIMS signal intensity for oxygen after (*1*) joint implantation of Yb^+ and O^+ ions, (*2*, *4*, *6*) annealing at 620°C, and (*3*, *5*) additional annealing at 900°C; (*4*, *5*) calculation.

energy of oxygen atoms; and k, the Boltzmann constant.

The desired parameters of the problem are r and E_b. One more parameter is the acceleration of oxygen diffusion as a result of the appearance of excess intrinsic point defects that are formed during the annealing of implantation-induced lattice disturbances. Equations (4) and (5) were solved numerically by the finite-difference method with the use of an implicit difference scheme. The results of calculations of oxygen redistribution in annealing are shown in Figs. 3 (curves *3*, *4*) and 4 (curves *4*, *5*) for $r = 4a$ (where a is the lattice constant of silicon, $a = 2.35$ Å) and $E_b = 0.4$ eV. The oxygen diffusion acceleration factor was found to be 8 at 620°C and 1 at 900°C. As can be seen in Figs. 3 and 4, the calculation describes, satisfactorily at x_m and less so at x_{a2}, the redistribution of the background oxygen contained in the silicon substrate (Fig. 3) and that of the implanted oxygen (Fig. 4), which lead to oxygen accumulation in places with the highest concentration of Yb. Presumably, oxygen atoms are captured in the vicinity of x_{a2} not only by Yb atoms, but also by the so-called end-of-range defects [16, 17]. As the annealing temperature increases from 620 to 900°C, the effect of oxygen accumulation in complexes becomes more pronounced. The results of calculations suggest that oxygen mainly accumulates in YbO_1 ($n = 1$) complexes in samples without additional implantation of O^+ ions and mainly in YbO_6 ($n = 6$) complexes in samples with coimplanted O^+ ions. It is noteworthy that, at 620°C, the characteristic decay time of the complexes, $\tau = 1/k_r \approx 2.3$ h, exceeds the duration of annealing, and oxygen capture into the complexes predominates. At the same time, the characteristic decay time of the complexes at 900°C, $\tau \approx 1$ s, is shorter than the duration of annealing, and the process of complexation becomes equilibrium.

4. CONCLUSION

A study of the redistribution of Yb and O impurities in the annealing of silicon layers amorphized by ion implantation demonstrated that the behavior of the REE impurity Yb both in the implantation of Yb ions only and in its coimplantation with oxygen ions is similar to that of the other REE impurities Er and Ho and is described by the model reported in [2, 5], with about the same parameters of the coordinate dependence of the segregation coefficient. The redistribution of the oxygen impurity and the accumulation of oxygen in the region with the highest REE concentration is due to the diffusion of oxygen atoms to immobile Yb atoms to form YbO_n complexes with $n = 1$–6. The oxygen redistribution was modeled on the assumption that the rate constants of the forward and reverse reactions are equal for complexes of different compositions ($k_{fn} = k_f$ and $k_{rn} = k_r$ at all n), and the parameters of complexation ($r = 4a$, $E_b = 0.4$ eV) were determined. It was shown that oxygen mainly accumulates in YbO_1 ($n = 1$) complexes in samples without additional implantation of O^+ ions and in YbO_6 ($n = 6$) complexes in samples with coimplanted O^+ ions.

ACKNOWLEDGMENTS

This study was supported in part by INTAS (grant no. 01-0194).

REFERENCES

1. J. S. Custer, A. Polman, and H. M. Pinxteren, J. Appl. Phys. **75**, 2809 (1994).
2. O. V. Aleksandrov, Yu. V. Nikolaev, and N. N. Sobolev, Fiz. Tekh. Poluprovodn. (St. Petersburg) **32**, 1420 (1998) [Semiconductors **32**, 1266 (1998)].
3. O. V. Aleksandrov, Yu. V. Nikolaev, and N. N. Sobolev, Fiz. Tekh. Poluprovodn. (St. Petersburg) **33**, 114 (1999) [Semiconductors **33**, 101 (1999)].
4. O. V. Aleksandrov, Yu. V. Nikolaev, N. N. Sobolev, *et al.*, Fiz. Tekh. Poluprovodn. (St. Petersburg) **33**, 652 (1999) [Semiconductors **33**, 606 (1999)].
5. O. V. Aleksandrov, Yu. V. Nikolaev, and N. N. Sobolev, Fiz. Tekh. Poluprovodn. (St. Petersburg) **34**, 3 (2000) [Semiconductors **34**, 1 (2000)].
6. P. N. Favenec, H. L'Haridon, D. Mountonnet, *et al.*, Jpn. J. Appl. Phys. **29**, L524 (1990).
7. D. L. Adler, D. C. Jacobson, D. J. Eaglesham, *et al.*, Appl. Phys. Lett. **61**, 2181 (1992).
8. A. Terrasi, G. Franzo, S. Coffa, *et al.*, Appl. Phys. Lett. **70**, 1712 (1997).
9. V. F. Masterov, F. S. Nasredinov, P. P. Seregin, *et al.*, Fiz. Tekh. Poluprovodn. (St. Petersburg) **32**, 708 (1998) [Semiconductors **32**, 636 (1998)].
10. J. D. Carrey, R. C. Barklie, J. F. Donegan, *et al.*, Phys. Rev. B **59**, 2773 (1999).
11. X. Duan, J. Palm, B. Zheng, *et al.*, Mater. Res. Soc. Symp. Proc. **422**, 249 (1997).
12. M. Hashimoto, A. Yanaza, H. Harima, and H. Katayama-Yoshida, Physica B (Amsterdam) **308–310**, 378 (2001).
13. J. Michel, L. V. Assali, M. T. Morse, and L. C. Kimerling, Semicond. Semimet. **49**, 111 (1998).
14. R. A. Devine, D. Mathiot, W. L. Warren, and B. Asper, J. Appl. Phys. **79**, 2302 (1996).
15. G. L. Olson and J. A. Roth, in *Handbook of Crystal Growth*, Ed. by D. T. J. Hurle (North-Holland, Amsterdam, 1994), Vol. 3, Chap. 7, p. 257.
16. V. I. Vdovin, T. G. Yugova, N. A. Sobolev, *et al.*, Nucl. Instrum. Methods Phys. Res. B **147**, 116 (1999).
17. R. N. Kyutt, N. A. Sobolev, Yu. A. Nikolaev, and V. I. Vdovin, Nucl. Instrum. Methods Phys. Res. B **173**, 319 (2001).

Translated by M. Tagirdzhanov

Semiconductors, Vol. 37, No. 12, 2003, pp. 1367–1372. Translated from Fizika i Tekhnika Poluprovodnikov, Vol. 37, No. 12, 2003, pp. 1414–1419.

ELECTRONIC AND OPTICAL PROPERTIES OF SEMICONDUCTORS

Two-Electron Tin Centers Formed in Lead Chalcogenides as a Result of Nuclear Transmutations

S. A. Nemov*, P. P. Seregin*, Yu. V. Kozhanova*, and N. P. Seregin**

**St. Petersburg State Polytechnical University, ul. Politekhnicheskaya 29, St. Petersburg, 195251 Russia*

***Institute of Analytical Instrumentation, Russian Academy of Sciences, Rizhskiĭ pr. 26, St. Petersburg, 198103 Russia*

Submitted April 9, 2003; accepted for publication April 21, 2003

Abstract—It is shown that the emission [^{119mm}Sn(^{119m}Sn)] and absorption (^{119}Sn) Mössbauer spectra of impurity tin atoms in lead chalcogenides are identical. It is assumed that the mechanism of emergence of multicharged tin ions as a result of conversion isomeric transition in the parent ^{119mm}Sn atom is valid only for free atoms, whereas the final charge state of a stabilized daughter atom in condensed media with a high concentration of charge carriers is the charge state of the parent atom. The large value of recoil energy for ^{119}Sb atoms after radioactive decay of parent ^{119m}Te atoms gives rise to a significant number of displaced ^{119m}Sn atoms; however, a greater fraction of ^{119m}Sn atoms after the ^{119m}Te $\longrightarrow$ ^{119}Sb $\longrightarrow$ ^{119m}Sn decay remains in the anionic sublattice and are antisite defects. In contrast to tin atoms in the cationic sublattice, the ^{119m}Sn antisite defects are found to be electrically inactive centers. © *2003 MAIK "Nauka/Interperiodica".*

1. INTRODUCTION

Mössbauer spectroscopy was found to be an efficient method for identifying two-electron tin centers with negative correlation energy in lead chalcogenides (PbS, PbSe). The parameters of ^{119}Sn Mössbauer spectra made it possible to determine the charge state of impurity atoms, their electronic structure, and the symmetry of the local surroundings [1]. It has been shown that the charge state of tin impurity atoms in PbS and PbSe depends on the position of the level of chemical potential in the semiconductor band gap; neutral $[Sn]^0$ and ionized $[Sn]^{2+}$ impurity centers were identified [1]. Mössbauer spectroscopy also made it possible to study the processes of electron exchange between the neutral and ionized tin impurity atoms in partially compensated PbSe.

It was shown that the electron-exchange rate increases with increasing temperature and is independent of the tin-center concentration; it was also shown that the exchange involved the simultaneous transfer of two electrons [2].

All the above studies were performed in the absorption mode of Mössbauer spectroscopy, in which case the material under investigation contained the stable isotope ^{119}Sn. The ultimate sensitivity of the absorption Mössbauer spectroscopy with respect to the concentration of the isotope ^{119}Sn in lead chalcogenides is no higher than 1 at %. However, as was assumed in a number of previous studies, the most drastic changes in the energy spectrum of impurity atoms occurred at a tin content of ≤0.5 at % [3].

Taking the above into account, it is preferable to use the emission mode of Mössbauer spectroscopy in studying the state of tin impurity atoms; in this case, the material under investigation contains a radioactive parent isotope after radioactive decay of which the daughter ^{119m}Sn atom comes into existence. The sensitivity of emission Mössbauer spectroscopy is controlled by the specific activity of the radioactive specimen of the parent isotope and may be as high as ~10^{-5} at %.

In this study, the potentialities of emission Mössbauer spectroscopy based on the isotope ^{119m}Sn with ^{119mm}Sn, ^{119}Sb, and ^{119m}Te parent atoms are used to identify the neutral and ionized states of tin impurity atoms, which introduce two-electron levels in the band gap of lead chalcogenides. The scheme of decay of the parent ^{119mm}Sn, ^{119}Sb, and ^{119m}Te atoms is shown in Fig. 1. It can be seen that the formation of the ^{119m}Sn Mössbauer level is preceded either by conversion isomeric transition (involving the parent ^{119mm}Sn nuclei) or by electron capture (involving the parent ^{119}Sb and ^{119m}Te nuclei). The probability that displaced daughter atoms will appear as a result of the radioactive decay of parent atoms depends on the relation between the recoil energy of the daughter nucleus E_R and the threshold energy of the atoms' displacement $E_d \approx 25$ eV.

We calculated the highest recoil energies for the daughter probe: the decay ^{119m}Te $\longrightarrow$ ^{119}Sb is accompanied by recoil energy $E_R \approx 24$ eV, and the decay ^{119}Sb $\longrightarrow$ ^{119m}Sn is accompanied by $E_R \approx 1.4$ eV. The larger value of recoil energy in the former case makes it possible to expect that the emission Mössbauer spectra of ^{119m}Te(^{119m}Sn) for the PbSb and PbSe samples include both the lines corresponding to the ^{119m}Sn atoms at the normal lattice sites and the lines corresponding to the ^{119m}Sn atoms displaced from these sites [4].

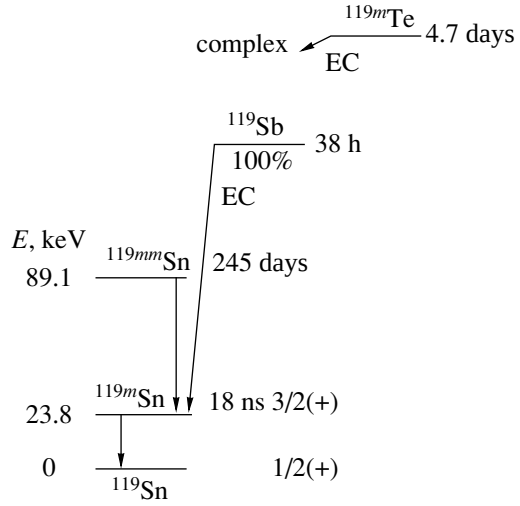

Fig. 1. Schemes of decay for ^{119mm}Sn, ^{119}Sb, and ^{119m}Te atoms.

It is assumed that the fine structure of Mössbauer spectra should depend not only on the rate of electron transfer between the $[Sn]^0$ and $[Sn]^{2+}$ centers but also on the version of Mössbauer spectroscopy used [2]. If the lifetimes of the $[Sn]^0$ (τ_n) and $[Sn]^{2+}$ (τ_i) states are much shorter than the lifetime of the ^{119m}Sn Mössbauer state ($\tau_0 \approx 20$ ns), only a single line will be observed in the absorption and emission Mössbauer spectra; this line features the isomer shift given by

$$\delta = \frac{\delta_i + R\delta_n}{R+1}. \quad (1)$$

If τ_n and $\tau_i \gg \tau_0$, an absorption Mössbauer spectrum should include two lines that correspond to $[Sn]^0$ and $[Sn]^{2+}$ and have a ratio of their intensities close to R, whereas the emission spectrum should include a single line that corresponds to $[Sn]^{2+}$ (here, R is the ratio of the areas under the $[Sn]^0$ and $[Sn]^{2+}$ spectra). This behavior is explained by the fact that both the conversion isomeric transition in the parent ^{119mm}Sn atoms and the electron capture in the parent ^{119}Sb and ^{119m}Te atoms initially give rise to multiply charged tin ions, which transform into the $[Sn]^{2+}$ state in a much shorter time than τ_0. The equilibrium between $[Sn]^{2+}$ and $[Sn]^0$ is then established slowly (in a much longer time than τ_0). By the instant of time τ_0, the equilibrium is not yet established, and, as a consequence, only a single $[Sn]^{2+}$ state is observed in the emission Mössbauer spectrum.

Thus, using the emission mode of Mössbauer spectroscopy based on the isotope ^{119m}Sn to study the states of tin impurity atoms in lead chalcogenides involves two problems: radioactive transmutation of the parent isotope can affect the site of the daughter atom in the lattice and can also affect the charge state of this atom. This study is devoted to solving these problems.

2. EXPERIMENTAL

Lead chalcogenides doped with ^{119mm}Sn were obtained by fusing starting semiconductor-grade components in evacuated quartz cells with subsequent annealing first of the ingots and then of pressed powders for 120 h at 650°C. The samples were of the single-phase type and had a structure similar to NaCl. Overstoichiometric lead was used as the donor impurity, while sodium was used as the acceptor impurity. The starting charge for the samples containing the daughter ^{119mm}Sn atoms was composed under the assumption that the tin impurity atoms replace lead atoms; as a result, the composition of the samples can be expressed as $Pb_{1-x-y}{}^{119m}Sn_xNa_yS$ and $Pb_{1-x-y}{}^{119m}Sn_xNa_ySe$.

The isotopes ^{119}Sb and ^{119m}Te were obtained according to the reactions ^{120}Sn(p, $2n$)^{119}Sb and ^{117}Sn(α, $2n$)^{119m}Te with subsequent separation of inactive ^{119}Sb and ^{119m}Te isotopes using anionic exchange. The Mössbauer sources were prepared by fusing the PbS and PbSe samples with the ^{119}Sb and ^{119m}Te inactive isotopes, so that the estimated concentrations of the antimony and tellurium atoms were no higher than 10^7 at/cm^3. The initial PbS and PbSe samples had n-type conductivity (with an excess of lead, $n \approx 5 \times 10^{18}$ cm^{-3}) or p-type conductivity (with an excess of sulfur or selenium, $p \approx 10^{18}$ cm^{-3}).

The emission Mössbauer spectra of ^{119m}Sn were measured in the temperature range 80–400 K using an SM 2201 commercial spectrometer. The compound $Ca^{119}SnO_3$ was used as the standard absorber with a surface density of 0.1 mg/cm^2 with respect to ^{119}Sn. The samples of lead chalcogenides doped with the parent ^{119mm}Sn, ^{119}Sb, and ^{119m}Te atoms served as the sources. Isomer shifts of the Mössbauer spectra of ^{119m}Sn will be given with respect to the $^{119m}SnO_2$ source.

3. RESULTS AND DISCUSSION

3.1. Paternal ^{119mm}Sn Atoms

3.1.1. PbS lead sulfide. Tin is an isoelectronic impurity in PbS and behaves like a donor [1, 2]. Therefore, only the neutral state of tin centers ($[Sn]^0$) can be observed in n-PbS (charges of [Sn] centers are given in relation to the charge of lead atoms). We chose the compound $Pb_{0.995}{}^{119mm}Sn_{0.005}S$ as the sample to be investigated; this sample contained overstoichiometric lead and featured n-type conductivity ($n = 3 \times 10^{18}$ cm^{-3} at 80 and 295 K). The Mössbauer spectra measured at 80 and 295 K were composed of individual lines (Figs. 2a, 2b) with the full width at the half-height Γ = 0.80(2) mm/s; the isomer shift of these lines δ = 3.70–3.65 mm/s corresponds to the divalent tin $^{119m}Sn^{2+}$ atoms. In what follows, the width of the ^{119m}Sn Mössbauer spectrum for the aforementioned source is assumed to be equal to the instrument-induced width of the ^{119}Sn line.

Only the ionized state of tin-containing centers can be observed in compensated p-type material. We stud-

ied a $Pb_{0.985}{}^{119mm}Sn_{0.005}Na_{0.01}S$ sample ($p = 6 \times 10^{13}$ cm^{-3} at 80 K and $p = 10^{17}$ cm^{-3} at 295 K). The Mössbauer spectra were represented by a single line (Figs. 2c, 2d) with an instrument-induced width and isomer shift (δ = 1.25–1.23 mm/s) that corresponded to tetravalent tin $^{119m}Sn^{4+}$.

A variation in the fine structure of Mössbauer spectra in the transition from $Pb_{1-x}{}^{119mm}Sn_xS$ solid solution to $Pb_{1-x-y}{}^{119mm}Sn_xNa_yS$ solid solution is attributed to the fact that both the parent ^{119mm}Sn impurity atoms and the daughter ^{119m}Sn impurity atoms that are formed as a result of the radioactive decay of the parent atoms replace lead atoms in the cubic PbS lattice and give rise to donor states. The ionization energy of the donors corresponds to levels in the lower half of the band gap. The line of bivalent tin $^{119m}Sn^{2+}$ corresponds to neutral $[Sn]^0$ atoms, whereas the line of tetravalent tin $^{119m}Sn^{4+}$ corresponds to doubly ionized states $[Sn]^{2+}$ of the tin donor center in PbS. By varying the ratio of the tin-impurity and acceptor concentrations in PbS, we can obtain any desired ratio between the intensities of the lines attributed to $^{119m}Sn^{2+}$ and $^{119m}Sn^{4+}$. In Figs. 2e and 2f, we show the spectra of a partially compensated $Pb_{0.99}{}^{119mm}Sn_{0.005}Na_{0.005}S$ sample ($p = 6 \times 10^{13}$ cm^{-3} at 80 K and $p = 6 \times 10^{16}$ cm^{-3} at 295 K); in the temperature range 80–295 K, these spectra include a superposition of the lines that correspond to the bivalent and tetravalent tin atoms and have an instrument-induced width of δ = 3.76–3.68 mm/s for $^{119m}Sn^{2+}$ and δ = 1.26–1.32 mm/s for $^{119m}Sn^{4+}$. As can be seen, the isomer shifts of the $^{119m}Sn^{2+}$ and $^{119m}Sn^{4+}$ spectra almost coincide with those of the $[Sn]^0$ and $[Sn]^{2+}$ spectra considered above; only a slight convergence of the corresponding lines is observed with increasing temperature. This convergence of the lines is caused by slow electron exchange between the $[Sn]^0$ and $[Sn]^{2+}$ states. It is noteworthy that the ratio of areas R under the $^{119m}Sn^{2+}$ and $^{119m}Sn^{4+}$ spectra for the sample under consideration decreases from R = 0.96(2) at 80 K to R = 0.90(2) at 295 K; this decrease is related to the stronger temperature dependence of the Mössbauer coefficient for bivalent tin.

3.1.2. Lead selenide PbSe. Only the neutral state of tin-related donor centers in PbSe was observed in an n-type $Pb_{0.995}{}^{119mm}Sn_{0.005}Se$ sample ($n = 2 \times 10^{19}$ cm^{-3} at 80 and 295 K). The Mössbauer spectra at 80 and 295 K consist of single lines with an instrument-induced width; the isomer shift of these lines (δ = 3.65–3.63 mm/s) corresponds to $^{119m}Sn^{2+}$ (Figs. 3a, 3b). This spectrum is related to neutral donor tin centers $[Sn]^0$. For a compensated p-type $Pb_{0.985}{}^{119mm}Sn_{0.005}Na_{0.01}Se$ sample ($p = 4 \times 10^{19}$ cm^{-3} at 80 and 295 K) with the concentration of sodium exceeding that of tin by a factor of 2, the Mössbauer spectrum at 80 K is formed by superimposed lines of $^{119m}Sn^{4+}$ (δ = 1.58(2) mm/s) and $^{119m}Sn^{2+}$ (δ = 3.63(2) mm/s); notably, R = 0.10(2).

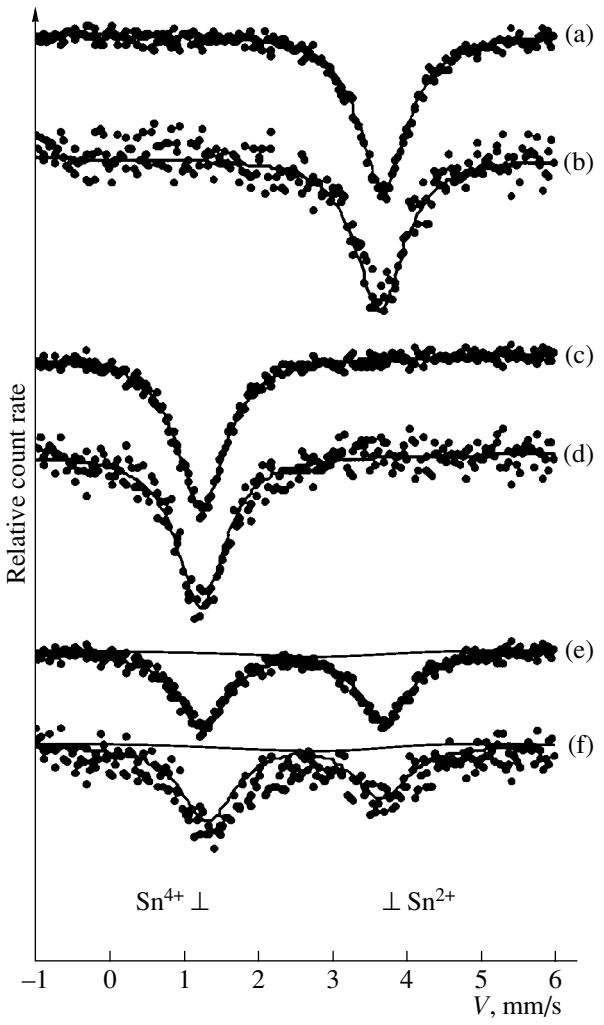

Fig. 2. Mössbauer spectra of (a, b) $Pb_{0.995}{}^{119mm}Sn_{0.005}S$, (c, d) $Pb_{0.985}{}^{119mm}Sn_{0.005}Na_{0.01}S$, and (e, f) $Pb_{0.99}{}^{119mm}Sn_{0.005}Na_{0.005}S$ at temperatures of (a, c, e) 80 K and (b, d, f) 295 K. Solid lines represent the resolution of experimental spectra into the components that correspond to $^{119m}Sn^0$, $^{119m}Sn^{2+}$, and $^{119m}Sn^{4+}$; the positions of the lines corresponding to the $^{119m}Sn^{2+}$ and $^{119m}Sn^{4+}$ ions are indicated.

Completely ionized tin centers $[Sn]^{2+}$ can be observed only in $Pb_{1-x-y}{}^{119mm}Sn_xNa_ySe$ samples in the situation where the sodium concentration far exceeds the doubled tin concentration. In particular, as can be seen from Figs. 3c and 3d, only a line corresponding to $^{119m}Sn^{4+}$ and having an instrument-induced width of δ = 1.52–1.50 mm/s is observed in the Mössbauer spectra of a $Pb_{0.98}{}^{119mm}Sn_{0.005}Na_{0.015}Se$ sample at 80 and 295 K.

Such behavior is attributed to the fact that tin energy levels are observed against the background of the valence band in PbSe. This circumstance gives rise to a situation where the chemical potential pinned at the partially filled tin level is also located within the

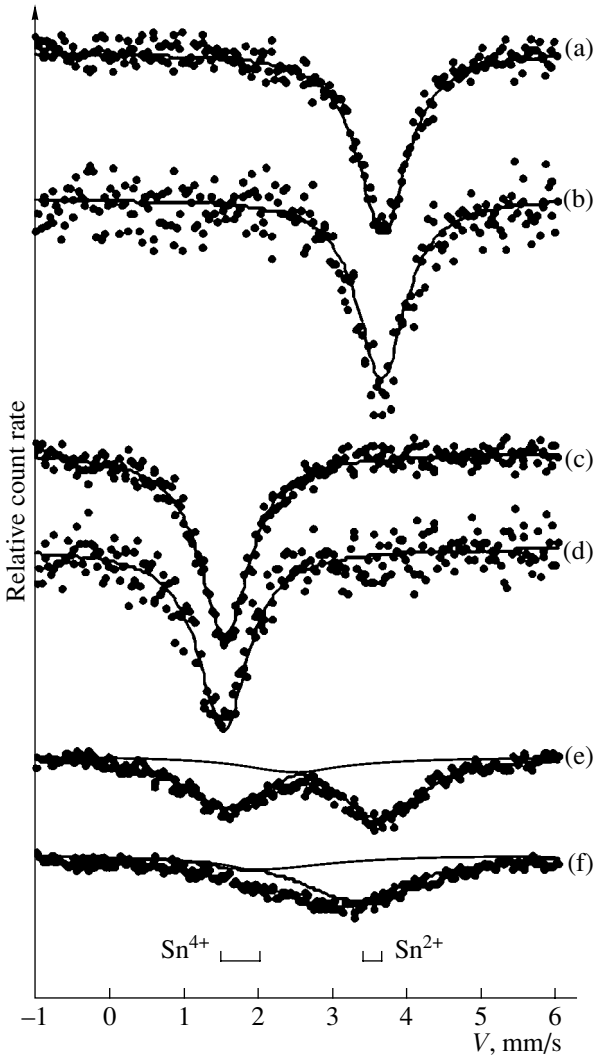

Fig. 3. Mössbauer spectra of (a, b) $Pb_{0.995}{}^{119mm}Sn_{0.005}Se$, (c, d) $Pb_{0.98}{}^{119mm}Sn_{0.005}Na_{0.015}Se$, and (e, f) $Pb_{0.99}{}^{119mm}Sn_{0.005}Na_{0.005}Se$ at temperatures of (a, c, e) 80 K and (b, d, f) 295 K. Solid lines represent the resolution of experimental spectra into the components that correspond to $^{119m}Sn^0$, $^{119m}Sn^{2+}$, and $^{119m}Sn^{4+}$; the positions of the lines corresponding to the $^{119m}Sn^{2+}$ and $^{119m}Sn^{4+}$ ions are indicated.

valence band, while the hole concentration is found to be comparable with the acceptor concentration.

As in the case of PbS, we can vary the ratio of the tin and sodium concentrations to obtain any controllable ratio between the intensities of the $^{119m}Sn^{2+}$ and $^{119m}Sn^{4+}$ lines in the Mössbauer spectrum. In Figs. 3e and 3f, we show the spectra for a partially compensated $Pb_{0.99}{}^{119mm}Sn_{0.005}Na_{0.005}Se$ sample ($p = 3.6 \times 10^{19}$ cm^{-3} at 80 K and $p = 2.8 \times 10^{19}$ cm^{-3} at 295 K). The spectrum measured at 80 K consists of two superimposed and partially broadened lines that are attributed to $^{119m}Sn^{2+}$ ($\delta = 3.60(2)$ mm/s, $\Gamma = 1.34(2)$ mm/s) and $^{119m}Sn^{4+}$ ($\delta = 1.56(2)$ mm/s, $\Gamma = 1.34(2)$ mm/s). The difference between the intensities of the lines under consideration is caused by a high hole concentration, as was already discussed above. As can be seen from Figs. 3e and 3f, as temperature increases, these lines in the Mössbauer spectrum of $Pb_{0.99}{}^{119mm}Sn_{0.005}Na_{0.005}Se$ converge significantly and are broadened even more (at 295 K, $\delta = 3.36(2)$ mm/s and $\Gamma = 1.79(2)$ mm/s for $^{119m}Sn^{2+}$ compared to $\delta = 2.0(2)$ mm/s and $\Gamma = 1.79(2)$ mm/s for $^{119m}Sn^{4+}$). All these facts are attributed to the processes of electron exchange between tin centers with differing valence.

It is important that the ratio R of areas under the $^{119m}Sn^{2+}$ and $^{119m}Sn^{4+}$ spectra for $Pb_{0.99}{}^{119mm}Sn_{0.005}Na_{0.005}Se$ increases from $R = 1.2(1)$ at 80 K to $R = 3.0(1)$ at 295 K. This behavior is inconsistent with the assumption that the Mössbauer coefficient for bivalent tin changes drastically with temperature and can be attributed to a variation in the energy spacing between the valence-band top and the tin impurity states.

3.2. Parent ^{119}Sb Atoms

Typical spectra of ^{119}Sb impurity atoms for the PbS and PbSe samples at 80 K are shown in Fig. 4. The spectrum of *n*-type samples is a superposition of two lines. The widths of both lines ($\Gamma = 1.33(2)$ mm/s) far exceed the instrument-induced width, which indicates that the cubic symmetry of the local surroundings of daughter ^{119m}Sn atoms formed as a result of the decay of ^{119}Sb atoms is distorted. This distortion may be caused by the difference in size between the substituted and substituting atoms. The line with higher intensity (the area under this line amounts to ~78% of the area under the entire spectrum for PbS and ~70% of that for PbSe) has an isomer shift of $\delta = 2.34(1)$ mm/s, which is characteristic of intermetallic tin compounds; thus, this line should be attributed to $^{119m}Sn^0$ centers in the anionic sublattice of PbS and PbSe. Lead atoms are the nearest neighbors of $^{119m}Sn^0$ centers; interaction between Pb atoms and these centers gives rise to isomer shift, which is typical of metallic tin compounds. Evidently, $^{119m}Sn^0$ atoms appear as a result of the decay of ^{119}Sb atoms located in the anionic sublattice of PbS and PbSe. The other lines in the spectra feature the isomer shifts $\delta = 3.73(1)$ mm/s for PbS and $\delta = 3.61(1)$ mm/s for PbSe; these shifts are characteristic of neutral $[Sn]^0$ tin centers in lead chalcogenides. As a result, the lines under consideration should be attributed to $^{119m}Sn^{2+}$ centers in cationic sublattices of PbS and PbSe. Evidently, $^{119m}Sn^{2+}$ atoms appear as a result of the decay of ^{119}Sb atoms located in cationic sublattices of PbS and PbSe.

The Mössbauer spectrum of *p*-type samples also consists of two superimposed and broadened lines ($\Gamma = 1.33(2)$ mm/s). One of the lines (the area under this line amounts to ~20% of the area under the entire spectrum for PbS and PbSe) features an isomer shift that is almost equal to that of the $^{119m}Sn^0$ spectrum. The line

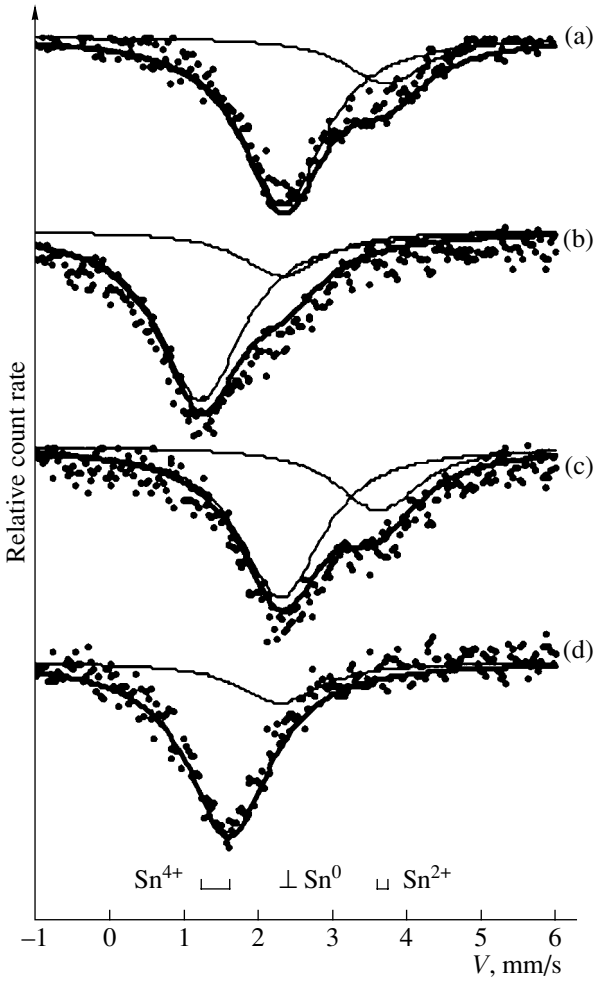

Fig. 4. Mössbauer spectra of ^{119}Sb(^{119m}Sn) impurity atoms at a temperature of 80 K for the (a, b) PbS and (c, d) PbSe samples of (a, c) *n*-type conductivity and (b, d) *p*-type conductivity. Solid lines represent the resolution of experimental spectra into the components that correspond to $^{119m}Sn^0$, $^{119m}Sn^{2+}$, and $^{119m}Sn^{4+}$; the positions of the lines corresponding to the $^{119m}Sn^{2+}$, $^{119m}Sn^{4+}$, and $^{119m}Sn^0$ centers are indicated.

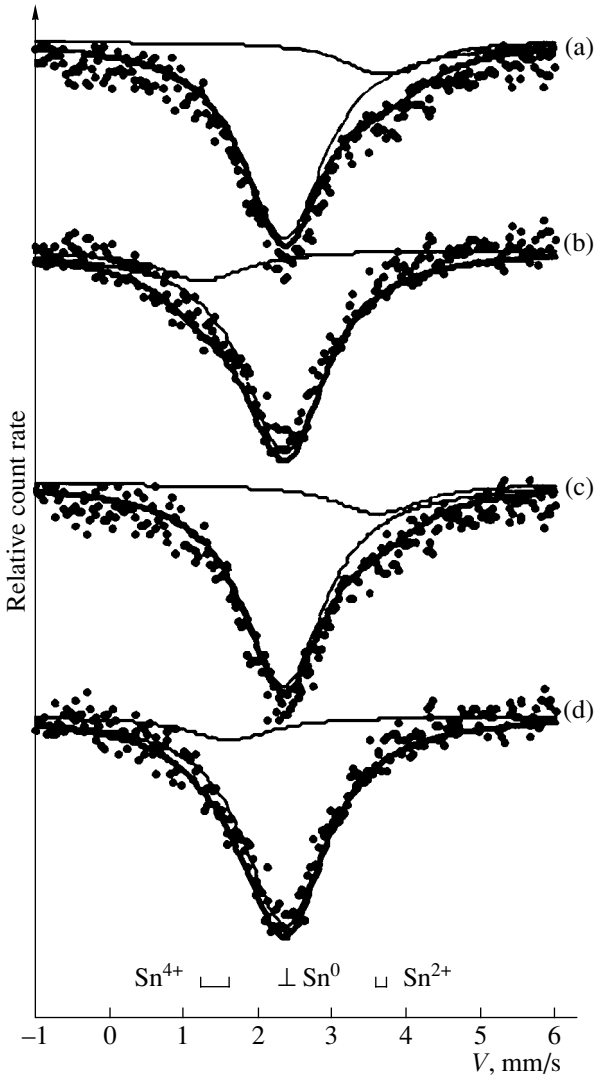

Fig. 5. Mössbauer spectra of ^{119m}Te(^{119m}Sn) impurity atoms at a temperature of 80 K for the (a, b) PbS and (c, d) PbSe samples of (a, c) *n*-type conductivity and (b, d) *p*-type conductivity. Solid lines represent the resolution of experimental spectra into the components that correspond to $^{119m}Sn^0$, $^{119m}Sn^{2+}$, and $^{119m}Sn^{4+}$; the positions of the lines corresponding to the $^{119m}Sn^{2+}$, $^{119m}Sn^{4+}$, and $^{119m}Sn^0$ centers are indicated.

under consideration is dominant in the *n*-type samples; however, its intensity is much lower in the *p*-type samples. This behavior is attributed to the fact that the localization site of antimony impurity atoms in the PbS and PbSe lattices depends on specific features of the deviation from stoichiometry in the aforementioned compounds. Antimony atoms are mainly localized in the anionic sublattice of the samples with an excess of lead, whereas these atoms are preferentially localized in the cationic sublattice of the samples with an excess of sulfur. The second line has an isomer shift that is characteristic of ionized $[Sn]^{2+}$ tin centers in lead chalcogenides; as a result, this line should be related to $^{119m}Sn^{4+}$ centers in the cationic sublattice of PbS and PbSe.

It is worth noting that the ^{119m}Sn center in the anionic sublattice of PbS and PbSe is an antisite defect; as follows from the fact that the isomer shift for the $^{119m}Sn^0$ spectrum is independent of the conductivity type of the material, the charge state of the antisite defect does not depend on the level of the Fermi position.

3.3. The Parent ^{119m}Te Atoms

Typical Mössbauer spectra of ^{119m}Te impurity atoms for the PbS and PbSe samples at 295 K are shown in Fig. 5. It can be seen that experimental spectra of *n*-type samples consist of two superimposed and broadened lines. The line with a higher intensity (the area under this line amounts to ~85% of the area under the entire

spectrum) with $\Gamma = 1.34(2)$ mm/s features the isomer shift $\delta = 2.34(2)$ mm/s that corresponds to $^{119m}Sn^0$ atoms surrounded by lead atoms. This spectrum should be attributed to the tin centers formed as a result of decay of the parent ^{119m}Te atoms that reside in the anionic sublattice. The line with a lower intensity ($\Gamma = 1.45(2)$ mm/s) features the isomer shift $\delta = 3.73(1)$ mm/s for PbS and $\delta = 3.61(1)$ mm/s for PbSe. These shifts correspond to neutral $[Sn]^0$ tin centers in the cationic sublattice of lead chalcogenides; i.e., the centers under consideration are the daughter $^{119m}Sn^{2+}$ atoms that appear as a result of decay of the parent ^{119m}Te atoms displaced from anionic to cationic lattice sites owing to the recoil energy.

The emission spectra of the *p*-type samples also consist of two superimposed lines. Along with the high-intensity $^{119m}Sn^0$ line corresponding to tin atoms in the anionic sublattice (the area under this line amounts to ~88% of the area under the entire spectrum; $\Gamma = 1.34(2)$ mm/s for this line), the spectrum also includes a line with a lower intensity. The isomer shift of the latter line ($\delta = 1.36(1)$ mm/s for PbS and $\delta = 1.60(1)$ mm/s for PbSe) corresponds to ionized $[Sn]^{2+}$ tin centers in the cationic sublattice of lead chalcogenides.

4. CONCLUSION

All the above-considered variations in the emission Mössbauer spectra of impurity ^{119m}Sn atoms in lead chalcogenides in relation to the chemical-potential position in the semiconductor band gap were also observed in the absorption Mössbauer spectra of tin impurity atoms in PbSe and PbS [1, 2]. Evidently, this observation does not confirm the assumption that the fine structures in the emission spectra of tin in PbSe and PbS differ from those in the corresponding absorption spectra in the situation where slow electron exchange is in effect. Apparently, the mechanism of appearance of multicharged tin ions as a result of conversion isomeric transition in parent ^{119mm}Sn atoms is valid only for free atoms. In contrast, the final charge state of a stabilized daughter atom corresponds to the charge state of the parent atom in condensed media with a high concentration of charge carriers.

As expected, a high recoil energy of ^{119}Sn atoms after radioactive decay of parent ^{119m}Te atoms gives rise to a significant fraction of displaced ^{119m}Sn atoms. However, ^{119m}Sn atoms remain mostly in the anionic sublattice and play the role of antisite defects after the radioactive decay $^{119m}\text{Te} \longrightarrow {}^{119}\text{Sb} \longrightarrow {}^{119m}\text{Sn}$. In contrast to tin atoms in the cationic sublattice, the antisite ^{119m}Sn defects are found to be electrically inactive centers.

ACKNOWLEDGMENTS

This study was supported by the Russian Foundation for Basic Research, project no. 02-02-17306.

REFERENCES

1. V. F. Masterov, F. S. Nasredinov, S. A. Nemov, and P. P. Seregin, Fiz. Tekh. Poluprovodn. (St. Petersburg) **30**, 840 (1996) [Semiconductors **30**, 450 (1996)].
2. V. F. Masterov, F. S. Nasredinov, S. A. Nemov, and P. P. Seregin, Fiz. Tekh. Poluprovodn. (St. Petersburg) **30**, 884 (1996) [Semiconductors **30**, 472 (1996)].
3. G. T. Alekseeva, E. A. Gurieva, P. P. Konstantinov, *et al.*, Fiz. Tekh. Poluprovodn. (St. Petersburg) **29**, 1388 (1995) [Semiconductors **29**, 719 (1995)].
4. V. F. Masterov, S. I. Bondarevskiĭ, F. S. Nasredinov, *et al.*, Fiz. Tekh. Poluprovodn. (St. Petersburg) **33**, 772 (1999) [Semiconductors **33**, 710 (1999)].

Translated by A. Spitsyn

Semiconductors, Vol. 37, No. 12, 2003, pp. 1373–1379. Translated from Fizika i Tekhnika Poluprovodnikov, Vol. 37, No. 12, 2003, pp. 1420–1426.

ELECTRONIC AND OPTICAL PROPERTIES OF SEMICONDUCTORS

Specific Features of Conductivity of $Cd_{1-x}Zn_xTe$ and $Cd_{1-x}Mn_xTe$ Single Crystals

L. A. Kosyachenko, A. V. Markov, E. L. Maslyanchuk, I. M. Rarenko, and V. M. Sklyarchuk

Chernovtsy State University, Chernovtsy, 58012 Ukraine

Submitted May 21, 2003; accepted for publication May 27, 2003

Abstract—The electrical characteristics of *p*-type $Cd_{1-x}Zn_xTe$ ($x = 0.05$) and $Cd_{1-x}Mn_xTe$ ($x = 0.04$) single crystals with a resistivity of 10^3–10^{10} Ω cm at 300 K are studied. The conductivity and its variation with temperature are interpreted on the basis of statistics of electrons and holes in a semiconductor with deep acceptor impurities (defects), with regard to their compensation by donors. The depth of acceptor levels and the degree of their compensation are determined. The problems of attaining near intrinsic conductivity close to intrinsic are discussed. © *2003 MAIK "Nauka/Interperiodica".*

1. INTRODUCTION

CdTe and $Cd_{1-x}Zn_xTe$ ($x = 0.05$–0.1) are currently the basic materials for semiconductor X-ray and gamma detectors operating without cryogenic cooling [1–3]. The conductivity of these materials and the lifetime of charge carriers, and, therefore, the key characteristics of detectors (the efficiency of collection of generated carriers and the energy resolution), are controlled by residual impurities and defects. A number of recent studies were devoted to analyzing the compensating effect of elements of Groups III or VII of the periodic table (Al, In, Cl, Br) and transition metals (V, Ti) on the conductivity of CdTe [4, 5]. However, the relationship of the conductivity and its temperature variation with the parameters of residual impurities and intrinsic defects for nominally undoped crystals have not been adequately studied, although, in this case, it is also possible to attain a level of conductivity close to intrinsic [1]. Up till now, it is not clearly understood under what conditions the compensation of acceptors by donors results in the semi-insulating state of a semiconductor with a high concentration of impurities and defects forming levels of different depth.

The purpose of this study is to gain insight into the mechanism of conductivity in nominally undoped $Cd_{1-x}Zn_xTe$ ($x = 0.05$) single crystals. As was found in the course of the study, the same mechanism of conductivity is typical of $Cd_{1-x}Mn_xTe$ ($x = 0.04$) solid solutions and undoped CdTe single crystals.

2. EXPERIMENTAL RESULTS

$Cd_{1-x}Zn_xTe$ ($x = 0.05$) and $Cd_{1-x}Mn_xTe$ ($x = 0.04$) single crystals were grown by the modified Bridgman method. The width of the band gap of $Cd_{0.95}Zn_{0.05}Te$, found from optical measurements, is equal to E_g = 1.505 eV (at 300 K), which is consistent with the approximately linear increase in E_g from 1.47 eV for CdTe to 2.26 eV for ZnTe [6]. The value of E_g determined by the same technique for $Cd_{0.96}Zn_{0.04}Te$ was found to be equal to 1.507 eV. The resistivity ρ of *p*-type wafers cut from the central parts of $Cd_{1-x}Zn_xTe$ and $Cd_{1-x}Mn_xTe$ ingots does not generally exceed 10^3–10^4 Ω cm at room temperature and may be even lower at the ends of the ingots (up to 10–100 Ω cm). In order to reduce the conductivity, we annealed wafers 1.5–2.5 mm thick in Cd vapor. As a result, the value of ρ increased noticeably (in some cases, up to 10^8–10^9 Ω cm or even higher). Hall measurements generally verified the *p*-type conductivity of crystals; the hole mobility did not exceed 60–80 $cm^2/(V\ s)$ at room temperature. Figure 1a shows the temperature dependences of the resistivity of $Cd_{1-x}Zn_xTe$ and $Cd_{1-x}Mn_xTe$ with different values of ρ at 300 K. The corresponding dependences for high-resistivity CdTe are also shown in Fig. 1a for comparison.

It is well known that in CdTe, as well as in $Cd_{1-x}Zn_xTe$ and $Cd_{1-x}Mn_xTe$ single crystals of high structural quality with small values of *x*, scattering by optical phonons is dominant at $T > 200$ K; hence, the mobility of carriers decreases with temperature proportionally to $T^{-3/2}$ [7, 8]. Since the effective densities of states in the conduction and valence bands, $N_c = 2(m_n^* kT/2\pi\hbar)^{3/2}$ and $N_v = 2(m_p^* kT/2\pi\hbar)^{3/2}$, are proportional to $T^{3/2}$, the temperature dependence of the resistivity $\rho = 1/(en\mu_n + ep\mu_p)$ is determined only by the exponential function (here, m_n^* and m_p^* are the electron and hole effective masses, respectively, and μ_n and μ_p are the electron and hole mobilities, respectively). Therefore, the dependences $\rho(T)$ in the coordinates $\log(\rho)$ and $1000/T$ are represented by straight lines whose slope directly yields the activation energy for the material conductivity ΔE (the corresponding values are indicated in Fig. 1a).

1063-7826/03/3712-1373$24.00

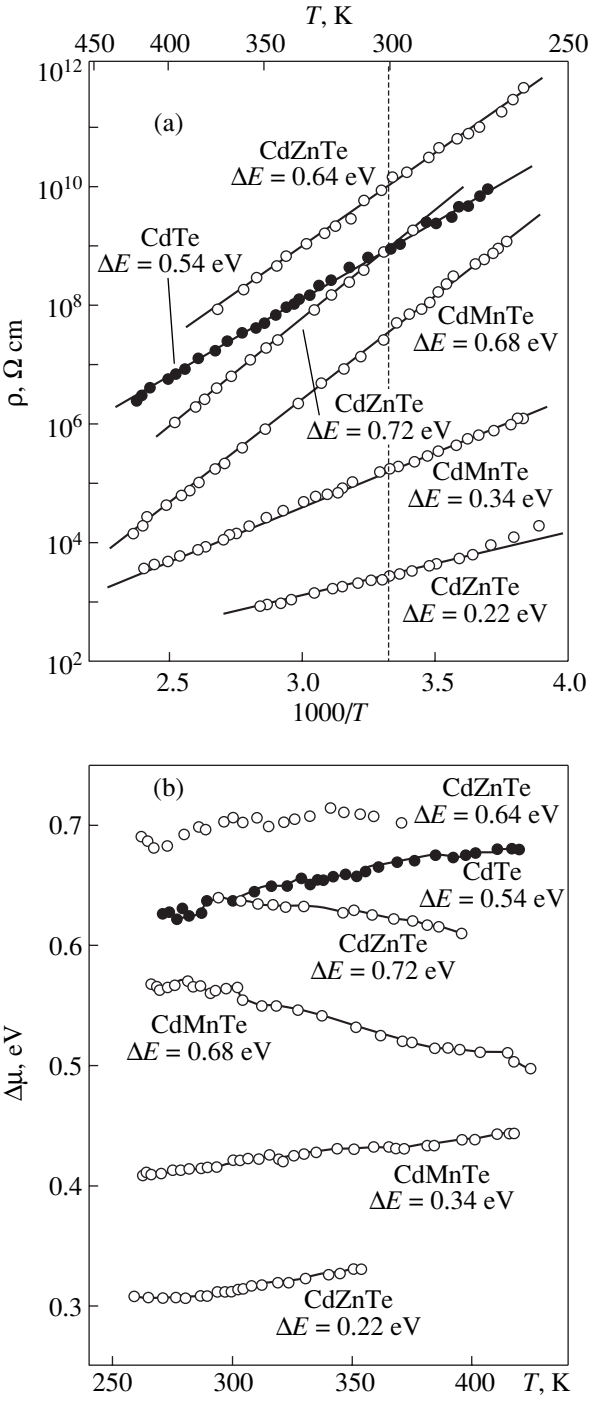

Fig. 1. (a) Temperature dependences of the resistivity ρ of $Cd_{0.95}Zn_{0.05}Te$ and $Cd_{0.96}Zn_{0.04}Te$ single crystals (with different values of ρ at 300 K) and CdTe. (b) Temperature dependences of the Fermi level position for the same samples.

Additional information on the type of conductivity can be derived from the position of the Fermi level and its shift in the band gap with variation in temperature. Let us denote the distance between the Fermi level and the top of the valence band (hereinafter, the Fermi level energy) as Δμ. Then, the densities of free electrons and holes can be written as

$$p = N_v \exp\left(-\frac{\Delta\mu}{kT}\right), \quad (1)$$

$$n = N_c \exp\left(-\frac{E_g - \Delta\mu}{kT}\right). \quad (2)$$

Solving the equation for ρ in Δμ and taking into account (1) and (2) (with the known resistivity and carrier mobility for each value of temperature), we can find the Fermi level energy as

$$\Delta\mu = kT\ln\left(\frac{1-\sqrt{1-4e^2\rho^2\mu_n\mu_p n_i^2}}{2e\rho\mu_n n_1^2/N_v}\right). \quad (3)$$

The curves Δμ(*T*), derived from the dependences ρ(*T*) by formula (3), are shown in Fig. 1a. The electron and hole effective masses, m_n^* and m_p^*, were assumed to be equal to $0.11m_0$ and $0.35m_0$, respectively (m_0 is the free-electron mass). For the electron and hole mobilities, we used the expressions $\mu_n = 5.5 \times 10^6 T^{-3/2}$ cm²/(V s) and $\mu_p = 4 \times 10^5 T^{-3/2}$ cm²/(V s) [8, 9], which are quite appropriate for CdTe at $T > 200$ K (when the scattering by optical phonons is dominant even at high impurity concentrations). These expressions yield 1058 and 77 cm²/(V s) at 300 K for the electron and hole mobilities, respectively.

3. DISCUSSION OF THE MODEL FOR CONDUCTIVITY IN THE CRYSTALS UNDER CONSIDERATION

Even the purest CdTe, $Cd_{1-x}Zn_xTe$, and $Cd_{1-x}Mn_xTe$ single crystals of highest structural quality contain impurities and defects, which introduce energy levels of different depth into the band gap [5, 9]. The residual impurities Ag, As, and P form shallow acceptor levels with energies E_v + (0.06–0.15) eV in initial CdTe, $Cd_{1-x}Zn_xTe$, and $Cd_{1-x}Mn_xTe$ crystals. An excess of Cd gives rise to a deep level at E_v + (0.4–0.45) eV in the band gap. The vacancy of Cd together with an impurity atom forms a so-called *A* center, which introduces a deeper level at E_v + 0.76 eV. The concentration of these impurities (defects), found by ESR in combination with optical and luminescence measurements, ranges from 10^{15} to 10^{16} cm^{-3} [5].

The high values of ρ observed in experiments (which are of the greatest practical importance) cannot be explained if we consider only acceptor levels, i.e., disregard compensation. In this case, the values of the activation energy Δ*E* found from the slope of the curves in Fig. 1a would yield half the ionization energy for impurity E_a ($\Delta E = E_a/2$). Then, for the samples with the highest resistivity (Δ*E* = 0.64–0.72 eV), we would have to assume the value of E_a to be equal to 1.28–1.44 eV. Donor levels were found in the band gaps of CdTe and

$Cd_{1-x}Zn_xTe$. These levels are 1.1 eV [9] or even 1.4 eV [5, 10] from the bottom of the condition band. Acceptor levels near the conduction band should also not be ruled out. However, the conductivity of a semiconductor with acceptor levels of different depth in the band gap is controlled by the shallowest levels. Simple calculation shows that, in the presence of acceptors, for example, with an ionization energy of 1.28 eV and a concentration of 10^{16} cm^{-3} (which independently ensure near intrinsic conductivity), the presence of acceptors with shallower levels (E_a = 0.1–0.7 eV) has almost no effect on the position of the Fermi level only when their concentration is lower than the intrinsic carrier concentration n_i (4×10^5 cm^{-3} for CdTe at 300 K). If the concentration of acceptors with shallower levels exceeds n_i, they determine the position of the Fermi level. Thus, we must assume that the role of acceptor levels located near the conduction band is not dominant in high-resistivity samples. The compensation of acceptors by donors, which is typical of compounds formed of elements of Groups II and VI of the periodic table, should be taken into account to explain the properties of the materials under study.

The fact that the activation energy may acquire two values, $\Delta E = E_a$ and $\Delta E = E_a/2$, is characteristic of the temperature dependence of the carrier concentration in a compensated semiconductor [11, 12]. For high degrees of compensation and low temperatures, the hole density in a *p*-type semiconductor is defined by the expression

$$p \approx \frac{N_a - N_d}{N_d} N_v \exp\left(-\frac{E_a}{kT}\right), \tag{4}$$

For low degrees of compensation and high temperatures, we have

$$p \approx \sqrt{N_a N_v} \exp\left(-\frac{E_a}{2kT}\right). \tag{5}$$

For Si, which features the impurity-ionization energy in the range 0.01–0.05 eV, the transition from (4) to (5) (the change in the slope from $\Delta E = E_a$ to $\Delta E = E_a/2$ in the dependence of $\ln pT^{-3/2}$ on $1000/T$) is observed at 10–20 K. In order to determine the conditions under which formulas (4) or (5) are valid for a wide-gap semiconductor with deep levels (especially, for the case in question where the conductivity is near intrinsic), one should solve the electroneutrality equation in the general form.

Let us consider a *p*-type semiconductor with three acceptor levels and one compensating donor level (Fig. 2). We denote the concentration of donors as N_d and the concentrations of acceptors as N_{a1}, N_{a2}, and N_{a3}. Their ionization energies are denoted as E_d, E_{a1}, E_{a2}, and E_{a3}, respectively. The ionization energy of acceptors, as well as the Fermi level energy $\Delta\mu$, are reckoned from the valence-band top, and the ionization energy of donors is reckoned from the conduction-band bottom.

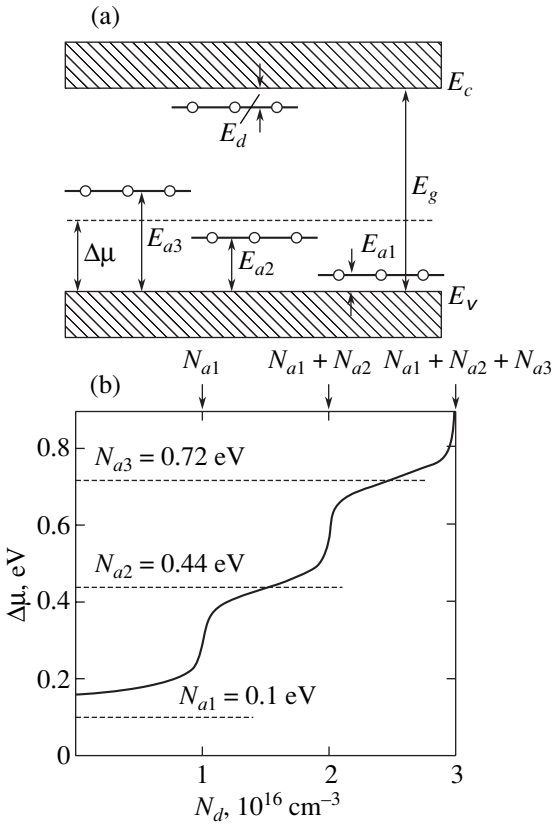

Fig. 2. (a) Energy-band structure of a semiconductor with one donor and three acceptor levels in the band gap. (b) Dependence of the Fermi level energy $\Delta\mu$ on the concentration of a compensating donor impurity N_d in the presence of three acceptor levels at E_{a1}, E_{a2}, and E_{a3}. The concentration of acceptors of each type is equal to 10^{16} cm^{-3}. The temperature is 300 K.

The electroneutrality condition for such an energy-level diagram has the form

$$n + N_{a1}^- + N_{a2}^- + N_{a3}^- = p + N_d^+, \tag{6}$$

where N_d^+, N_{a1}^-, N_{a2}^-, and N_{a3}^- are the concentrations of charged donors and acceptors. The electron and hole densities, *n* and *p*, respectively, are given by formulas (1) and (2). The concentrations of charged donors and acceptors can be written as

$$N_d^+ = \frac{N_d}{g_d \exp\left(-\dfrac{E_g - E_d - \Delta\mu}{kT}\right) + 1}, \tag{7}$$

$$N_a^+ = \frac{N_a}{g_a \exp\left(\dfrac{E_a - \Delta\mu}{kT}\right) + 1} \tag{8}$$

with subscripts 1, 2, and 3 for N_a, E_a, and N_a^-. For definiteness, we assume that the energies of the acceptor

and donor levels are equal to $E_{a1} = 0.1$, $E_{a2} = 0.44$, $E_{a3} = 0.72$, and $E_d = 0.1$ eV. Variation in the value of E_d in the range 0.1–0.7 eV does not affect the results of the calculation since, provided that a donor level is located several kT higher than an acceptor level, nearly all the donors are ionized. We also assume that the spin-degeneracy factors of impurities, g_d and g_a, are equal to 1. This assumption introduces a small error in the value of the ionization energy, which is equal to $kT\ln g_d$ or $kT\ln g_a$ (smaller than ±0.01 eV at 300 K).

Figure 2 shows the results of computer calculation of the dependence of the Fermi level energy $\Delta\mu$ on the concentration of donors, the concentrations of all three acceptors being equal to 10^{16} cm^{-3}. As can be seen from Fig. 2, the position of the Fermi level in a compensated semiconductor (and, consequently, its conductivity) is not controlled by the impurity or defect with the lowest ionization energy. At small values of N_d, which are insufficient for compensation of the shallowest acceptor, the Fermi level slowly shifts from the valence band with increasing N_d (certainly, $\Delta\mu \approx E_a/2$ at $N_d \longrightarrow 0$ and $T \longrightarrow 0$). When N_d approaches N_{a1}, the Fermi level shifts faster and, at $N_d = N_{a1}$, it passes to the energy range $\Delta\mu \approx E_{a2}$. With a further increase in N_d, the Fermi level slowly shifts from the valence band again until N_d approaches $N_{a1} + N_{a2}$. As soon as N_d becomes equal to $N_{a1} + N_{a2}$, the Fermi level again passes to the energy range $\Delta\mu \approx E_{a3}$. Finally, when N_d exceeds the total concentration of all acceptors $N_{a1} + N_{a2} + N_{a3}$, the Fermi level shifts to the upper half of the band gap (the conductivity becomes electronic and sharply increases).

It should be noted that the compensation of the deepest level occurs regardless of the presence of completely compensated shallower levels. The effect of these levels amounts to the fact that a certain number of donors is involved in the compensation of acceptors (in reality, N_d should be considered as the total concentration of all donors). The complete compensation of a partially compensated level has almost no effect on the deeper levels located above except for the very narrow transition region with $N_d = (1 \pm 0.05)N_a$, where an abrupt shift of the Fermi level occurs (especially for deep levels, which are of greatest interest). Satisfying such a severe condition, $N_d = (1 \pm 0.05)N_a$, within a large volume of a semiconductor seems unrealistic. More likely is a state in which the Fermi level slowly shifts with changing N_d, being near an acceptor level (so-called pinning). The relation $\Delta E = E_a$ corresponds to this state. Obviously, the relation $\Delta E = E_a/2$ can be observed only for weakly compensated, and, therefore, low-resistivity samples.

4. DISCUSSION

We will begin analysis with the experimental results obtained for $Cd_{1-x}Zn_xTe$ single crystals. In accordance with the above, the values of the activation energy ΔE = 0.64 and 0.72 eV, observed for high-resistivity samples, are equal to the ionization energies of acceptors E_a, and the rather high values of the resistivity $\rho = 1.6 \times 10^{10}$ and 9×10^8 Ω cm suggest a high degree of compensation of the high-resistivity material. Figures 3a and 3b show the temperature dependences of the Fermi level energy $\Delta\mu$ derived from the electroneutrality Eq. (6) for $E_a = 0.64$ and 0.72 eV at different values of $\xi = N_d/N_a$ for $Cd_{1-x}Zn_xTe$ (indicated in the figure). The curves $\Delta\mu(T)$ derived from the experimental dependences $\rho(T)$ by formula (3) (Fig. 1b) are also shown in Figs. 3a and 3b. As can be seen, we can determine the degree of compensation of acceptors by donors with a rather high accuracy by comparing the calculated and experimental dependences. For two samples with $\rho = 1.6 \times 10^{10}$ and 9×10^8 Ω cm, ξ = 0.90–0.92 and 0.044, respectively; i.e., higher ρ is obtained due to the higher degree of compensation, despite the fact that the acceptor level is shallower.

For a low-resistivity sample of $Cd_{1-x}Zn_xTe$ ($\rho = 3 \times 10^3$ Ω cm, $\Delta E = 0.22$ eV), a similar comparison of the experimental curve with the calculated dependences $\Delta\mu(T)$ yields inconsistent results. One would expect this since low ρ indicates weak compensation of the acceptor impurity, and, in this case, $\Delta E = E_a/2$; i.e., the ionization energy E_a is equal to 0.44 rather than 0.22 eV. Comparison of the experimental dependence $\Delta\mu(T)$ with the curves calculated for $E_a = 0.44$ eV at different degrees of compensation confirms such a suggestion (Fig. 3c). As can be seen from Fig. 3c, the best agreement between the results of calculation and experiment is obtained when we suggest a low, but noticeable, compensation $\xi \approx 0.001$. According to (5), $p = (N_aN_v)^{1/2}\exp(-E_a/2kT)$ with such a low compensation. Comparing the experimental hole densities, which can be easily determined if we know the resistivity and hole mobility ($p = 1/e\rho\mu_p$), with the above expression, we find the concentration of acceptor impurity (defect) $N_a = 6 \times 10^{15}$ cm^{-3}.

Comparison of the experimental dependences $\Delta\mu(T)$ for $Cd_{1-x}Mn_xTe$ with the calculated curves in Fig. 3d suggests a high compensation of acceptors by donors in the high-resistivity sample, which manifests itself in a large slope in the curve $\rho(T)$ and low compensation in the low-resistivity sample; i.e., the activation energy ΔE is equal to E_a in the former case and $E_a/2$ in the latter case. Figure 3d shows the theoretical dependences $\Delta\mu(T)$ calculated for $E_a = 0.68$ eV in a wide range of ξ and the experimental values of $\Delta\mu(T)$ for $Cd_{1-x}Mn_xTe$ (Fig. 1b). As can be seen, comparison of theory with experiment confirms the above suggestion. The conductivity of the $Cd_{1-x}Mn_xTe$ single crystals under investigation is controlled by the acceptor impurity with an ionization energy of 0.68 eV, which is differently compensated by donors in different samples. When the compensation is low ($\xi < 10^{-4}$), the activation energy ΔE is equal to 0.34 eV, and, when the compensation is relatively high ($\xi \approx 0.03$), $\Delta E = 0.68$ eV; i.e., the difference by a factor of 2 in the activation energies

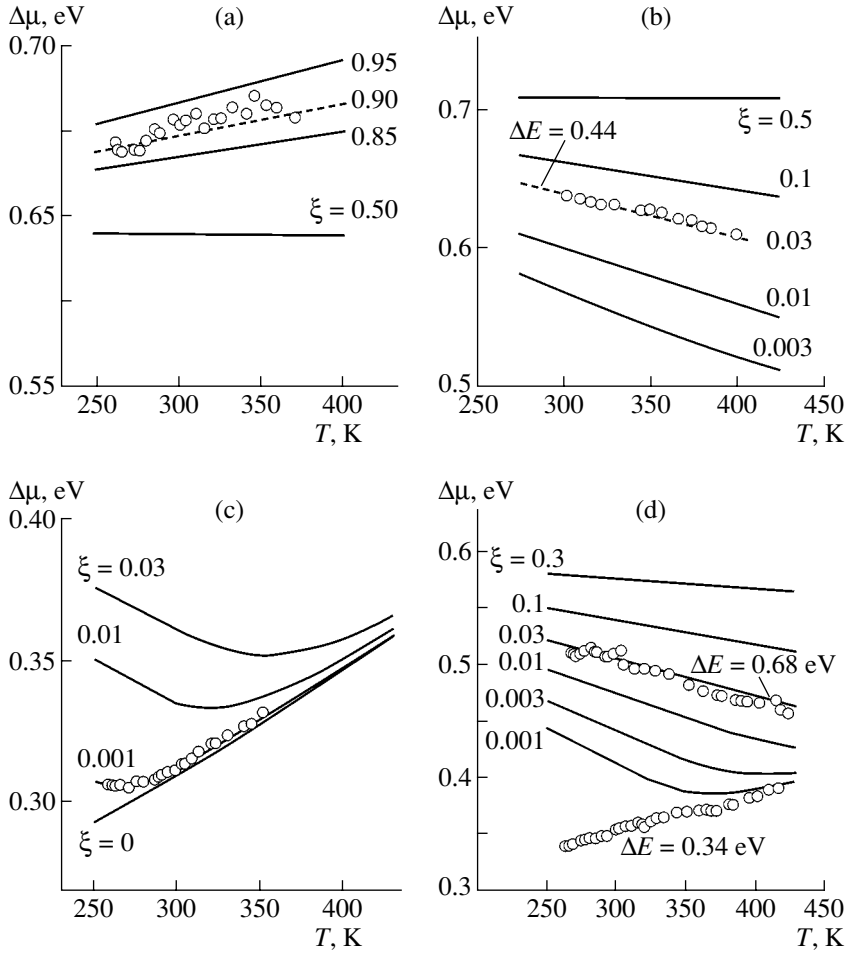

Fig. 3. Calculated temperature dependences of the Fermi level energy Δμ at different degrees of compensation $\xi = N_d/N_a$ (at $N_a = 10^{16}$ cm^{-3}) in (a–c) $Cd_{0.95}Zn_{0.05}Te$ and (d) $Cd_{0.96}Zn_{0.04}Te$. The ionization energy of acceptors E_a = (a) 0.64, (b) 0.72, (c) 0.44, and (d) 0.68 eV. Experimental data are indicated by circles.

for high- and low-resistivity samples (0.68 and 0.34 eV) is not accidental.

Analysis of the experimental data obtained for a CdTe single crystal shows that the high resistivity (1.5×10^9 Ω cm) of this sample is due to the near complete compensation ($\xi \approx 0.98$) of the acceptor level with $E_a = 0.54$ eV.

5. OPTIMAL CONDITIONS FOR OBTAINING SEMI-INSULATING MATERIALS

Thus, the conductivity of high-resistivity *p*-type $Cd_{1-x}Zn_xTe$, $Cd_{1-x}Mn_xTe$, and CdTe single crystals is governed by rather highly compensated deep acceptors, whereas the conductivity of relatively low-resistivity samples is determined by weakly compensated shallower acceptors.

The conductivity of a material can be significantly reduced by introducing a compensating impurity; however, this does not mean that 100% compensation ($\xi = 1$) makes the conductivity intrinsic. Such a requirement would be correct only in some specific cases, e.g., when acceptor and donor levels are located symmetrically with respect to the midgap and the electron and hole effective masses are equal. In reality, when deep-level acceptor impurities are compensated by shallow-level donors during the crystal growth or upon annealing the crystals in cadmium vapor, the situation is more complex.

Figure 4 shows the dependences of the resistivity ρ on the degree of compensation of acceptors by donors for three values of the ionization energy of acceptors: E_a = 0.44, 0.64, and 0.72 eV. The calculations were performed for $E_g = 1.5$ eV, $m_n^* = 0.11m_0$, $m_p^* = 0.35m_0$, $T = 300$ K, $N_a = 10^{16}$ cm^{-3}, and $E_d = 0.1$ eV (as was mentioned above, the value of E_d does not affect the results of calculations provided that the donor level is located (4–5)*kT* above the acceptor level).

As can be seen from Fig. 4, for the deepest acceptor level ($E_a = 0.72$ eV), the highest resistivity $\rho \approx 5 \times 10^{10}$ Ω cm is obtained at 60–70% compensation (ξ = 0.6–0.7); however, for $E_a = 0.64$ and 0.44 eV, the resis-

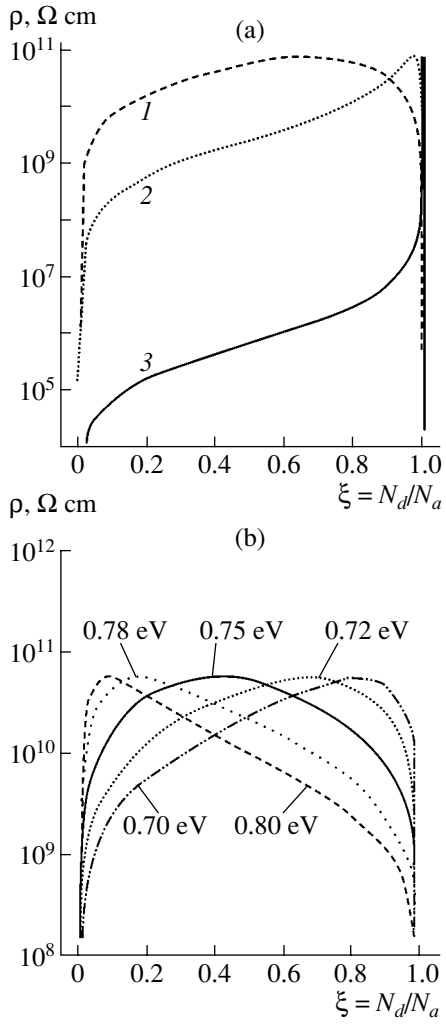

Fig. 4. Dependences of the resistivity ρ on the degree of compensation of acceptors by donors ξ at $T = 300$ K: (a) the ionization energy of acceptors E_a = (*1*) 0.72, (*2*) 0.64, and (*3*) 0.44 eV; (b) the case of levels located near the midgap.

tivity is highest at 96 and nearly 100% compensation, respectively. We should note that, due to the large difference between the electron and hole mobilities, the maximum resistivity (5×10^{10} Ω cm) is higher than in the intrinsic semiconductor (2×10^{10} Ω cm). It important that, in the case of $E_a = 0.72$ eV when the degree of compensation ξ is varied over a rather wide range (0.2–0.8), the resistivity decreases in comparison with the largest value by no more than a factor of 2. In order to ensure the same change in resistivity for E_a = 0.64 eV, one should vary the degree of compensation in a narrower range, specifically, from 0.85 to 0.99. Notably, ξ should not exceed 0.99 because ρ abruptly decreases in this case. For $E_a = 0.44$ eV, almost complete compensation ξ = 1 should be provided with a very high accuracy (which seems to be unrealistic for the technology currently in use).

Thus, a high resistivity of a compensated semiconductor is attained most easily when its conductivity is governed by impurities (defects), whose levels are located near the midgap (for example, at a distance of no more than 0.1 eV). Deep levels can be created by introducing special impurities during the growth of the crystal. In [4], a model developed for GaAs [13] was used. According to this model, the conductivity of CdTe doped with V or Ti, which is close to that of a semi-insulating material (semi-insulating conductivity), is attributed to the compensation of acceptors, which are always present in this material, by donors whose levels are located near the midgap. In this case, the material is overcompensated in such a way that the total concentration of donors slightly exceeds that of acceptors. As a result, a semi-insulating material with weakly pronounced *n*-type conductivity is formed. Later, the same model was used to explain the semi-insulating conductivity of nominally undoped CdTe [14]. It was suggested that tellurium ions occupying cadmium sites in the lattice (Te_{Cd} antisite defects) play the role of deep donors. Thus, in order to make the conductivity of the single crystals under investigation (which, generally, have *p*-type conductivity) close to semi-insulating, one can either undercompensate deep-level acceptors or overcompensate deep-level donors, which gives rise to a very low *p*- or *n*-type conductivity, respectively. We should note that additional doping with a deep-level donor impurity may lead to an undesirable decrease in the carrier lifetime.

6. CONCLUSIONS

The conductivity of nominally undoped high-resistivity *p*-type $Cd_{1-x}Zn_xTe$ and $Cd_{1-x}Mn_xTe$ single crystals, as well as that of CdTe, is controlled by acceptor impurities with ionization energies E_a = 0.54, 0.64, 0.68, or 0.72 eV. The difference observed in the conductivities of different samples is due to the different degrees of compensation of acceptors by donors in these samples. In semi-insulating single crystals, the degree of compensation ξ ranges from 0.02 to 0.98; in low-resistivity crystals, $\xi < 10^{-3}$–10^{-4}. The concentration of acceptors in the single crystals under study is in the range $(6–9) \times 10^{15}$ cm^{-3}. Near intrinsic conductivity can be obtained most easily by compensating acceptors whose levels are located near the midgap ($E_a = E_g/(2 \pm 0.1)$ eV). In this case, a quite significant change in the degree of compensation (ξ = 0.3–0.9) only slightly changes the conductivity (severalfold). If the impurity (defect) level is found at a large distance from the midgap (more than a few tenths of an electron volt away), near complete compensation is required to obtain intrinsic conductivity; in this case, the condition of near complete compensation should be satisfied throughout the crystal bulk with a high accuracy.

ACKNOWLEDGMENTS

We are grateful to Z.I. Zakharuk for the single crystals and to C.L. Korolyuk for helpful discussion of the results.

REFERENCES

1. Y. Eisen and A. Shor, J. Cryst. Growth **184–185**, 1302 (1998).
2. Y. Eisen, I. Mardor, and A. Shor, Nucl. Instrum. Methods Phys. Res. A **428**, 158 (1999).
3. M. R. Squillante, L. Cirignano, and R. Grazioso, Nucl. Instrum. Methods Phys. Res. A **458**, 288 (2001).
4. M. Fiederle, D. Ebling, C. Eiche, *et al.*, J. Cryst. Growth **146**, 142 (1995).
5. D. M. Hofmann, W. Stadler, P. Chrismann, and B. K. Meyer, Nucl. Instrum. Methods Phys. Res. A **380**, 117 (1996).
6. L. A. Kosyachenko, I. M. Rarenko, Z. I. Zakharuk, *et al.*, Fiz. Tekh. Poluprovodn. (St. Petersburg) **37**, 238 (2003) [Semiconductors **37**, 227 (2003)].
7. S. S. Devlin, in *Physics and Chemistry of II–VI Compounds*, Ed. by M. Aven and J. S. Prener (North-Holland, New York, 1967; Mir, Moscow, 1970), p. 418.
8. I. Turkevych, R. Grill, J. Franc, *et al.*, Semicond. Sci. Technol. **17**, 1064 (2002).
9. A. Castaldini, A. Cavallini, and B. Fraboni, J. Appl. Phys. **83**, 2121 (1998).
10. B. K. Meyer, P. Omling, E. Weigel, and G. Muller-Vogt, Phys. Rev. B **46**, 15135 (1992).
11. K. Seeger, *Semiconductor Physics* (Springer, Berlin, 1974; Mir, Moscow, 1977).
12. J. S. Blakemore, *Semiconductor Statistics* (Pergamon Press, Oxford, 1962; Mir, Moscow, 1964).
13. E. J. Jonson, J. A. Kafalas, and R. W. Davies, J. Appl. Phys. **54**, 204 (1983).
14. M. Fiederle, C. Eiche, M. Salk, *et al.*, J. Appl. Phys. **84**, 6689 (1998).

Translated by Yu. Sin'kov

Semiconductors, Vol. 37, No. 12, 2003, pp. 1380–1382. Translated from Fizika i Tekhnika Poluprovodnikov, Vol. 37, No. 12, 2003, pp. 1427–1430.

ELECTRONIC AND OPTICAL PROPERTIES OF SEMICONDUCTORS

Photoluminescence at 1.5 μm from Single-Crystal Silicon Layers Subjected to Mechanical Treatment

R. I. Batalov*, R. M. Bayazitov*, B. A. Andreev, D. I. Kryzhkov**, E. I. Terukov***, and V. Kh. Kudoyarova*****

**Zavoiskiĭ Physicotechnical Institute, Kazan Scientific Center, Russian Academy of Sciences, Sibirskiĭ trakt 10/7, Kazan 29, 420029 Tatarstan, Russia*

e-mail: bayaz@kfti.knc.ru

***Institute for Physics of Microstructures, Russian Academy of Sciences, Nizhni Novgorod, 603950 Russia*

****Ioffe Physicotechnical Institute, Russian Academy of Sciences, Politekhnicheskaya ul. 26, St. Petersburg, 194021 Russia*

Submitted June 17, 2003; accepted for publication June 18, 2003

Abstract—The photoluminescence of single-crystal silicon layers (100) subjected to mechanical processing (grinding and polishing) is investigated. An intense photoluminescence signal at 77 K with a peak at 0.83 eV (1.5 μm) and FWHM = 50 meV was observed after annealing at 800°C. The possible origin of this signal is discussed and is tentatively related to dislocations decorated by impurity atoms. © *2003 MAIK "Nauka/Interperiodica".*

1. INTRODUCTION

Single-crystal silicon is an inefficient light emitter at room temperature due to its indirect band gap (the band gap E_g = 1.1 eV), which prevents the development of optoelectronic devices on the basis of it (light-emitting diodes and lasers) and their integration with conventional microelectronic devices. In the last 10–15 years, active efforts have been made to develop new Si-based light-emitting structures. This line of research is commonly referred to as silicon optoelectronics. The development of efficient Si-based emitters operating at a wavelength of 1.5 μm, which corresponds to the Si and SiO_2 transparency region and is used in fiber communication lines, is of particular interest. The basic approaches to the development of such emitters are Si doping with erbium ions (Si:Er) [1, 2], the synthesis of direct-gap iron disilicide (β-$FeSi_2$) [3, 4], and the formation of Si dislocation structures causing a number of emission lines D1–D4, where line D1 (~0.81 eV) is of particular interest for optoelectronics [5, 6].

The basic ways of introducing extended-defect structures into Si that emit at 1.5 μm (D1 line) are plastic deformation of the Si crystal [5, 6], SiGe layer growth on a Si substrate [7, 8], heavy-ion implantation into Si followed by annealing [9, 10], and Si surface melting by a laser beam [11]. As was shown in [7, 12, 13], a necessary condition for the initiation of intense photoluminescence (PL) at 1.5 μm is the decoration of dislocations and stacking faults by transition- and noble-metal atoms (Cu, Fe, Ni, Ag, Au, and Pt). There exists an optimum level of defect decoration, ~10^{13} cm^{-2}, at which the PL signal is strongest. As the degree of decoration is increased to 10^{15} cm^{-2}, metal silicide precipitates (Cu_3Si, $NiSi_2$) are formed and completely suppress photon emission at 1.5 μm.

The effect of metal atom accumulation at Si lattice defects during high-temperature annealing is widely used in microelectronic technology to remove undesirable metal impurities from active device regions at the top surface of a Si single crystal to inactive regions of the crystal [14]. To this end, the rear surface of a Si wafer is subjected to mechanical processing (grinding and polishing), which gives rise to a damaged layer; the latter is up to 10 μm thick and contains a significant number of structural defects, mostly dislocations [15–17]. Currently, there are no systematic data on PL studies of a damaged Si layer decorated by metal atoms during gettering, despite the fact that this object in principle can yield intense PL with moderate levels of decoration of dislocations by impurity atoms (10^{12}–10^{14} cm^{-2}), which can be achieved by annealing.

In this paper, we report the results of studying the PL of silicon wafers whose rear surface was subjected to conventional mechanical processing (grinding and polishing). As a result of subsequent annealing, an intense PL signal was observed with a peak at 0.83 eV (1.5 μm); this peak differed in spectral position and shape from the well-known D1 line caused by dislocations.

2. EXPERIMENTAL

We used conventional single-crystal silicon wafers (ELMA, 75 mm in diameter) grown by the Czochralski method, with an oxygen content of 5×10^{17} cm^{-3}. The *n*-Si (100) (phosphorus-doped to ~10^{15} cm^{-3}) wafers 380 μm thick had a resistivity of 4–5 Ω cm. The rear

(inactive) surface of the wafers was mechanically ground and polished, while the top (active) surface was additionally polished chemically to mirror luster to remove the damaged layer. Samples of area S = 1.0–1.5 cm^2 were annealed in a quartz tube in nitrogen at a temperature of 800°C for 20 min. Silicon samples were loaded into a furnace at room temperature. The sample heating and cooling rates were 30 and 50 K/min, respectively. The PL spectra of initial and annealed Si samples were measured at 77 K in the near infrared (IR) region (1.0–1.7 μm). The PL signal was excited by a 300-mW argon laser (514.5 nm) and was measured using a Bomem Fourier spectrometer with a cooled germanium *p–i–n* photodiode, from the side exposed to the laser beam.

3. RESULTS AND DISCUSSION

The PL spectra measured from the rear (mechanically ground and polished) side of the initial Si wafer before annealing contained no spectral features in the range 0.75–1.2 eV (Fig. 1, curve *1*). The absence of a peak at 1.1 eV (Si intrinsic emission) is explained by the strong distortion and stresses of Si layers, which suppress radiative recombination of nonequilibrium electron–hole pairs. After annealing (800°C, 20 min), the PL spectrum measured from the wafer rear side changed drastically (curve *2*). In this case, an intense and symmetric PL line with a peak at 0.83 eV (1.5 μm) and FWHM = 50 meV was observed, as well as a signal of intrinsic Si emission at 1.1 eV with an intensity that was almost sevenfold lower. The appearance of Si edge luminescence is indicative of the crystallization of amorphous Si surface layers up to 100 nm thick [17], relaxation of stresses, and elimination of various point defects that are introduced by mechanical processing and are efficient centers of nonradiative recombination.

To clarify the origin of the intense PL signal at 0.83 eV, a layer ~3 μm thick was etched from the Si wafer rear side with a solution of hydrofluoric and nitric acids (HF : HNO_3 = 1 : 4), and PL was measured at a temperature of 77 K (curve *3*). A sharp falloff in signal intensity was observed at 0.83 eV with no significant change in its spectral position, while the intensity of intrinsic Si emission increased, which suggests that the layer most damaged by mechanical polishing was removed.

In contrast to the spectra measured from the rear side, the PL spectra measured from the front (chemically polished) side of the initial wafer (Fig. 2, curve *1*) feature rather intense edge luminescence at 1.1 eV. After annealing (curve *2*), the edge luminescence intensity increases, and an additional line appears with a peak at 0.83 eV; however, the intensity of this peak is almost five times lower than that of the signal measured from the rear side. The significantly lower intensity of the PL signal at 0.83 eV from the wafer front surface is probably caused by the much lower density of processing-induced defects that remained after additional chemical polishing of this surface.

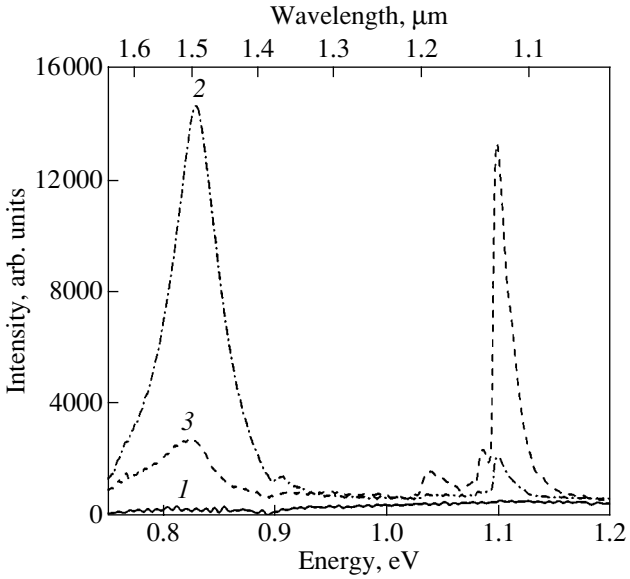

Fig. 1. Photoluminescence spectra measured at 77 K from the rear side of the *n*-Si (100) wafer (*1*) in the initial state, (*2*) after annealing at 800°C for 20 min, and (*3*) after annealing at 800°C for 20 min with etchings of a layer 3 μm thick.

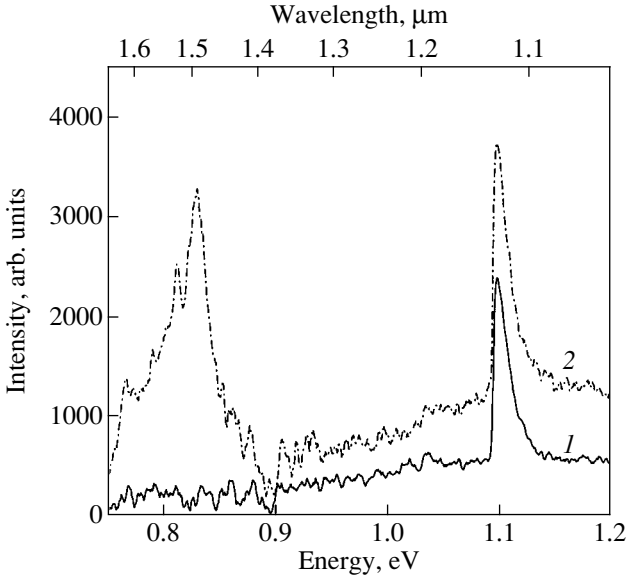

Fig. 2. Photoluminescence spectra at 77 K, measured from the top surface of the *n*-Si (100) wafer (*1*) in the initial state and (*2*) after annealing at 800°C for 20 min.

The spectral position (0.83 eV) of the intense PL band detected in this study significantly differs from the position of the well-known line *D*1 (0.807–0.810 eV) related to Si dislocations [5]. The etching experiments we carried out show that the optically active Si layer is located in the rear side of the wafer at a depth of 5 μm from the surface and is caused by defects introduced by

mechanical processing, which were transformed during high-temperature annealing. Let us clarify the possible origin of the intense PL signal from the rear surface of the wafer.

As is well known, the Si layer damaged by mechanical processing at the rear surface of the wafer is a sink for transition- and noble-metal atoms (Cu, Ni, Fe, Au, and Pt), which diffuse rapidly in Si. Moreover, it is known that the damaged layer can also getter interstitial oxygen in Si, which is accumulated at lattice defects and forms oxide precipitates SiO_x after long-term annealing [16]. It is also known that the PL band in the range 0.83–0.84 eV was observed previously both at (oxidation- and epitaxy-induced) stacking faults decorated by gold atoms [13] and in Si containing oxygen precipitates [18]. It should be noted that the nucleation and growth of oxygen precipitates takes place during multistage (450–1050°C) and long-term (up to 120 h) annealing, which was not carried out in the experiments we conducted. The most probable cause of the intense PL signal at 0.83 eV might be the gettering of metal impurities, originally contained in the Si single-crystal bulk with concentrations $<10^{14}$ cm^{-3}, by the defects of mechanical processing. The influence of residual impurities in the Si crystal on PL at 1.5 μm is currently being studied using deep-level transient spectroscopy (DLTS) and neutron activation analysis (NAA).

4. CONCLUSION

Single-crystal silicon Si(100) wafers subjected to conventional mechanical processing (grinding and polishing) were studied using photoluminescence spectroscopy at 77 K in the near IR range (1.0–1.7 μm). After annealing, (800°C, 20 min) an intense PL signal was detected as a symmetric line with a peak at 0.83 eV (1.5 μm) and FWHM = 50 meV. Chemical removal of a mechanically treated and thermally annealed Si layer 3 μm thick resulted in almost total loss of the PL signal. It is assumed that the intense PL signal is caused by decoration of polishing-induced defects by impurity atoms from the bulk of the Si single crystal.

ACKNOWLEDGMENTS

This study was supported by the Russian Foundation for Basic Research (project no. 02-02-16838) and the federal program "Low-Dimensional Quantum Structures" (4V19).

REFERENCES

1. H. Ennen, K. Schneider, G. Pomrenke, and A. Axmann, Appl. Phys. Lett. **43**, 943 (1983).
2. H. Ennen, G. Pomrenke, A. Axmann, *et al.*, Appl. Phys. Lett. **46**, 381 (1985).
3. M. C. Bost and J. E. Mahan, J. Appl. Phys. **58**, 2696 (1985).
4. D. Leong, M. Harry, K. J. Reeson, and K. P. Homewood, Nature **387**, 686 (1997).
5. N. A. Drozdov and A. A. Patrin, Pis'ma Zh. Éksp. Teor. Fiz. **23**, 651 (1976) [JETP Lett. **23**, 597 (1976)].
6. V. V. Kveder, E. A. Steinman, S. A. Shevchenko, and H. G. Grimmeiss, Phys. Rev. B **51**, 10520 (1995).
7. V. Higgs, Solid State Phenom. **32–33**, 291 (1993).
8. E. A. Steinman, V. I. Vdovin, T. G. Yugova, *et al.*, Semicond. Sci. Technol. **14**, 582 (1999).
9. M. G. Grimaldi, S. Coffa, C. Spinella, *et al.*, J. Lumin. **80**, 467 (1999).
10. N. A. Sobolev, O. B. Gusev, E. I. Shek, *et al.*, J. Lumin. **80**, 357 (1999).
11. E. O. Sveinbjornsson and J. Weber, Appl. Phys. Lett. **69**, 2686 (1996).
12. V. Higgs, E. C. Lightowlers, G. Davies, *et al.*, Semicond. Sci. Technol. **4**, 593 (1989).
13. V. Higgs, M. Goulding, A. Brinklow, and P. Kightley, Appl. Phys. Lett. **60**, 1369 (1992).
14. A. A. Istratov, H. Hieslmair, and E. R. Weber, Appl. Phys. A **70**, 489 (2000).
15. Ya. A. Ugaĭ, I. V. Kirichenko, and K. R. Kurbanov, Izv. Akad. Nauk SSSR **8** (2), 209 (1972).
16. T. J. Magee, C. Leung, H. Kawayoshi, *et al.*, Appl. Phys. Lett. **38**, 891 (1981).
17. J. Chen and I. DeWolf, Semicond. Sci. Technol. **18**, 261 (2003).
18. S. Binetti, S. Pizzini, E. Leoni, *et al.*, J. Appl. Phys. **92**, 2437 (2002).

Translated by A. Kazantsev

Semiconductors, Vol. 37, No. 12, 2003, pp. 1383–1386. Translated from Fizika i Tekhnika Poluprovodnikov, Vol. 37, No. 12, 2003, pp. 1431–1434.

SEMICONDUCTOR STRUCTURES, INTERFACES, AND SURFACES

Investigation of the ZnS–CdHgTe Interface

P. V. Biryulin, S. A. Dudko, S. A. Konovalov, Yu. A. Pelevin, and V. I. Turinov

NPO Istok, Fryazino, 141120 Russia

e-mail: birulin@sl.ru

Submitted February 28, 2003; accepted for publication March 18, 2003

Abstract—The ZnS–$Cd_xHg_{1-x}Te$ interface was investigated using the capacitance–voltage characteristics of MIS structures in experimental samples. During fabrication of the n^+–p junctions based on p-$Cd_xHg_{1-x}Te$, the density of states within the range $N_{ss} = (1–6) \times 10^{11}$ cm^{-2} eV^{-1} at $T = 78$ K was obtained. The experiments showed that the conditions in which n^+–p junctions are fabricated only slightly affect the state of the ZnS–CdHgTe interface. The negative voltages of the flat bands V_{FB}, even if immediately after deposition of the ZnS films $V_{FB} > 0$, point to the enrichment of the ZnS–p-CdHgTe near-surface layer with majority carriers, specifically, holes. This led to a decrease in the leakage current over the surface. During long-term storage (as long as ~15 years) in air at room temperature, no degradation of differential resistance R_d, current sensitivity S_i, and detectivity D^* of such n^+–p junctions with a ZnS protection film was observed. © *2003 MAIK "Nauka/Interperiodica".*

The passivation coating of photodiode structures based on narrow-gap $Cd_xHg_{1-x}Te$ with $x = 0.2$ for the spectral range 8–14 μm involves some critical factors. In addition to the usual requirements for semiconductor devices such as stability of the interface, good adhesion, and high dielectric strength, the coating should also sustain the thermal cycles from 78 to 300 K without changing the electrical properties. In addition, perhaps the main requirement for the temperature of dielectric deposition is that it be no higher than 90–100°C because of the thermal instability of $Cd_xHg_{1-x}Te$.

For SiO_2–$Cd_xHg_{1-x}Te$ structures ($x \approx 0.2$), the density of surface states N_{ss} can be both low ($N_{ss} = (1–2) \times 10^{11}$ cm^{-2} eV^{-1}) and high ($N_{ss} = (8–9) \times 10^{11}$ cm^{-2} eV^{-1}) [1]. According to [2], N_{ss} varies from 1.25×10^9 to 3×10^{11} cm^{-2} eV^{-1}. For structures with native anodic films, N_{ss} varies from 1×10^9 to 6×10^{11} cm^{-2} eV^{-1} [3]. For structures with anodic oxide, for example (see [4]), for HgCdTe with $x = 0.22$ and $p_0 = 1.6 \times 10^{16}$ cm^{-3} and an additional ZnS film with a thickness of $d_{ZnS} = 0.25$ μm, $N_{ss} = 4 \times 10^{11}$ cm^{-2} eV^{-1} was found. With the passivation by a SiN_x film, for n^+–p junctions based on $Cd_xHg_{1-x}Te$ with a threshold wavelength of sensitivity $\lambda = 5.4$ μm for SiN_x–$Hg_{1-x}Cd_xTe$ structures ($x = 0.3$), the lowest value of N_{ss} (10^{11} cm^{-2} eV^{-1}) was found, whereas for ZnS–$Hg_{1-x}Cd_xTe$ with the same x, $N_{ss} = 5 \times 10^{11}$ cm^{-2} eV^{-1} [5]. Nemirovsky and Bahir [6] compared the passivation properties of various dielectric films for this material and pointed out that the ZnS film forms a high-quality interface with freshly etched HgCdTe. However, this film is unstable at thermal cycles from room temperature to 80–90°C and has poorer dielectric properties compared with SiO_2 [6].

Our long-standing practice, however, has shown that an ZnS film can be successfully used not only in the fabrication of n^+–p junctions based on p-$Hg_{1-x}Cd_xTe$ with $x \approx 0.2$ as a mask for ion-implantation doping, but also for final passivation of photodiode structures. To increase the dielectric strength, the film was usually deposited by evaporation in three to five stages. The highest temperature of the wafers, which was reached during deposition due to heating by evaporator emission and release of the condensation heat, was ~110°C. In the context of the development of $Hg_{1-x}Cd_xTe$-based photodiodes, we investigated N_{ss} of the ZnS–CdHgTe interface and variations in N_{ss} during the fabrication of photodiodes, as well as during their long-term storage. These results are given below.

The capacitance–voltage (C–V) characteristics of MIS structures were measured using a setup based on an E7-12 device at 78 K for metal–ZnS–CdHgTe structures (metal = Al + In) at a frequency $f = 1$ MHz. The dispersion dependence of capacitance was recorded within the limits of a bias voltage at a metal electrode $V = \pm 20$ V with a step of 0.1 V. The area of the metal contact was $S = 0.5$ mm^2, the thickness of the ZnS layer was ~0.4–0.6 μm, and the dielectric capacitance was $C_d = 50–100$ pF. The capacitance variance can be seen in Figs. 1–4.

In the course of fabricating photodiodes, CdHgTe crystals with a passivation film are repeatedly subjected to the thermal effect during the deposition of In contacts ($T \approx 80–100$°C, $\tau \approx 5$ min) and during soldering on a Polycor substrate ($T \approx 115$°C, $\tau \approx 2$ min). An especially prolonged effect ($T \approx 90$°C, $\tau > 13$ h) is observed when photodiodes that are already fabricated are mounted in cryostats, when the devices are outgassed using a pumping setup and then (at $T \approx 60$°C, $\tau \geq 100$ h) again on a test bench in equipped with an NEM-02 ion-sputter pump. In this case, a variation in the state of the ZnS–CdHgTe interface can occur. To verify this fact, we measured the C–V characteristics of MIS structures

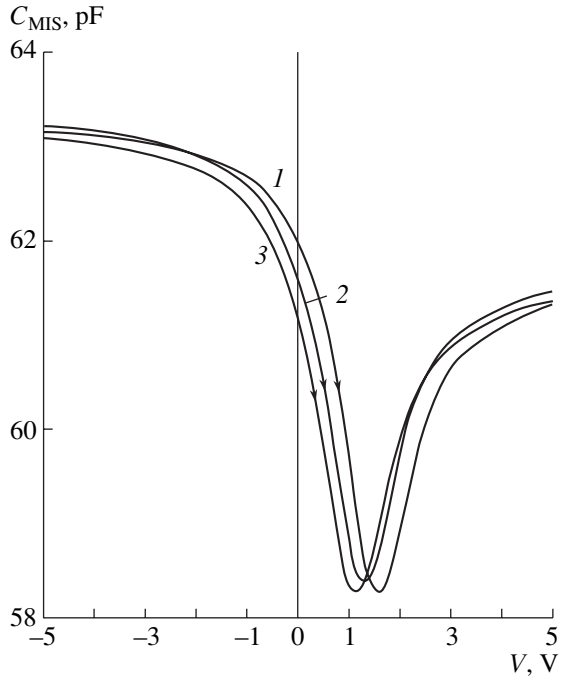

Fig. 1. Effect of heating in vacuum (T = 60°C) on the C–V characteristics of the ZnS–CdHgTe structure. Sample 4, x = 0.219, $p = 1.18 \times 10^{16}$ cm^{-3}, d_{ZnS} = 0.52 μm, the contact Al + In; τ = (*1*) 0, (*2*) 110, and (*3*) 283 h (table). The normalized surface potential for V = 0, $y = \varphi_s/k_0T$: +0.334 (curve *1*), +1.26 (curve *2*), and +2.1 (curve *3*).

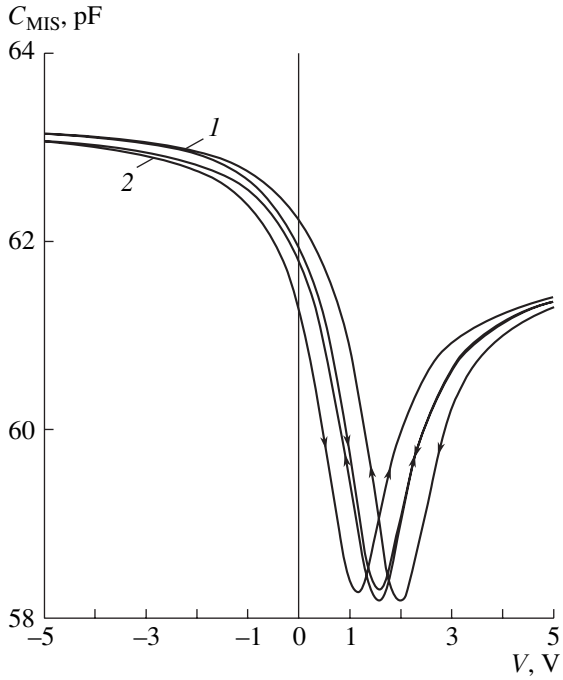

Fig. 2. Effect of heating in vacuum (T = 60°C) on the hysteresis of the C–V characteristic of the ZnS–CdHgTe structure: sample 4 (curves *1*, *2*) correspond to curves *1* and *2* in Fig. 1.

prior to and after the thermal treatment at various temperatures depending on time. These characteristics are shown in Figs. 1–4 and in the table. As was expected, they had a low-frequency shape, since the carrier lifetime for the samples investigated $\tau_n < 1/2\pi f$). The electrical and photoelectric parameters and characteristics of n^+–p junctions are determined mainly by a lightly doped region. Therefore, only the p-type material was investigated; as a result, the parameters of the ZnS–CdHgTe interface, Q_{ss} and N_{ss}, can be calculated from formulas for a parabolic band [7]:

$$C = C_sC_d/(C_s + C_d); \quad C_d = \varepsilon_d\varepsilon_0/d;$$
$$C_s = (q/k_0T)(\partial Q_s/\partial T)$$
$$= (\varepsilon_s\varepsilon_0/2L_D)|\{\delta[1 - \exp(-y)] - \delta^{-1}[1 - \exp(y)]\}/\{[\exp(-y) + y - 1] + \delta^{-1}[\exp(y) - y - 1]\}^{1/2}|, \quad (1)$$

$$Q_s = (k_0T/q)(\varepsilon_s\varepsilon_0/L_D)\{\delta[\exp(-y) + y - 1] + \delta^{-1}[\exp(y) - y - 1]\}^{1/2}. \quad (2)$$

Here, C is the measured capacitance, which consists of the series-connected capacitance of the surface layer of the space charge of semiconductor C_s and dielectric capacitance C_d (ZnS); Q_s is the charge of the surface layer of the semiconductor; $y = \varphi_s q/k_0T$ is the normalized surface potential; q is the elementary charge; k_0 is the Boltzmann constant; T is the temperature (in K); $\delta = p_0/n_i$; p_0 and n_i are the majority-carrier density and the intrinsic-carrier density in the p-CdHgTe bulk; $L_D = (\varepsilon_s\varepsilon_0k_0T/2n_iq^2)$ is the Debye screening length; and ε_s, ε_d, and ε_0 are the relative permittivities for CdHgTe, ZnS, and free space, respectively. For calculations, it is assumed that ε_s = 19.5 for compounds with $x \approx 0.2$ [8]; for ZnS, it is assumed that ε_d = 7.45 [6] and $\tilde{n}$ = 2.19 at the wavelength λ = 10.6 μm [9]. From the experimental C–V characteristic (Fig. 1), we find the smallest capacitance of the surface layer of semiconductor $C_{s,\,min} = C_dC_{min}/(C_d - C_{min})$, which corresponds to the condition of strong inversion of the space charge of this layer, expression (1), with the condition $y \geq 2\ln\delta$, and determine δ from $C_{s,\,min}$. For example, for sample 4 (curve *1*, Fig. 1): y = 16, δ = 2540 at x = 0.219 and E_g = 0.129 eV, and $n_i = 4.65 \times 10^{12}$ cm^{-3}; i.e., $p_0 = 1.18 \times 10^{16}$ cm^{-3}, $E_c - E_i$ = 0.044 eV, $F - E_v$ = 0.032 eV, $L_D = 8.82 \times 10^{-5}$ cm, d_{ZnS} = 0.52 μm, $C_{min} = 1.17 \times 10^{-8}$ F/cm^2, $C_{s,\,min} = 1.52 \times 10^{-7}$ F/cm^2, and the capacitance of flat bands C_{FB} = 61.22 pF with the area of the top metal contact $A = 5 \times 10^{-3}$ cm^2. Substituting δ and y into expression (2), we find $Q_s(y)$ and the density of the surface charge $Q_{ss}(y)$ from the equation of the voltage balance across the MIS structure: $Q_{ss}(y) = -[C_dV + Q_s(y)]$. We find the density of surface states by the differentiation of the $Q_{ss}(y)$ dependences; i.e., $N_{ss} = (1/q)(dQ_{ss}(y)/dy)$ (Figs. 5, 6). In the table, the values of

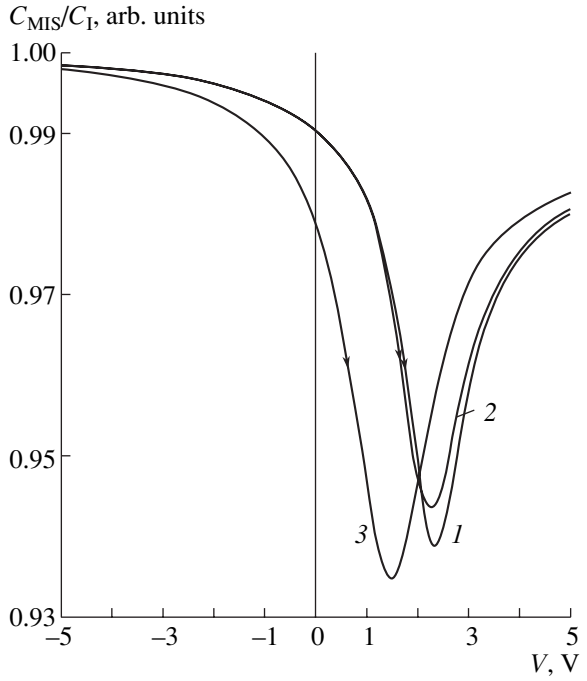

Fig. 3. Effect of treatment of the *p*-CdHgTe surface and subsequent heating of the Me–ZnS–CdHgTe structure on its *C–V* characteristics: (*1*) sample 5, (*2*) sample 6, and (*3*) sample 7. The normalized surface potential for $V = 0$, $y = \varphi_s/k_0T$: –1.36 (curve *1*), –1.15 (curve *2*), and +0.82 (curve *3*).

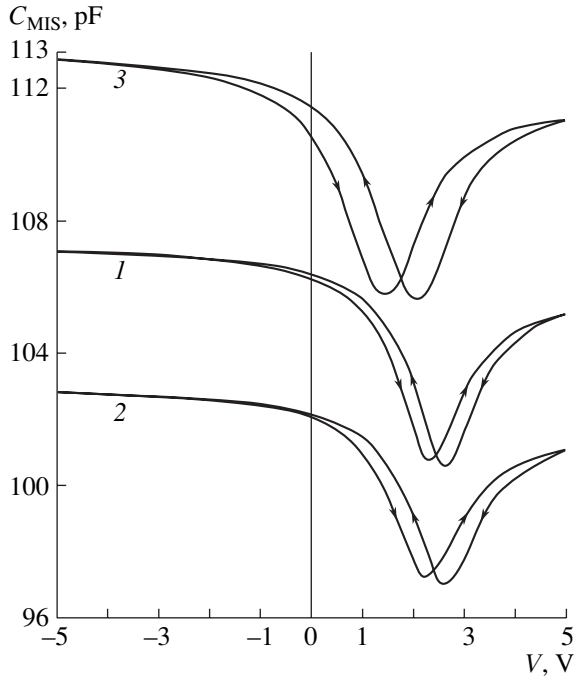

Fig. 4. Effect of treatment of the *p*-CdHgTe surface and subsequent heating of the Me–ZnS–CdHgTe structure on the hysteresis of its *C–V* characteristic: curves *1–3* correspond to curves *1–3* in Fig. 3.

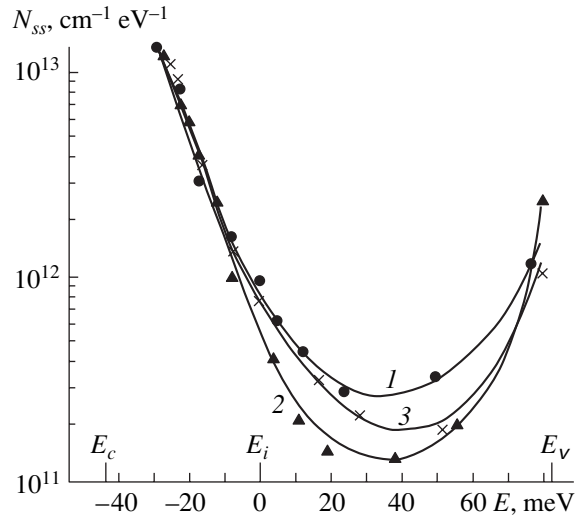

Fig. 5. Effect of heating in vacuum ($T = 60$°C) on the N_{ss} value for the ZnS–CdHgTe structure: sample 4, $x = 0.215$–0.223, $p = 8.7 \times 10^{15}$ cm^{-3}, $d_{ZnS} = 0.52$ μm, the contact Al + In; τ = (*1*) 0, (*2*) 110, and (*3*) 283 h. Curves *1–3* correspond to curves *1–3* in Fig. 1.

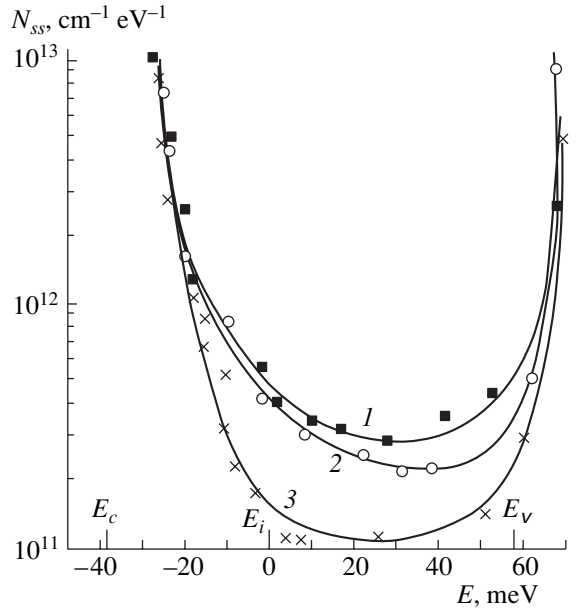

Fig. 6. Effect of treatment of the *p*-CdHgTe surface and subsequent heating of the Me–ZnS–CdHgTe structure on the value of N_{ss}. Curves *1–3* correspond to curves *1–3* in Fig. 3.

$N_{ss,\,mid}$ are listed, i.e., the densities of surface states $N_{ss,\,mid} = N_{ss}(V_{FB})/E_g$ averaged over E_g. In this case, $N_{ss}(V_{FB})$ is found from the relationship $N_{ss}(V_{FB}) = C_dV_{FB}/q$, and V_{FB} is the voltage of flat bands (table), which can be determined, specifically, from relationship (1) with the condition $y = 0$. In this case, $C_{s0}(y = 0) = q(\varepsilon_s\varepsilon_0p_0/k_0T)^{1/2}$, and $C_{FB} = C_{s0}C_d/(C_{s0} + C_d)$, from which we find V_{FB}.

Table

No. of wafer and MIS structure	Thermal treatment temperature, °C	Thermal treatment time, h	V_{FB}, V	$N_{ss,\,mid}$, 10^{11} cm^{-2} eV^{-1}
1	90	0	−0.553	5.40
		8	−0.719	5.47
		21	−0.849	4.40
		37	−0.839	5.23
2	90	0	−0.198	5.80
		21	−0.437	2.02
		37	−0.547	3.12
3	60	0	−0.049	2.13
		13	−0.12	2.10
		46	−0.566	3.16
		71	−0.254	2.09
		110	−0.304	2.16
		164	−0.376	2.21
		221	−0.365	1.85
		283	−0.411	2.02
		342	−0.494	2.10
4	60	0	+0.095	1.62
		46	−0.269	1.60
		71	−0.186	1.52
		110	−0.204	1.48
		164	−0.242	1.30
		283	−0.275	1.33

The experiments showed (see table and Figs. 1, 2) that variations in the fabrication conditions only slightly affect the state of the ZnS–CdHgTe interface. In this case, the negative voltages of flat bands V_{FB} indicated that ZnS–*p*-CdHgTe surface layer is enriched with majority carriers (holes), even if immediately after deposition of the ZnS film $V_{FB} > 0$ (see table, Fig. 1, sample 2). This should lead to a decrease in the leakage current of n^+–*p* junctions over the surface. In the *C*–*V* characteristics, narrow hysteresis loops were usually observed when applying the forward and reverse voltages to the top electrode (Figs. 3, 4), i.e., the charge of mobile ions in the film is insignificant. The treatment of the wafer surface prior to the deposition of the ZnS film and the mode of its deposition have a more significant effect on the interfacial properties (Figs. 3, 4). Specifically, curve *1* shows the results of boiling the *p*-CdHgTe wafer in methanol with the subsequent vacuum deposition of the ZnS film on a wafer whose temperature was $T = 90$°C. Curve *2* shows the results of boiling the wafer in acetone and deposition of ZnS at 90°C. Finally, curve *3* shows the results of boiling the wafer in acetone and deposition of ZnS at $T = 60$°C. However, the density of surface states N_{ss} in this case is also no higher than that of the high-quality structures in [1–5].

From the above, it is possible to conclude that the low N_{ss} (Figs. 5, 6) in our structures, the negative V_{FB} values (see table), and the relatively high breakdown voltages $V \approx 10$–15 V of the ZnS film indicate that the ZnS film, the methods of depositing it, and the modes of outgassing cryostats may be considered satisfactory for the passivation by coating the n^+–*p* junctions based on *p*-CdHgTe with $x \approx 0.2$. It should also be added that the long-term storage of crystals with n^+–*p* junctions at normal room temperature (20–25°C) in air for ≈15 years caused no degradation of operational parameters such as the differential resistance at a zero bias R_0, voltage sensitivity S_v, and detectivity D^*. Such n^+–*p* junctions were also mounted in cryostats after storage, the standard cycle of outgassing was carried out, the photodiodes were delivered to the customers, and, judging by their photoelectric parameters, they did not subsequently fail.

Thus, when investigating the ZnS–$Cd_xHg_{1-x}Te$ interface using the *C*–*V* characteristics of the MIS structures, we found that the density of states N_{ss} at such an interface is no higher than at the SiO_2–$Cd_xHg_{1-x}Te$ interface or at the interface with native anodic oxide. This density is within the limits $N_{ss} = (1–6) \times 10^{11}$ cm^{-2} eV^{-1}. The ZnS film satisfactorily fulfilled the function of passivation of the surface of the n^+–*p* junctions based on *p*-$Cd_xHg_{1-x}Te$. It was also found that during the long-term storage (as long as ≈15 years) in air at room temperature, no degradation of the differential resistance R_d, current sensitivity S_i, and detectivity D^* was observed. These structures were later successfully used as sensitive elements.

REFERENCES

1. B. K. Janousek, R. C. Carscallen, and P. A. Bertran, J. Vac. Sci. Technol. A **1**, 1723 (1983).
2. J. A. Wilson and V. A. Cotton, J. Vac. Sci. Technol. A **3**, 199 (1985).
3. Y. Nemirovsky, L. Burstein, and I. Kidron, J. Appl. Phys. **58**, 366 (1985).
4. Y. Nemirovsky, R. Adar, A. Kornfeld, and I. Kidron, J. Vac. Sci. Technol. A **4**, 1986 (1986).
5. N. Kajihara, G. Sudo, Y. Miyamoto, and K. Tanikawa, J. Electrochem. Soc. **135**, 1252 (1988).
6. Y. Nemirovsky and G. Bahir, J. Vac. Sci. Technol. A **7**, 450 (1989).
7. M. V. Whelan, Philips Res. Rep. **20**, 620 (1965).
8. D. L. Carter, M. A. Kinch, and D. D. Buss, J. Phys. Chem. Solids Suppl. **32**, 273 (1971).
9. A. Campbell and C. Hayman, Proc. SPIE **915**, 79 (1988).

Translated by N. Korovin

Semiconductors, Vol. 37, No. 12, 2003, pp. 1387–1389. Translated from Fizika i Tekhnika Poluprovodnikov, Vol. 37, No. 12, 2003, pp. 1435–1437.

SEMICONDUCTOR STRUCTURES, INTERFACES, AND SURFACES

Mechanisms of Photocurrent Generation in In_2O_3–InSe Heterojunctions

V. P. Makhniy and O. I. Yanchuk

Fed'kovich National University, Chernovtsy, 58012 Ukraine

Submitted December 16, 2002; accepted for publication January 27, 2003

Abstract—Spectral and integral characteristics of In_2O_3–InSe heterojunctions fabricated by oxidation of indium monoselenide substrates were studied. It was established that the photocurrent is determined by photogeneration of carriers in the space charge region of the structure via isolated deep levels. © *2003 MAIK "Nauka/Interperiodica".*

The interest in studies of diodes based on layered semiconductors is primarily due to the possibility of using these diodes as photoelectric analyzers of light polarization [1]. Heterojunctions with a conducting oxide, e.g., In_2O_3 with energy gap $E_g \approx 3.6$ eV [2], as a wide-bandgap component may be promising in this regard. This oxide can be easily formed on indium monoselenide (InSe) by thermal oxidation of a wafer; the oxidation occurs simultaneously on all faces and the unnecessary parts of the oxide coating are removed during the fabrication process of a heterojunction [3]. Structures of this kind show a rather high coefficient of natural photopleochroism (~90%), which is observed when illuminating the substrate in the direction perpendicular to the crystallographic axis *c*. The oblique incidence of polarized light onto the frontal face of a rectifying structure gives rise to another kind of photopleochroism: induced photopleochroism [4]. A specific feature of this phenomenon is that it can be observed on diodes made of any semiconductors, irrespective of their structural and phase state. At the same time, a superposition of natural and induced photopleochroism would be expected to occur under these illumination conditions for layered materials. This may extend the functional capabilities of spectropolarimetric devices on their base. However, reports of the physical properties of heterostructures consisting of indium oxide and indium monoselenide are few in number [5, 6]. The present study analyzes mechanisms governing the observed integral and spectral characteristics of In_2O_3–InSe heterojunctions.

Single crystals of InSe were grown by the Bridgman method and doped with Cd in the course of synthesis to obtain *p*-type conduction. The technology of fabrication of the heterojunctions is similar to that described in [3], and structures with an oxide layer parallel to the cleavage plane were chosen for study. The electrical and photoelectric characteristics were measured using the well-known techniques, with the heterojunctions illuminated from the In_2O_3 side. The illuminance L was varied within four orders of magnitude, using a set of calibrated light filters. In doing so, the spectral composition of light remained the same at any L. The structures exhibited clearly pronounced diode characteristics with a rectification coefficient of no less than 10^4 at 300 K and bias $V = 0.5$ V. Under forward biases exceeding 1.5 V, the dark current–voltage (I–V) characteristics are described by a linear relation of the type

$$V = V_i + R_0 I, \tag{1}$$

where I is current, and V_i is the cutoff voltage. In the first approximation, V_i corresponds to the height of the potential barrier, $\varphi_0 \approx eV_i$, being equal to 0.8–0.9 V for the structures studied. The residual resistance R_0 is within the range 10^4–10^5 Ω at a temperature of T = 300 K, and the $R_0(T)$ dependence is approximated with a straight line in the coordinates $\ln R_0 - 10^3/T$ with an energy slope of ~0.45 eV. This value correlates with the depth of acceptor levels in InSe:Cd crystals [7]. In addition, the experimental value of R_0 is in good agreement with the resistance of the heterojunction base, calculated taking into account its geometric dimensions and electrical resistivity. The results presented indicate that the intermediate high-resistivity layer at the interface, which may appear in heterostructure fabrication, is not formed in this case. Also noteworthy is the fact that the junction interface lies deep in the substrate since In_2O_3 is synthesized via oxidation of In atoms in the base crystal. This should lead to a weaker influence of surface levels on the photoelectric properties of the heterojunction and, first and foremost, on the spectral distribution of sensitivity S_ω.

As can be seen from Fig. 1, the experimental photosensitivity spectrum of the heterojunction is in satisfac-

1063-7826/03/3712-1387$24.00

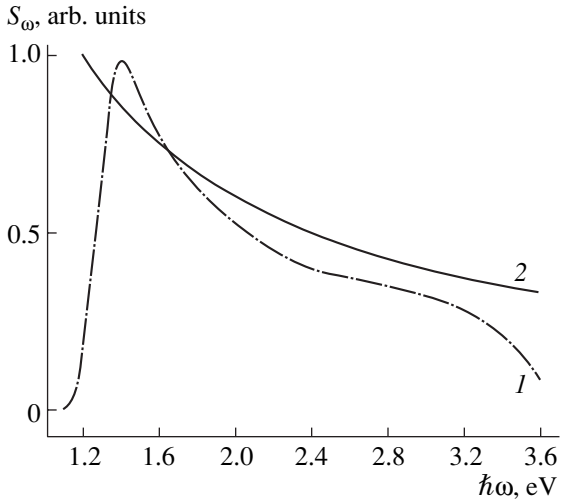

Fig. 1. Normalized photosensitivity spectra of the In_2O_3–InSe heterojunction: (*1*) experiment and (*2*) calculation by (2).

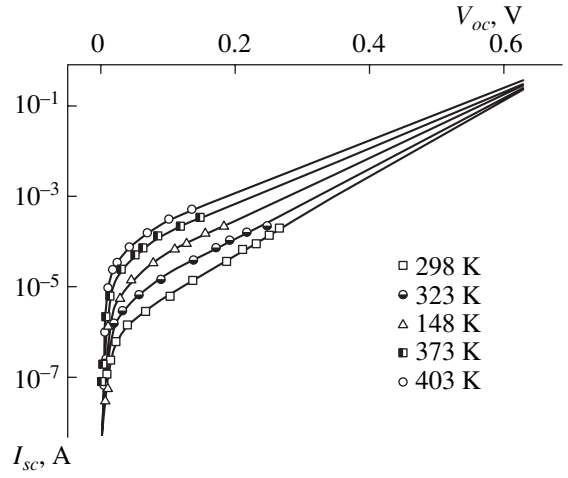

Fig. 2. Light *I–V* characteristics of the In_2O_3–InSe heterojunction at different temperatures. Points, experiment; solid lines, calculation using formulas (3) and (4) at $A = 3 \times 10^{-6}$ A.

tory agreement with the known distribution for the ideal photodiode [2]

$$S_\omega = \text{const}\eta/\hbar\omega, \tag{2}$$

where η is the quantum yield of the photoelectric effect, and $\hbar\omega$ is the photon energy. It is noteworthy that the peak energy of curve *1* differs from the energy gap E_g of InSe, which is equal to ~1.2 eV at 300 K [8]. A similar shift is observed for *p*-GaSe–*n*-InSe heterojunctions, and the reasons for its appearance were considered in detail in [9]. The main reason is that η and the surface recombination rate depend on $\hbar\omega$, which is not accounted for by formula (2). The lack of sensitivity at $\hbar\omega \gtrsim 3.5$ eV indicates that photocarriers are mainly generated in the narrow-gap component of the heterojunction, with the oxide acting as a wide-bandgap window only. At the same time, spectral studies give no answer to the question of what the dominating mechanism of photocarrier generation is. An answer can, in particular, be provided by an analysis of how the short-circuit current I_{sc} depends on the open-circuit voltage V_{oc}.

The light *I–V* characteristic of the diode is described by the expression [10]

$$I = I_0[\exp(eV/nkT) - 1] - I_L, \tag{3}$$

where I_0 is the saturation current; I_L, the current due to illumination; *n*, the ideality factor of the *I–V* characteristic, determined by the current transport mechanism; and *k*, the Boltzmann constant. From Eq. (3) it follows that, with an open external circuit ($I = 0$), $V = V_{oc}$ and

$$I_L = I_{sc} = I_0[\exp(eV_{oc}/2kT) - 1]. \tag{4}$$

As can be seen from Fig. 2, the experimental $I_{sc}(V_{oc})$ dependences are described at $eV \geq 3kT$, when plotted on a semilogarithmic scale, by straight lines with slope equal to $e/2kT$. This is evidence in favor of photocarrier generation in the space-charge region via isolated deep levels.

The temperature dependence of I_0 is determined by the energy gap of the material in which the space charge is localized; i.e.,

$$I_0 = A\exp(-E_g/2kT), \tag{5}$$

where *A* is a parameter whose temperature dependence is weaker than exponential. The value of *A* can be found at 300 K from expression (3) after substitution of the known values of E_g [7] and I_0 (experiment). The resulting value $A \approx 3 \times 10^{-6}$ A makes it possible to calculate, using the corresponding formulas, the cutoff current and *I–V* characteristics at any temperature from the range under study taking account of the temperature coefficient of E_g, which is $\sim 3.7 \times 10^{-4}$ eV/K for indium monoselenide [8].

The good agreement between the experimental and calculated *I–V* characteristics strongly suggests that the photocurrent in the heterostructures studied is a consequence of carrier generation in the space-charge region via isolated levels. The above-mentioned acceptor levels lying close to the midgap of InSe may serve as these levels. According to the Sah–Noyce–Shockley theory, this should ensure a rate of generation close to the maximum value. At the same time, definitive clarification of the nature of the deep centers requires further research, which is beyond the scope of the present study.

REFERENCES

1. Yu. V. Rud', Izv. Vyssh. Uchebn. Zaved. Fiz., No. 8, 68 (1986).
2. S. Sze, *Physics of Semiconductor Devices*, 2nd ed. (Wiley, New York, 1981; Mir, Moscow, 1984).
3. V. N. Katerinchuk and M. Z. Kovalyuk, Pis'ma Zh. Tekh. Fiz. **18**, 70 (1992) [Sov. Tech. Phys. Lett. **18**, 394 (1992)].
4. F. P. Kesamanly, V. Yu. Rud', and Yu. V. Rud', Fiz. Tekh. Poluprovodn. (St. Petersburg) **33**, 513 (1999) [Semiconductors **33**, 483 (1999)].
5. V. N. Katerinchuk and M. Z. Kovalyuk, Pis'ma Zh. Tekh. Fiz. **23** (10), 1 (1997) [Tech. Phys. Lett. **23**, 377 (1997)].
6. Z. D. Kovalyuk, V. N. Katerinchuk, and T. V. Betsa, Opt. Mater. **17**, 297 (2001).
7. S. Shigetomi, H. Ohkubo, and T. Ikari, J. Phys. Chem. Solids **51** (1), 91 (1990).
8. I. Cammasel, P. Merle, H. Mathieu, and A. Chevy, Phys. Rev. B **17**, 4718 (1978).
9. Z. D. Kovalyuk, V. P. Makhniĭ, and O. I. Yanchuk, Visn. L'viv. Derzh. Univ., Ser. Fiz. **34**, 218 (2001).
10. A. L. Fahrenbruch and R. H. Bube, *Fundamentals of Solar Cells* (Academic, New York, 1987; Énergoatommash, Moscow, 1987).

Translated by M. Tagirdzhanov

Semiconductors, Vol. 37, No. 12, 2003, pp. 1390–1399. Translated from Fizika i Tekhnika Poluprovodnikov, Vol. 37, No. 12, 2003, pp. 1438–1448.

LOW-DIMENSIONAL SYSTEMS

Spin Depolarization in Spontaneously Polarized Low-Dimensional Systems

I. A. Shelykh*, N. T. Bagraev^, and L. E. Klyachkin****

**St. Petersburg State Technical University, Politekhnicheskaya ul. 29, St. Petersburg, 195251 Russia*

***Ioffe Physicotechnical Institute, Russian Academy of Sciences, Politekhnicheskaya ul. 26, St. Petersburg, 194021 Russia*

^e-mail: impurity.dipole@mail.ioffe.ru

Submitted April 1, 2003; accepted for publication April 1, 2003

Abstract—Conditions for the appearance of a spontaneous spin polarization in low-dimensional systems in zero magnetic field are analyzed for the case of low occupation of the lowest quantum-confinement subbands, when the energy of exchange interaction of charge carriers exceeds their kinetic energy. In terms of the Hartree–Fock approximation, the critical densities above which complete spin depolarization of the charge-carrier gas occurs, were determined for quasi-two-dimensional and quasi-one-dimensional systems. The emphasis is on the probable interrelation of the spin depolarization, first, with the transition of a two-dimensional gas to a metallic state and, second, with the evolution of the "$0.7(2e^2/h)$ feature," which is split off from the first step in the staircase function of the quantum conductance of a one-dimensional channel and varies in height from e^2/h to $(3/2)e^2/h$ as the density of charge carriers increases. © *2003 MAIK "Nauka/Interperiodica".*

1. INTRODUCTION

Progress in nanotechnology makes it possible to fabricate low-dimensional semiconductor systems with low density of high-mobility charge carriers, which exhibit ballistic behavior under the condition $k_BT\tau/\hbar > 1$ (where $\hbar/k_BT$ is the time of electron–electron interaction and $\tau = m^*\mu/e$ is the transport relaxation time) [1–33]. In contrast to the diffusion mode ($k_BT\tau/\hbar < 1$), in the case of ballistic transport the role of spin correlations is considerably enhanced [2–4]. Among their most dramatic manifestations in the localization and transport processes are the metal–insulator transition observed in silicon MOS transistors [1] and in Si/Ge [6] and GaAs/AlGaAs [7, 8] heterojunctions and the appearance of the "$0.7(2e^2/h)$ feature," which is split off from the first step in the staircase function of the quantum conductance of a one-dimensional channel [26–33]. Both effects are probably related to the spontaneous spin polarization of a two-dimensional (2D) or one-dimensional (1D) gas of charge carriers in zero magnetic field [6, 15–24, 34–40].

The spin nature of the metallic state found to exist in a 2D electron or hole gas, contrary to the prediction of the one-parameter scaling theory of localization [5], manifests itself, first of all, in the destruction of this state by a magnetic field applied in the plane of the 2D system [2, 9]. However, the conclusion, based on the measurements of field dependences of the conductance, that a spontaneous polarization exists in a 2D electron gas with a density close to the critical density n_c, corresponding to the metal–insulator transition [12, 15], is not confirmed by the measurements of Shubnikov–de Haas oscillations and spin susceptibility. The latter studies indicate that a trend towards ferromagnetic ordering is accompanied by a transformation of a normal 2D metal into a 2D insulator without the formation of a spontaneously polarized state with extended wave functions [9, 14, 16]. Thus, there remains the basic question of the interrelationship between the metal–insulator transition and the values of the critical density of charge carriers above which a complete spin depolarization of the spontaneously polarized 2D gas occurs.

In the case of 1D systems, two experimental observations should be noted that indicate the importance of the spin component for the behavior of the $0.7(2e^2/h)$ feature, which is split off from the first step in the staircase quantum conductance of a 1D channel. First, it was found that the electron g factor increases severalfold (from 0.4 to 1.3) as the number of occupied 1D subbands decreases [26]. Second, the height of the $0.7(2e^2/h)$ feature of the first step evolves to a value of $0.5(2e^2/h)$ with increasing external magnetic field applied along the channel [26–30]. These results stimulated the analysis of possible mechanisms of a spontaneous spin polarization that may appear in semiconductor quantum wires (QWRs), despite the theoretical prediction that a ferromagnetic state cannot exist in ideal 1D systems in the absence of a magnetic field [41]. These studies were carried out in the framework of the Kohn–Sham mean-field approximation for the case of ultralow linear density of charge carriers, when the energy of exchange interaction starts to exceed the kinetic energy in zero magnetic field. This approach enables one to qualitatively describe the current–voltage characteristics of a polarized 1D channel [34–40]. However, the question of the behavior of the $0.7(2e^2/h)$ feature of the first quantum step with the onset of spin

depolarization, which increases with increasing linear density of charge carriers, remains open; this circumstance considerably hinders analysis of the electron polarization in 1D systems at finite temperatures.

In this study, the critical densities for a quasi-2D and a quasi-1D gas of charge carriers above which complete depolarization occurs—probably, interrelated with the metal–insulator transition and the disappearance of the $0.7(2e^2/h)$ feature of the first step in the quantized conductance—are calculated within the Hartree–Fock approximation, which is used to determine the conditions for the appearance of a spontaneous spin polarization in quasi-2D and quasi-1D systems in zero magnetic field.

2. SPONTANEOUS SPIN POLARIZATION IN LOW-DIMENSIONAL SYSTEMS IN ZERO MAGNETIC FIELD

Let us consider a system of fermions described by the Schrödinger equation $H\Psi = E\Psi$ with $H = H_0 + H_1$; here, H_0 is the Hamiltonian of noninteracting fermions, which depends on the dimensionality of the system under study, and the term H_1 accounts for the interaction of fermions.

The form of H_0 depends on the dimensionality of the system under consideration. In the three-dimensional (3D) case, it is the kinetic-energy operator

$$H_0^{3D} = \frac{1}{2m}\sum_{j=1}^{N}\hat{\mathbf{p}}_\mathbf{j} = -\frac{\hbar^2}{2m}\sum_{j=1}^{N}\nabla_\mathbf{j}^2. \quad (1)$$

The single-particle wave functions of unperturbed motion are given by plane waves

$$\psi_\mathbf{k}(\mathbf{r}) = \frac{1}{\sqrt{\Omega_{3D}}}e^{i\mathbf{kr}}, \quad (2)$$

where Ω_{3D} is the 3D volume of the system.

In the consideration of 2D systems—in particular, the case of a fermion gas in a planar quantum well (QW)—the potential energy responsible for the quantum confinement of the charge-carrier motion in the direction z normal to the QW plane should be added to the kinetic energy:

$$H_0^{2D} = \left(\sum_{j=1}^{N}\left(\frac{\mathbf{p}_\mathbf{j}^2}{2m^*} + U(z_j)\right)\right). \quad (3)$$

Unperturbed single-particle wave functions are described by the products of size-quantization wave functions and plane waves parallel to the QW:

$$\psi_{k,m}(\mathbf{r}) = \frac{1}{\sqrt{\Omega_{2D}}}e^{i\mathbf{k\rho}}\varphi_m(z). \quad (4)$$

Here, m is the number of the subband of the quantum confinement in the direction z, $\boldsymbol{\rho} = \mathbf{i}x + \mathbf{j}y$, and Ω_{2D} is the 2D volume (a quantity with the dimension of area).

Finally, in 1D systems, the motion is quantized in two directions (x, y), and the Hamiltonian for noninteracting particles has the form

$$H_0^{1D} = \sum_{j=1}^{N}\left(\frac{\mathbf{p}_\mathbf{j}^2}{2m} + U(x_j, y_j)\right). \quad (5)$$

The corresponding unperturbed wave functions can be written as

$$\psi_{k,m}(\mathbf{r}) = \frac{1}{\sqrt{\Omega_{1D}}}e^{ikz}\varphi_m(\boldsymbol{\rho}), \quad (6)$$

where m is the number of the subband of the quantum confinement in the plane $\boldsymbol{\rho} = \mathbf{i}x + \mathbf{j}y$, and Ω_{1D} is the 1D volume (a quantity with the dimension of length).

The interaction operator is the same for all three cases; it is given by

$$H_1 = \frac{1}{2}\sum_{i\neq j}V(|\mathbf{r}_i - \mathbf{r}_j|), \quad (7)$$

where

$$V(|\mathbf{r}_i - \mathbf{r}_j|) = \frac{e^2}{|\mathbf{r}_i - \mathbf{r}_j|}. \quad (8)$$

In the second-quantized representation,

$$H_1 = \frac{1}{2}\sum_{i\neq j}\langle KL|V|MQ\rangle c_K^+ c_L^+ c_Q c_M, \quad (9)$$

where each of the subscripts K, L, M, and Q stands for a particle wave vector, the number of the quantum-confinement subband (for systems of reduced dimensionality), and the spin.

If the density of noninteracting carriers is sufficiently low so that only the lowest quantum-confinement subband is occupied, the total energy of the electron gas equals its kinetic energy, and the energy density can easily be calculated both for a 2D and a 1D gas of charge carriers:

$$\varepsilon_{kin} = \sum_{k<k_F}\frac{\hbar^2k^2}{2m}, \quad (10)$$

where k_F is the Fermi wave vector.

Accordingly,

$$\varepsilon_{kin}^{2D} = \sum_{k<k_F}g_s\frac{\hbar^2k^2}{2m^*} = \frac{\hbar^2}{16\pi m^*}g_s k_F^4 = \frac{\pi\hbar^2 n_{2D}^2}{m^* g_s}, \quad (11)$$

$$\varepsilon_{kin}^{1D} = \sum_{k<k_F}g_s\frac{\hbar^2k^2}{2m} = \frac{\hbar^2 g_s}{12\pi m}k_F^3 = \frac{\pi\hbar^2 n_{1D}^3}{12 m g_s^2}. \quad (12)$$

The value of k_F is determined from the conditions

$$\pi k_F^2 = \frac{(2\pi)^2}{g_s} n_{2D} \tag{13}$$

and

$$k_F = \frac{\pi}{g_s} n_{1D}; \tag{14}$$

here, n_{2D} and n_{1D} are the densities of a 2D and a 1D gas of charge carriers, respectively, and g_s is the spin factor, which is equal to the number of electrons per unit cell of phase space. For an unpolarized state, $g_s = 2$; for a completely polarized state, $g_s = 1$. The values $1 < g_s < 2$ correspond to the partial spin polarization of a 2D or a 1D gas of charge carriers.

Let us consider the possibility of the appearance of a spontaneous spin polarization due to the exchange interaction in low-dimensional systems. A polarized state of 2D and 1D gases of noninteracting fermions is always energetically unfavorable because its kinetic energy is always higher than the kinetic energy of an unpolarized state. However, for a system of interacting particles, there is an additional energy term E_1, which can be represented by the following infinite sequence of diagrams:

$\varepsilon_{\text{core}} + \varepsilon_{\text{el-el}}$

(15)

It can easily be seen that exchange diagrams 3 and 5 depend substantially on the spin polarization of the system. Indeed, the interaction is independent of the spin, which implies spin conservation at the diagram vertices. Thus, only particles with the same spin may be involved in the processes described by the exchange diagrams; this means that the contribution from these diagrams is more significant for polarized than for unpolarized systems. Since the contribution from diagram 2 is negative, a spin-polarized state may be energetically more favorable than an unpolarized state.

We limit our discussion to the first two diagrams, which means that the particle interaction is taken into account within the Hartree–Fock approximation. Thus,

$$E_1 = \frac{1}{2} \sum_{E_K, E_L < E_F} [\langle KL|V|KL\rangle - \langle KL|V|LK\rangle]. \tag{16}$$

Here, the first term is the Hartree correction and the second term is the Fock correction to the exchange energy; the summation is carried out both over spatial and spin variables. In the thermodynamic limit ($N \longrightarrow \infty$, $\Omega \longrightarrow \infty$, and $N/\Omega = n = \text{const}$), the first term diverges; however, this divergence is compensated by the term describing the interaction with a positively charged background. Thus, in the first order, the exchange-interaction plays a decisive role. Below, we consider its behavior in 2D and 1D systems.

2.1. Exchange Interaction in a Quasi-2D System

The matrix element of the exchange interaction for electrons in a QW can be written as

$$\langle KL|V|LK\rangle = \frac{e^2}{\Omega_{2D}^2} \frac{e^{-i\mathbf{k}\boldsymbol{\rho}'} e^{-i\mathbf{l}\boldsymbol{\rho}''} e^{i\mathbf{l}\boldsymbol{\rho}'} e^{i\mathbf{k}\boldsymbol{\rho}''}}{\sqrt{|\boldsymbol{\rho}' - \boldsymbol{\rho}''|^2 + (z' + z'')^2}}$$
$$\times |\varphi(z')|^2 |\varphi(z'')|^2 d\boldsymbol{\rho}' d\boldsymbol{\rho}'' dz' dz'' \tag{17}$$
$$= \frac{e^2}{\Omega_{2D}} \int \frac{e^{-i\mathbf{k}\boldsymbol{\rho}} e^{i\mathbf{l}\boldsymbol{\rho}}}{\sqrt{\boldsymbol{\rho}^2 + (z' - z'')^2}} |\varphi(z')|^2 |\varphi(z'')|^2 d\boldsymbol{\rho} dz' dz'',$$

where $\boldsymbol{\rho} = \mathbf{i}x - \mathbf{j}y$ describes the position of a particle in the QW plane and the z axis is perpendicular to this plane. Here, a transformation of the variables was performed: $\boldsymbol{\rho} = \boldsymbol{\rho}' - \boldsymbol{\rho}''$ and $\mathbf{P} = (\boldsymbol{\rho}' + \boldsymbol{\rho}'')/2$. The integral over $\mathbf{P}$ is equal to the sample area Ω_{2D}. Thus, the expression for the exchange-interaction energy has the form

$$E_{\text{exc}} = -\frac{1}{2} \sum_{K, L < k_f} \langle KL|V|LK\rangle = -\frac{g_s e^2 \Omega_{2D}}{2(2\pi)^4} \int e^{-i\mathbf{k}\boldsymbol{\rho}} d\mathbf{k}$$
$$\times \int e^{i\mathbf{l}\boldsymbol{\rho}} d\mathbf{l} \int \frac{|\varphi(z')|^2 |\varphi(z'')|^2}{\sqrt{\boldsymbol{\rho}^2 + (z' - z'')^2}} d\boldsymbol{\rho} dz' dz'', \tag{18}$$

where the spin factor g_s appears due to the summation over spins. Integrating over $\mathbf{k}$ and $\mathbf{l}$ yields

$$E_{\text{exc}} = -\frac{e^2 k_F^2 \Omega_{2D}}{4\pi} \int |\varphi(z)|^2 |\varphi(z')|^2 dz dz'$$
$$\times \int_0^\infty \frac{J_1^2(k_F\rho)}{\rho \sqrt{\rho^2 + (z' - z'')^2}} d\rho, \tag{19}$$

where $J_1(k_F\rho)$ is the Bessel function. This expression contains the integral

$$I = \int_0^\infty \frac{J_1^2(k_F\rho)}{\rho \sqrt{\rho^2 + (z - z')^2}} d\rho = k_F \int_0^\infty \frac{J_1^2(u)}{u \sqrt{u^2 + \alpha^2}} d;$$

here, $\alpha = k_F|z - z'| \approx k_F d$ (d is the QW width). It is reasonable to estimate this integral under the condition

$$k_F d \ll 1, \tag{20}$$

which corresponds to the case of low occupation of the lowest quantum-confinement subbands. It will be seen below that the validity of this condition is an important factor for the appearance of spontaneous polarization in a 2D system. In this case, $I \approx k_F \int_0^\infty \frac{J_1^2(u)}{u^2} du \approx A k_F$ (where $A \approx 0.424$). Thus, we obtain the following

expression for the density of the exchange-interaction energy in a 2D gas of charge carriers:

$$\varepsilon_{exc} = E_{exc}/\Omega_{2D} = -\frac{g_s A e^2 k_F^2}{4\pi}\int |\varphi(z')|^2|\varphi(z')|^2 dz'dz'' = g_s\frac{Ae^2k_F^2}{4\pi} = -\frac{\beta_{2D}}{g_s^{1/2}}n_{2D}^{3/2}. \quad (21)$$

Here, $\beta_{2D} = 2\sqrt{\pi}Ae^2$. We conclude that ε_{exc} is negative and does not depend on the wave functions of noninteracting particles, i.e., on the shape of the QW. Actually, the character of its dependence on n_{2D} can be determined by considering the dimensions. We stress once more that formula (21) for the density of the exchange-interaction energy of a 2D electron gas is valid only for sufficiently low particle densities, when condition (20) is satisfied.

Let us estimate the value of k_F corresponding to the onset of the filling of the second quantum-confinement subband of a QW. The position of the bottom of the jth subband in a rectangular well is given by $E_j = \pi^2\hbar^2j^2/2m^*d^2$; thus, the wave vector k_0 corresponding to the onset of the filling of the second subband can be estimated from the following relations: $E_2 - E_1 \approx 3\pi^2\hbar^2/2m^*d^2 \approx \hbar^2k_0^2/2m^*$, whence $k_0d \approx \sqrt{3}\pi \approx 5.44$. Consequently, condition (20) will not be satisfied automatically in any QW with a single occupied subband, and it is interesting to estimate the integral I for the other limiting case: $k_Fd \gg 1$. In this case, $I \approx B/|z - z'|$ (where $B \approx 0.498$). Accordingly, for the density of the exchange energy we obtain

$$\varepsilon_{exc} = -g_s\frac{Be^2k_F^2}{4\pi}\int\frac{|\varphi(z')|^2|\varphi(z'')|^2}{|z-z'|}dz'dz'' = -\chi_{2D}n_{2D}, \quad \chi_{2D} \approx Be^2\int\frac{|\varphi(z')|^2|\varphi(z'')|^2}{|z-z'|}dz'dz''. \quad (22)$$

Thus, there is an essential difference in the character of the dependence of the exchange-interaction energy on the charge-carrier density in a 2D system in the cases of high and low densities. Interestingly, in the limiting case of high density, the exchange energy does not depend on the degree of polarization, since, apparently, the exchange interaction in 2D systems is short-range in the k space.

2.2. Exchange Interaction in a Quasi-1D System

The matrix element of the exchange interaction for electrons in a QWR has the form

$$\langle KL|V|LK\rangle = \frac{e^2}{\Omega_{1D}^2}\frac{e^{-ikz'}e^{-ilz''}e^{ilz'}e^{ikz''}}{\sqrt{|\boldsymbol{\rho}' - \boldsymbol{\rho}''|^2 + (z'+z'')^2}} \times |\varphi(\boldsymbol{\rho}')|^2|\varphi(\boldsymbol{\rho}'')|^2 d\boldsymbol{\rho}'d\boldsymbol{\rho}''dz'dz'' \quad (23)$$

$$= \frac{e^2}{\Omega_{1D}}\int\frac{e^{-ikz}e^{ilz}}{\sqrt{|\boldsymbol{\rho}' - \boldsymbol{\rho}''|^2 + z^2}}|\varphi(\boldsymbol{\rho}')|^2|\varphi(\boldsymbol{\rho}'')|^2 d\boldsymbol{\rho}'d\boldsymbol{\rho}''dz$$

(where the z coordinate coincides with the wire axis). Here, a transformation of the variables was performed: $z = z' - z''$ and $Z = (z' + z'')/2$, with the integral over Z being equal to the sample length Ω_{1D}. Thus, the expression for the exchange-interaction energy can be written as

$$E_{exc} = -\frac{1}{2}\sum_{K,\,L<k_F}\langle KL|V|LK\rangle = -g_s\frac{e^2\Omega_{2D}}{2(2\pi)^2}\int_{-k_F}^{k_F}e^{ikz}dk \times \int_{-k_F}^{k_F}e^{ilz}dl\int\frac{|\varphi(\boldsymbol{\rho}')|^2|\varphi(\boldsymbol{\rho}'')|^2}{\sqrt{|\boldsymbol{\rho}' - \boldsymbol{\rho}''|^2 + z^2}}d\boldsymbol{\rho}'d\boldsymbol{\rho}''dz = -g_s\frac{e^2\Omega_{1D}}{2\pi^2}\int\frac{\sin^2(k_Fz)}{z^2\sqrt{|\boldsymbol{\rho}' - \boldsymbol{\rho}''|^2 + z^2}}dz \times \int|\varphi(\boldsymbol{\rho}')|^2|\varphi(\boldsymbol{\rho}'')|^2 d\boldsymbol{\rho}'d\boldsymbol{\rho}''. \quad (24)$$

Making another substitution, $u = z/|\boldsymbol{\rho}' - \boldsymbol{\rho}''|$ and $\alpha = k_F|\boldsymbol{\rho}' - \boldsymbol{\rho}''|$, we transform the integral over z and obtain the following expression for the exchange-energy density in a quasi-1D system:

$$\varepsilon_{exc} = E_{exc}/\Omega_{1D} = -g_s\frac{e^2}{2\pi^2}\int\frac{|\varphi(\boldsymbol{\rho}')|^2|\varphi(\boldsymbol{\rho}'')|^2}{|\boldsymbol{\rho}' - \boldsymbol{\rho}''|^2}I(\alpha)d\boldsymbol{\rho}'d\boldsymbol{\rho}''. \quad (25)$$

Here,

$$I(\alpha) = \int_{-\infty}^{+\infty}\frac{\sin^2(\alpha u)}{u^2\sqrt{1+u^2}}du.$$

Estimating this integral in the limiting case of low linear densities

$$\alpha = k_F|\boldsymbol{\rho}' - \boldsymbol{\rho}''| \ll 1, \quad (26)$$

we obtain

$$I(\alpha) \approx \alpha^2\left(-\frac{1}{2}\ln\alpha + \frac{3}{4} - \frac{C}{2}\right). \quad (27)$$

Here, C is the Euler constant ($C \approx 0.5772$). Thus, we obtain the following expression for the density of the exchange-interaction energy as a function of the particle density in a 1D system:

$$\varepsilon_{exc} \approx -g_s\frac{e^2k_F^2}{2\pi^2}\int|\varphi(\boldsymbol{\rho}')|^2|\varphi(\boldsymbol{\rho}'')|^2\left[-\frac{1}{2}\ln(k_F|\boldsymbol{\rho}' - \boldsymbol{\rho}''|) + \frac{3}{4} - \frac{C}{2}\right]d\boldsymbol{\rho}'d\boldsymbol{\rho}'' \approx -\frac{\beta_{1D}}{g_s}n_{1D}^2 + \frac{\gamma_{1D}}{g_s}n_{1D}^2\ln\left(\frac{n_{1D}R}{\pi g_s}\right). \quad (28)$$

Here,

$$\beta_{1D} = e^2\left(\frac{3}{8} - \frac{C}{4}\right) \approx 0.28e^2,$$

$$\gamma_{1D} = \frac{e^2}{4}$$

and R is the width of the QWR. Note that, since this expression is obtained in the limiting case of low linear particle densities, when

$$k_F R \ll 1, \tag{29}$$

the logarithmic factor in the second term is negative and the corresponding exchange-energy correction is negative.

Let us now consider the other limiting case:

$$k_F R \approx \alpha \gg 1. \tag{30}$$

Then,

$$I(\alpha) = \int_{-\infty}^{+\infty} \frac{\sin^2(\alpha u)}{u^2\sqrt{1+u^2}} du \approx A\alpha,$$
$$A = \int_{-\infty}^{+\infty} \frac{\sin^2(t)}{t^2} dt \approx 3.1375, \tag{31}$$

and the linear density of the exchange energy

$$\varepsilon_{\text{exc}} = E_{\text{exc}}/\Omega_{1D} = -\frac{g_s e^2}{2\pi^2}\int \frac{|\varphi(\boldsymbol{\rho}')|^2|\varphi(\boldsymbol{\rho}'')|^2}{|\boldsymbol{\rho}' - \boldsymbol{\rho}''|^2} I(\alpha) d\boldsymbol{\rho}' d\boldsymbol{\rho}''$$
$$\approx \frac{Ae^2}{2\pi^2} k_F = \chi_{1D} n_{1D}, \tag{32}$$
$$\chi_{1D} \approx \frac{e^2}{2\pi}\int \frac{|\varphi(\boldsymbol{\rho}')|^2|\varphi(\boldsymbol{\rho}'')|^2}{|\boldsymbol{\rho}' - \boldsymbol{\rho}''|^2} d\boldsymbol{\rho}' d\boldsymbol{\rho}''$$

does not depend on the spin factor, similarly to the 2D case considered above (see (22)).

3. SPONTANEOUS SPIN POLARIZATION IN THE CASE OF EXCHANGE-INTERACTION ENERGY EXCEEDING THE KINETIC ENERGY

To answer the question of whether the exchange interaction may result in the appearance of a spontaneous spin polarization, we have to compare the total energies of polarized and unpolarized states of a quasi-2D or quasi-1D gas of charge carriers. In the limiting case of low charge-carrier densities, the energy density of a quasi-2D gas equals

$$\varepsilon^{2D} = \varepsilon_{kin} + \varepsilon_{\text{exc}} \approx \frac{\pi\hbar^2 n_{2D}^2}{m^* g_s} - \frac{\beta_{2D}}{g_s^{1/2}} n_{2D}^{3/2}, \tag{33}$$

where the first and the second terms correspond to the kinetic and the exchange-interaction energy, respectively. Thus, the energies of polarized ($g_s = 1$) and unpolarized ($g_s = 2$) states are equal to $\varepsilon^{2D}\big|_{g_s=1} \approx \pi\hbar^2 n_{2D}^2/m^* - \beta_{2D} n_{2D}^{3/2}$ and $\varepsilon^{2D}\big|_{g_s=2} \approx \pi\hbar^2 n_{2D}^2/2m^* - \beta_{2D} n_{2D}^{3/2}/\sqrt{2}$.

It is evident (see (33)) that, when the density of charge carriers exceeds the critical value n_0, which is equal to

$$n_0 = \left[\frac{(2-\sqrt{2})m^*\beta_{2D}}{\pi\hbar^2}\right]^2, \tag{34}$$

the kinetic energy exceeds the exchange-interaction energy and, thus, the unpolarized state is energetically more favorable than the polarized state.

At the same time, if the charge-carrier density does not exceed the critical value and the exchange energy is dominant, the polarized state is energetically more favorable. Note that n_0 depends only on the effective mass of the charge carriers and increases with increasing m^*. It should also be noted that the effective mass decreases as the density of charge carriers increases in a 2D system [7, 9]; it will be shown below that this phenomenon could be related to the growing dominance of the kinetic energy over the exchange-interaction energy.

In a 1D system, the energy density in the limiting case of low charge-carrier densities is given by the following expression (see (12) and (28)):

$$\varepsilon^{1D} = \frac{\pi^2\hbar^2 n_{1D}^3}{12 m g_s^2} - \frac{n_{1D}^2}{g_s}\left[\beta_{1D} - \gamma_{1D}\ln\left(\frac{n_{1D}R}{\pi g_s}\right)\right]. \tag{35}$$

Thus, the critical density n_0 is determined by the transcendental equation

$$\frac{3\pi^2\hbar^2 n_0}{24m} = \beta_{1D} - \gamma_{1D}\ln\left(\frac{2n_0 R}{\pi}\right), \tag{36}$$

which always has a unique solution.

For $n > n_0$, a complete spin depolarization of the quasi-1D gas occurs.

Two features of the discussed mechanism of the appearance of a spontaneous spin polarization in low-dimensional semiconductor systems should be noted. First, we considered quasi-2D and quasi-1D systems and, in this context, explicitly introduced the quantum-confinement wave functions. At the same time, we found that, in the limiting case of low n_{2D} and n_{1D}, the results are independent of these wave functions. Moreover, the conditions for the appearance of ferromagnetic ordering in a quasi-2D system in the limiting case of low densities of 2D charge carriers are actually reduced to those obtained for a strictly 2D system, in which case it was proven that inclusion of correlation corrections does not destroy the stability of the ferromagnetic state due to the exchange interaction [17–19].

Second, taking into account the correlation energy is very important in determining the 2D electron density corresponding to the onset of Wigner crystallization—a process that competes strongly with the above-considered transition to a spontaneously polarized state with extended wave functions [20–25]. However, according to theoretical estimates [22–25], a Wigner crystal is formed at densities below $n_{2D} \approx m^2e^4/r_s^2\hbar^2$, where r_s is the ratio of the potential to the kinetic energy, which corresponds to the transition to the crystalline state. Depending on the model chosen, the onset of Wigner crystallization is characterized by the value of r_s varying from 30 to 100 [22–25]. At the same time, the critical density corresponding to the complete depolarization of a spontaneously polarized 2D gas of charge carriers (see (34)) is $n_0 \approx 0.5m^2e^4/\hbar^2$. Thus, a spontaneous spin polarization in a 2D system arises when the kinetic and the potential energies are of the same order of magnitude; in contrast, Wigner crystallization occurs when their ratio is about 1 to 100. In other words, the transition to the crystalline state occurs at densities that are two to four orders of magnitude lower than those corresponding to the transition to a spontaneously polarized state with extended wave functions. A more accurate calculation [23–25] restricts the range of r_s corresponding to the appearance of a spontaneous spin polarization to $10 < r_s < 30$; for lower r_s, the probability of polarization decreases dramatically, apparently because of the rigorous requirements set by condition (20). Nevertheless, this restriction does not prohibit using the Hartree–Fock approximation to analyze ferromagnetic ordering induced by the exchange interaction, even if the correlation corrections are to be taken into account; it only limits the range of densities in which plane waves can be used for this purpose as zero-approximation wave functions.

A similar conclusion can be drawn from a consideration of the spontaneous spin polarization in quasi-1D systems with regard to the correlation energy [37, 42–45]. In this case, Wigner crystallization should take place for $r_s \geq 39$ [44], while a spontaneous spin polarization appears at $r_s = 3.3$ [37]. Since $r_s \approx (1/n_{2D})^{1/2}$, it should be expected that a spontaneous polarized state with extended wave functions is formed in a QWR at higher values of n_{2D} than in a 2D gas of charge carriers. Less stringent conditions for the appearance of a spontaneous spin polarization in a QWR in comparison to a 2D gas of charge carriers originate from an additional partial decay of the kinetic energy with a reduction in the system dimensionality [37].

We stress once more that this consideration corresponds to the limiting case of low charge-carrier densities: $k_Fd \ll 1$ for quasi-2D and $k_FR \ll 1$ for quasi-1D systems. This circumstance imposes serious restrictions on the width of QWs and QWRs. If these conditions are not satisfied, the system should be considered in the limiting case of high charge-carrier densities ($k_Fd \gg 1$ for quasi-2D and $k_FR \gg 1$ for quasi-1D systems), when an unpolarized state is always energetically more favorable than a polarized state, since the exchange energy becomes independent of g_s.

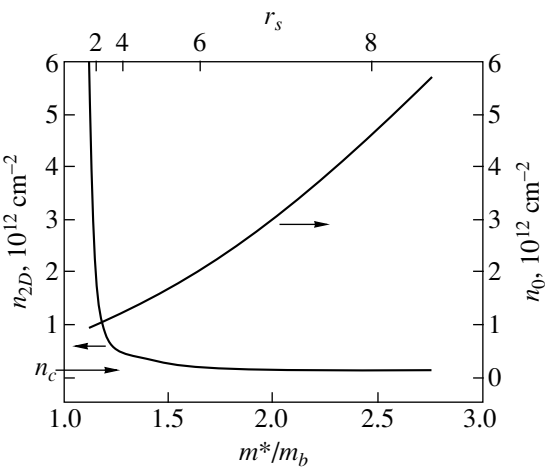

Fig. 1. Dependence of the critical density of electrons n_0 corresponding to a complete spin depolarization of a 2D electron gas in Si MOS structures on the effective mass m^*; the dependence of m^* on the electron density n_{2D}, as determined in [9], is also shown. Here, $m_b = 0.19m_0$ and n_c denotes the critical electron density for the onset of a metal–insulator transition in Si MOS structures [9].

4. SPIN DEPOLARIZATION AND METAL–INSULATOR TRANSITION IN 2D SYSTEMS

The values of the effective masses determined for 2D electrons and holes in Si MOS transistors [9] and GaAs/AlGaAs heterojunctions [7] with densities close to the critical density n_c, corresponding to the transition to a metallic state, were used to calculate the relevant dependences of n_0 on m^* (Figs. 1, 2). One can see that spontaneous spin polarization decreases sharply for densities of a 2D electron or hole gas above n_c. Note that the dependences shown in Figs. 1 and 2 demonstrate the importance of a spread in the values of n_c for the observations of a trend towards ferromagnetic ordering of a 2D electron gas in Si MOS transistors. Comparing the values of n_0 calculated for the case of $n_c = 8 \times 10^{10}$ cm^{-2}, where spontaneous polarization was observed [12, 15], with those calculated for the case of $n_c = 1.0 \times 10^{11}$ cm^{-2}, where no essential evidence of ferromagnetic ordering was revealed [9, 16], we find that they differ by two orders of magnitude. Possibly, it is this difference in the values of n_0 that leads to a sharp decrease in the degree of spin polarization of a 2D electron gas near the metal–insulator transition in a 2D system with higher n_c [9, 16] (although the residual effect of the polarized state can be seen in the deviation of the temperature dependences of the spin susceptibility from the Curie law [14], with a trend to superparamagnetism). However, such an explanation, based on the

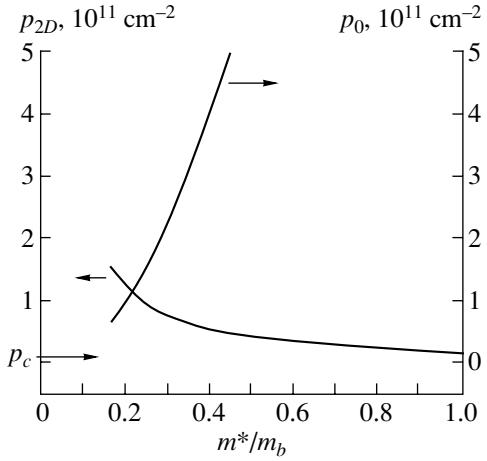

Fig. 2. Dependence of the critical density of holes p_0 corresponding to a complete spin depolarization of a 2D hole gas in Si MOS structures on the effective mass m^*; the dependence of m^* on the hole density p_{2D}, as determined in [7], is also shown. Here, $m_b = 0.38m_0$ and p_c denotes the critical hole density for the onset of a metal–insulator transition in GaAs/AlGaAs heterostructures [7].

coincidence of the critical values of the charge-carrier density corresponding to the metal–insulator transition n_c and to the appearance of a spontaneous spin polarization n_x [12, 15], contradicts the data on the Shubnikov–de Haas oscillations: the latter do not confirm the existence of a noticeable spin polarization of the charge carriers even at $n_{2D} \approx 7.5 \times 10^{10}$ cm^{-2} [9, 16]. It still remains unclear whether this result can be explained by a decrease in n_0 caused by greater disorder in the MOS structures studied in [9, 16] as compared to those studied in [12, 15]. Thus, the possible interrelationship between the critical densities n_c, n_x, and n_0 requires further research in order to identify the relative contributions of the spontaneous spin polarization [4, 12, 13] and the spin–orbit interaction [2, 9–11], as well as weak antilocalization and localization [46], to the mechanism of the metal–insulator transition in 2D systems.

5. SPIN DEPOLARIZATION AND QUENCHING OF THE $0.7(2e^2/h)$ FEATURE IN THE QUANTUM STAIRCASE CONDUCTANCE OF A ONE-DIMENSIONAL CHANNEL

The critical linear density n_0 corresponding to a complete spin depolarization in a QWR connecting two 2D reservoirs, which is given by (36), depends upon the wire width and the effective mass. With a decrease in the 2D charge-carrier density n_{2D}, the effective mass increases [7, 9] (see Figs. 1, 2). Energy dependence of the effective mass may be one reason for such behavior; in particular, this dependence was calculated for GaAs-based QWs in the case when the kinetic energy and the quantum-confinement energy are dominant [47, 48]:

$$m = m_0(1 + 1.447E + 0.245E^2). \quad (37)$$

Here, E is the sum of the kinetic and quantum-confinement energies in a QW and the coefficients of E account for the band parameters of GaAs.

It was found that the electron effective mass increases by a factor of 1.1–2 due to the increase in the quantum-confinement energy as the QW width decreases below 10 nm [47–49]. Even if the exchange-energy contribution, compensating the kinetic energy (see (33)), is taken into account in (37), this does not lead to a corresponding decrease in the effective mass with increasing n_{2D} in 2D systems (such as the GaAs-based QWs analyzed in this study). However, the exchange interaction may significantly affect the effective mass of charge carriers in QWRs, because a spontaneously polarized state with extended wave functions in a quasi-1D system is formed at higher values of n_{2D} than in a 2D gas of charge carriers [37]. Consequently, in the middle part of a QWR connecting two 2D reservoirs, the kinetic energy is effectively quenched due to a competition with the exchange energy (see (35)), which may favor a reduction in the effective mass with increasing n_{2D}. Thus, the calculated dependences of the electron effective mass in GaAs wires, shown in Fig. 3a, demonstrate the increasing role of the exchange interaction as the widths of the QW and QWR (d and R, respectively) decrease, which makes it easier to satisfy conditions (20) and (29). It should be noted that the enhanced role of the exchange interaction in systems of lower dimensionality may account for the considerable increase in the effective mass of electrons as their density decreases in QWs [9] (see Fig. 1): in this case, the formation of 2D relatively large areas connected by quantum point contacts is rather probable, especially in the presence of disorder [50].

The data shown in Fig. 3a enable one to determine the values of the critical linear density n_0 (36), corresponding to a complete spin depolarization of electrons in a QWR connecting two 2D GaAs reservoirs (Fig. 3b). These dependences of n_0 on the charge-carrier density in 2D reservoirs n_{2D} can be used in analysis of the density dependences of the $0.7(2e^2/h)$ feature in the quantum staircase conductance of a 1D channel formed in a QW using the split-gate technique [30].

Ballistic 1D channels of this kind are quantum point contacts or short QWRs formed upon application of a negative voltage to a pair of split gates, which are formed in a 2D structure by electron-beam lithography [30–32]. As the gate voltage U_g increases, the density of electrons in the QWR connecting two 2D reservoirs also increases, which leads to an increase in the number of occupied 1D subbands. The dependence $G(U_g)$ in this case is a set of plateaus separated by steps of height $2e^2/h$: a stepwise change in the conductance of a 1D channel occurs each time the Fermi level coincides with one of the 1D subbands, so that

$$G = G_0NT. \quad (38)$$

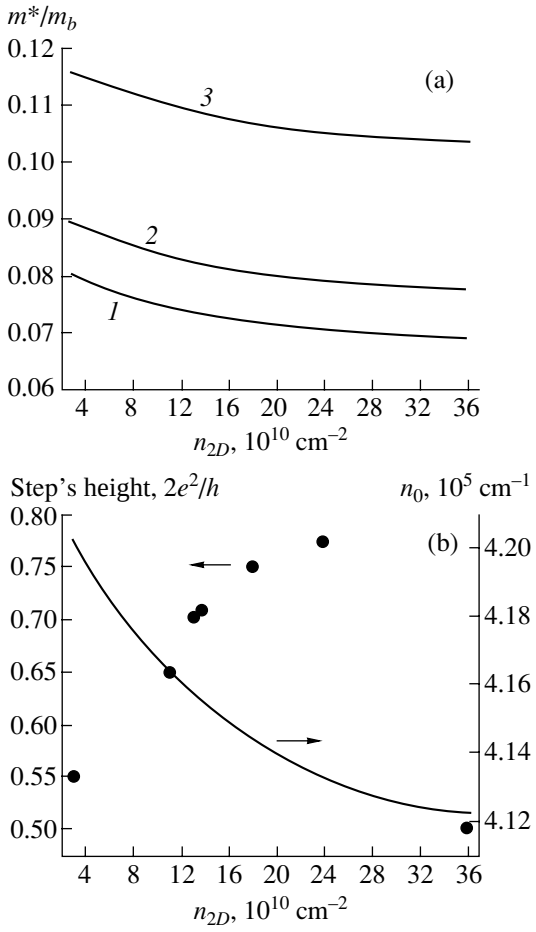

Fig. 3. (a) Dependence of the effective mass in a 1D channel connecting 2D reservoirs in a GaAs/AlGaAs QW on the density of electrons in them. The dependence is plotted according to (37), taking into account the contributions from the quantum-confinement energy, the kinetic energy, and the exchange-interaction energy. The width of the QWR R = 100 nm; the width of the QW d = (*1*) 20, (*2*) 10, and (*3*) 5 nm. (b) Dependence of the critical linear density corresponding to a complete spin depolarization of the quasi-1D electron gas in a QWR connecting 2D reservoirs in a GaAs/AlGaAs QW on the density of electrons in them; R = 100 nm, d = 20 nm. Circles indicate the height of the substep in the staircase function of the quantum conductance ($0.7(2e^2/h)$ feature) determined experimentally for 1D channels formed in GaAs/AlGaAs QWs using the split-gate technique [26–29].

Here, $G_0 = 2e^2/h$; N is the number of occupied 1D subbands, which can be changed by varying U_g and corresponds to the number of the highest occupied subband; and T is the transmission coefficient, which equals unity if the elastic-scattering length exceeds the length of the ballistic channel. Thus, the quantum staircase structure in the conductance dependence $G(U_g)$ indicates the adiabatic transparency of spin-nondegenerate 1D subbands. With the level of nanotechnology attained in recent years, the split-gate technique makes it possible to form QWRs that have one or several 1D ballistic channels in GaAs/AlGaAs heterostructures

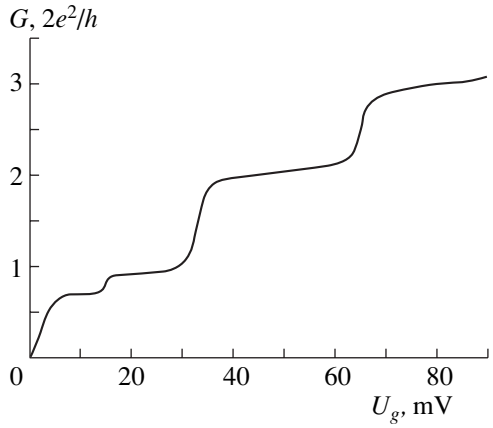

Fig. 4. Current–voltage characteristic for the case of staircase quantum conductance of a 1D channel oriented along the [001] direction, formed in a self-ordered p-type Si(100) QW in the plane. The position of the Fermi level corresponds to the occupation of the 1D subbands of heavy holes; T = 77 K (see also [51, 52]).

[26–32] and Si QWs [51–53]; they are identified by the observation of a quantum staircase in the electron [26–32] or hole [51–53] conductance (see Fig. 4).

Studies of the quantum staircase conductance under conditions of low occupation of the lowest 1D subbands are of a special interest; in this case, as shown above, the exchange interaction is dominant, which may favor spontaneous spin polarization of quasi-1D charge carriers [26–29, 34–37, 40, 51–53]. A consequence of the spontaneous polarization of a 1D gas of charge carriers in zero magnetic field is the appearance of a $0.7(2e^2/h)$ feature that splits off from the first step in the staircase function of quantum conductance, its height approaching $0.5(2e^2/h)$ with increasing external magnetic field oriented along the QWR [26].

Evidently, an important factor that supports the interpretation of the $0.7(2e^2/h)$ feature as a criterion for the appearance of a spontaneous polarization in a 1D channel is its dependence on the particle density, which is plotted in Fig. 3b using the data from [26–29]. One can see that, at sufficiently small values of n_{2D}, when the 1D channel is completely polarized, the height of the $0.7(2e^2/h)$ feature almost attains the value of $0.5(2e^2/h)$, which indicates that spin degeneracy of the first step of the quantum-conductance staircase is lifted. However, as soon as the charge-carrier density in the 2D reservoir attains the value corresponding to the critical linear density in the 1D channel (n_0), the height of the $0.7(2e^2/h)$ feature evolves towards its normal value due to partial spin depolarization. It should be noted that an apparent level-off of the height of the substep near $0.75(2e^2/h)$ is probably related to its temperature dependence, which suggests that such a behavior should occur at finite temperatures because of partial spin depolarization of the electron gas near the bottom of the 1D subband [40]. A most interesting result is the

unexpected transformation of the $0.7(2e^2/h)$ feature with a subsequent increase in n_{2D}, with its height approaching $0.5(2e^2/h)$ (see Fig. 3b). The observed increase in the spin polarization of electrons in the QWR probably originates from the magnetic ordering of electrons occupying the lowest 1D subband due to the indirect exchange via electrons excited to the upper subband at a finite temperature. Indirect-exchange mechanisms, which are responsible for such nonequilibrium spin polarization in a 1D channel, are most probably related to the processes of spin-correlated transport within a narrow band [54, 55] and spin polarization under the conditions of the formation of spin polarons [44]. It should be noted that the $0.5(2e^2/h)$ substep at large values of n_{2D} is much more readily observed in QWRs with a higher level of disorder [56]; this is another indication of the important role that indirect exchange plays in lifting the spin degeneracy of the first step in the staircase function of quantum conductance observed under these conditions.

6. CONCLUSIONS

Analysis of the conditions for the appearance of a spontaneous spin polarization in low-dimensional systems in zero magnetic field, carried out within the Hartree–Fock approximation, enabled us to determine the critical densities above which a complete spin depolarization of a quasi-2D and a quasi-1D gas of charge carriers occurs.

We established the density range, governed by the correlation corrections, in which plane waves can be used as zero-order wave functions in the analysis of ferromagnetic ordering in low-dimensional systems in the case of dominance of the exchange energy over the kinetic energy. We demonstrated that the transition of a 2D gas to the crystalline state begins at charge-carrier densities that are two to four orders of magnitude lower than those corresponding to the transition to a spontaneously polarized state with extended wave functions. A similar conclusion can be drawn from the analysis of the conditions for spontaneous spin polarization in quasi-1D systems with regard to the correlation energy. We demonstrated that a spontaneously polarized state with extended wave functions in a QWR appears at larger values of the 2D density of charge carriers than in a QW, which is caused by the effective quenching of the kinetic energy due to competition with the exchange energy upon a reduction of the dimensionality of the system.

Such a quenching of the kinetic energy in the middle part of a QWR connecting two 2D reservoirs may contribute to a decrease in the effective mass in a quasi-1D gas of charge carriers as their 2D density increases. Furthermore, enhancement of the exchange interaction with decreasing dimensionality of the system presumably accounts for the increase in the effective mass of electrons as their density decreases in a QW [9], which is accompanied by the appearance of superparamagnetism, since in this case (especially in the presence of disorder) there is a high probability that 2D relatively large areas connected by quantum point contacts will appear.

A correlation was found between the critical densities corresponding to the spin depolarization and the metal–insulator transition in a 2D gas of charge carriers. However, the issue of the possible interrelationship between these critical densities and the critical density corresponding to the formation of a spontaneously polarized state of a 2D gas requires further research. One should bear in mind that the spin–orbit interaction, which may also cause the metal–insulator transition, affects the processes of spin depolarization.

The dependences of the critical linear density corresponding to a complete spin depolarization in a QWR connecting two 2D reservoirs on the density of 2D charge carriers were used in the analysis of the density dependence of the $0.7(2e^2/h)$ feature in the staircase function of the quantum conductance of a 1D channel formed in a QW by the split-gate technique.

It was demonstrated that at a sufficiently low charge-carrier density n_{2D} in 2D reservoirs, so that the 1D channel is completely polarized at a density lower than this value, the $0.7(2e^2/h)$ feature almost attains the value of $0.5(2e^2/h)$, which indicates that the spin degeneracy of the first step in the staircase function of the quantum conductance is lifted. However, with an increase in n_{2D}, the linear density in the 1D channel attains the critical value corresponding to a complete spin polarization, due to which the $0.7(2e^2/h)$ feature evolves back to its normal magnitude. The observed level-off of the height of this quantum substep near $0.75(2e^2/h)$ is probably related to its temperature dependence, which suggests that such a behavior should occur at finite temperatures, since, owing to the large widths of QWRs available for experiments, partial spin depolarization of the electron gas near the bottom of the 1D subband occurs even at ultralow temperatures.

ACKNOWLEDGMENTS

We are grateful to V.F. Sapega and V.V. Shnitov for useful discussions of the results of this study and for help in carrying out numerical calculations.

This study was supported by the International Science and Technology Center, grant no. 2136.

REFERENCES

1. S. V. Kravchenko, G. V. Kravchenko, J. E. Furneaux, *et al.*, Phys. Rev. B **50**, 8039 (1994).
2. V. M. Pudalov, Usp. Fiz. Nauk **168**, 227 (1998) [Phys. Usp. **41**, 211 (1998)].
3. A. M. Finkel'shtein, Zh. Éksp. Teor. Fiz. **84**, 168 (1983) [Sov. Phys. JETP **57**, 97 (1983)].
4. G. Zala, B. N. Narozhny, and I. L. Aleiner, Phys. Rev. B **64**, 201201 (2001).

5. E. A. Abrahams, P. W. Anderson, D. C. Licciardello, and T. V. Ramakrishnan, Phys. Rev. Lett. **42**, 673 (1979).
6. P. T. Coleridge, R. L. Williams, Y. Feng, and P. Zawadzkii, Phys. Rev. B **56**, R12764 (1997).
7. Y. Y. Proskuryakov, A. K. Savchenko, S. S. Safonov, *et al.*, Phys. Rev. Lett. **89**, 076406 (2002).
8. Y. Hanein, D. Shahar, C. C. Li, *et al.*, Phys. Rev. B **58**, R13338 (1998).
9. V. M. Pudalov, M. E. Gershenson, H. Kojima, *et al.*, Phys. Rev. Lett. **88**, 196404 (2002).
10. L. E. Golub and S. Pedersen, cond-mat/0205373 (2002).
11. E. I. Rashba, J. Supercond. **15**, 1 (2002).
12. A. A. Shashkin, S. V. Kravchenko, V. T. Dolgopolov, and T. M. Klapwijk, Phys. Rev. Lett. **87**, 086801 (2001).
13. S. A. Vitkalov, H. Zheng, K. M. Mertes, *et al.*, Phys. Rev. Lett. **87**, 086401 (2001).
14. O. Prus, Y. Yaish, M. Reznikov, *et al.*, cond-mat/0209142 (2002).
15. S. V. Kravchenko, A. A. Shashkin, and V. T. Dolgopolov, Phys. Rev. Lett. **89**, 219701 (2002).
16. V. M. Pudalov, M. E. Gershenson, H. Kojima, *et al.*, Phys. Rev. Lett. **89**, 219702 (2002).
17. F. Stern, Phys. Rev. Lett. **30**, 278 (1973).
18. A. K. Rajagopal and J. C. Kimball, Phys. Rev. B **15**, 2819 (1977).
19. N. Iwamoto, Phys. Rev. B **43**, 2174 (1991).
20. R. S. Crandall and R. W. Williams, Phys. Lett. A **34A**, 404 (1971).
21. P. M. Platzman and H. Fukuyama, Phys. Rev. B **10**, 3150 (1974).
22. H. Fukuyama, P. M. Platzman, and P. W. Anderson, Phys. Rev. B **19**, 5211 (1979).
23. G. Senatore, S. Moroni, and D. Varsano, Solid State Commun. **119**, 333 (2001).
24. B. Bernu, L. Candido, and D. M. Ceperley, Phys. Rev. Lett. **86**, 870 (2001).
25. C. Attaccalite, S. Moroni, P. Gori-Giorgi, and G. B. Bachelet, Phys. Rev. Lett. **88**, 256601 (2002).
26. K. J. Thomas, J. T. Nicholls, M. Y. Simmons, *et al.*, Phys. Rev. Lett. **77**, 135 (1996).
27. K. J. Thomas, J. T. Nicholls, N. J. Appleyard, *et al.*, Phys. Rev. B **58**, 4846 (1998).
28. K. J. Thomas, J. T. Nicholls, M. Pepper, *et al.*, Phys. Rev. B **61**, 13365 (2000).
29. K. S. Pyshkin, C. J. B. Ford, R. H. Harrell, *et al.*, Phys. Rev. B **62**, 15842 (2000).
30. T. J. Thornton, M. Pepper, H. Ahmed, *et al.*, Phys. Rev. Lett. **56**, 1198 (1986).
31. D. A. Wharam, T. J. Thornton, R. Newbury, *et al.*, J. Phys. C **21**, L209 (1988).
32. B. J. van Wees, H. van Houten, C. W. J. Beenakker, *et al.*, Phys. Rev. Lett. **60**, 848 (1988).
33. A. Yakoby, H. L. Stormer, N. S. Wingreen, *et al.*, Phys. Rev. Lett. **77**, 4612 (1996).
34. Chuan-Kui Wang and K.-F. Berggren, Phys. Rev. B **54**, 14257 (1996).
35. Chuan-Kui Wang and K.-F. Berggren, Phys. Rev. B **57**, 4552 (1998).
36. A. M. Bychkov, I. I. Yakymenko, and K.-F. Berggren, in *Proceedings of 8th International Symposium on Nanostructures: Physics and Technology* (St. Petersburg, 2000), p. 391.
37. Kenji Hirosi, Shu-Shen Li, and N. S. Wingreen, Phys. Rev. B **63**, 033315 (2001).
38. A. Gold and L. Calmels, Philos. Mag. Lett. **74**, 33 (1996).
39. A. Gold and L. Calmels, in *Proceedings of the 23rd International Conference on Physics of Semiconductors, Berlin, 1996*, Ed. by M. Scheffler and R. Zimmermann (World Sci., Singapore, 1996), p. 1229.
40. I. A. Shelykh, N. T. Bagraev, V. K. Ivanov, and L. E. Klyachkin, Fiz. Tekh. Poluprovodn. (St. Petersburg) **36**, 70 (2002) [Semiconductors **36**, 65 (2002)].
41. E. Lieb and D. Mattis, Phys. Rev. **125**, 164 (1962).
42. V. V'yurkov and V. Vetrov, in *Proceedings of 8th International Symposium on Nanostructures: Physics and Technology* (St. Petersburg, 2000), p. 444.
43. V. V'yurkov and V. Vetrov, Nanotechnology **11**, 336 (2000).
44. B. Spivak and Fei Zhou, Phys. Rev. B **61**, 16730 (2000).
45. H. Bruus, V. Cheianov, and K. Flensberg, cond-mat/0002338 (2000).
46. I. V. Gornyĭ, A. P. Dmitriev, and V. Yu. Kocharovskiĭ, Pis'ma Zh. Éksp. Teor. Fiz. **68**, 314 (1998) [JETP Lett. **68**, 338 (1998)].
47. M. Altarelli, U. Ekenberg, and A. Fasolino, Phys. Rev. B **32**, 5138 (1985).
48. U. Ekenberg, Phys. Rev. B **40**, 7714 (1989).
49. G. Goldoni, T. Ruf, V. F. Sapega, *et al.*, Phys. Rev. B **51**, 14542 (1995).
50. B. A. Aronzon, D. A. Bakaushin, A. S. Vedeneev, *et al.*, Fiz. Tekh. Poluprovodn. (St. Petersburg) **31**, 1460 (1997) [Semiconductors **31**, 1261 (1997)].
51. N. T. Bagraev, A. D. Buravlev, L. E. Klyachkin, *et al.*, Fiz. Tekh. Poluprovodn. (St. Petersburg) **36**, 462 (2002) [Semiconductors **36**, 439 (2002)].
52. N. T. Bagraev, A. D. Bouravleuv, W. Gehlhoff, *et al.*, Physica E (Amsterdam) **12**, 762 (2002).
53. N. T. Bagraev, A. D. Bouravleuv, W. Gehlhoff, *et al.*, Physica E (Amsterdam) **13**, 764 (2002).
54. N. T. Bagraev, A. I. Gusarov, and V. A. Mashkov, Zh. Éksp. Teor. Fiz. **92**, 968 (1987) [Sov. Phys. JETP **65**, 548 (1987)].
55. N. T. Bagraev, A. I. Gusarov, and V. A. Mashkov, Zh. Éksp. Teor. Fiz. **95**, 1412 (1989) [Sov. Phys. JETP **68**, 816 (1989)].
56. D. J. Reilly, G. R. Facer, A. S. Dzurak, *et al.*, cond-mat/0001174 (2000).

Translated by M. Skorikov

Semiconductors, Vol. 37, No. 12, 2003, pp. 1400–1405. Translated from Fizika i Tekhnika Poluprovodnikov, Vol. 37, No. 12, 2003, pp. 1449–1455.

LOW-DIMENSIONAL SYSTEMS

Fabrication and Optical Properties of Photonic Crystals Based on Opal–GaP and Opal–GaPN Composites

G. M. Gadzhiev*, V. G. Golubev, M. V. Zamoryanskaya**, D. A. Kurdyukov**, A. V. Medvedev**, J. Merz***, A. Mintairov***, A. B. Pevtsov**, A. V. Sel'kin**, V. V. Travnikov**^, and N. V. Sharenkova****

**Institute of Physics, Dagestan Scientific Center, Russian Academy of Sciences, Makhachkala, 367003 Russia*

***Ioffe Physicotechnical Institute, Russian Academy of Sciences, St. Petersburg, 194021 Russia*

^e-mail: travn@spectr.mail.ru

****University of Notre Dame, Notre Dame, 46556 IN, USA*

Submitted May 22, 2003; accepted for publication May 22, 2003

Abstract—Nanocrystalline GaP and amorphous GaPN solid solution have been synthesized in voids of artificial opal. The opal–GaP and opal–GaPN composites obtained clearly demonstrate properties of photonic crystals. The reflection spectra of the opal–GaPN composite exhibit specific features related to multiple Bragg diffraction on two systems of {111} planes, parallel and nonparallel to the surface of the photonic crystal. The study of photoluminescence spectra revealed a considerable modification of the emission band of the opal–GaPN composite, which was attributed to the influence of the photonic band gap. *© 2003 MAIK "Nauka/Interperiodica".*

1. INTRODUCTION

Photonic crystals are 3D-periodic structures whose dielectric constant is modulated with a period comparable with the wavelength of light. The interaction of photons with these structures results in considerable modification of the spatial distribution and energy spectrum of the electromagnetic field. In particular, there arise photonic band gaps (PBG), i.e., ranges of energy for which the propagation of light is impossible in certain (pseudo-PBG) or all (complete PBG) directions within the photonic crystal [1]. The energy gap and the space angle corresponding to PBGs are defined by the depth of modulation of the dielectric constant and, therefore, depend on the optical contrast $\eta = \max(\varepsilon_a/\varepsilon_b, \varepsilon_b/\varepsilon_a)$, where ε_a and ε_b are the dielectric constants of materials forming the photonic crystal.

Complete PBG is only possible in 3D photonic crystals with high enough η (in photonic crystals with a face-centered cubic lattice, η must be $\gtrsim 8.5$ [2]). PBGs are formed through Bragg diffraction of electromagnetic waves on the system of crystal planes in the photonic crystal lattice. A necessary condition for the formation of PBG is that a large enough number of the lattice planes participate in the diffraction process. Therefore, it is desirable to synthesize photonic crystals from materials with a weak absorption of light in the spectral range corresponding to PBG. Thus, to produce structures with clearly pronounced photonic crystal properties, it is necessary to use component materials which have real parts of the dielectric constant that differ considerably and imaginary parts that are as low as possible.

Considerable promise for the synthesis of photonic crystals for the visible light range is offered by semiconductor compounds GaP [3], GaN [4], and their solid solutions. These semiconductors are transparent in the visible range, and they are characterized by a high dielectric constant. Moreover, specific luminescent properties of these compounds are widely used in modern semiconductor optoelectronics [5, 6]. In this context, photonic crystals based on GaP, GaN, and GaPN may also be promising for the study of the effect of PBG on the spontaneous emission characteristics. The point is that it is the possibility of controlling the probability of spontaneous emission from a source embedded in a photonic crystal that determines the prospects of practically applying photonic crystals as components of LEDs and low-threshold-pumping lasers [7]. The above considerations have stimulated our efforts to synthesize and study photonic crystals based on GaPN solid solutions.

2. SAMPLES

As we reported earlier [8], the starting matrices for the fabrication of our photonic crystals were synthetic opals composed of a 3D-ordered close-packed lattice of *a*-SiO_2 spheres. In these opals, up to 26% of the total volume is occupied by air voids between the spheres, and this volume is accessible to fill with other materials. The diameter of the spheres, determined with scanning electron and atomic-force microscopes, was ~245 nm. The opals had a polydomain structure. The characteristic size of domains with a high degree of

ordering of SiO_2 spheres was about 100 μm. Each submicrometer SiO_2 sphere was composed of nanosize particles of amorphous SiO_2, with some fraction of air voids in between. As a result of this, the average dielectric constant of a sphere, ε_b, differs from the value for bulk *a*-SiO_2. According to our estimates [9], $\varepsilon_b \approx 2.0$ for the opal samples used.

Semiconductors were synthesized directly in the opal voids using a technology similar to that used in [10]. At the initial stage, the voids between the spheres were filled with a Ga_2O_3 precursor. Later, opals were annealed at a temperature of about 900°C in a mixture of nitrogen and phosphorus hydrides. The chemical reactions that may take place in these conditions should yield GaPN material in the opal voids, and, therefore, hereafter we shall refer to the samples obtained in this case as opal–GaPN composites. By analogy, we shall denote the samples obtained by annealing in an atmosphere of phosphorus hydrides only as opal–GaP composites. The degree to which the voids were filled with the material was determined by gravimetry to be 20–30%.

The atomic concentrations of elements forming the materials introduced into the opals were determined by X-ray electron probe microanalysis. In the opal–GaP composite, the concentrations of Ga and P atoms were nearly equal (Ga : P ≈ 1 : 1.2). Some excess of P can be accounted for by the presence of elementary phosphorus in the opal voids, which could condense during cooling of the sample in phosphorus vapor. Analysis of the intensity of characteristic X-ray lines has shown that the concentration ratio of the principal components in opal–GaPN composites is Ga : P : N = 1 : 0.2 : 0.8. It is worth noting that the concentration of nitrogen atoms is determined with a low precision due to the low intensity of characteristic lines of light atoms (in our case, N and O).

The X-ray study has shown that the material introduced into the voids of the opal–GaP composite is cubic nanocrystalline GaP (Fig. 1a), and the material synthesized in the voids of the opal–GaPN composite is X-ray-amorphous (Fig. 1b). At high nitrogen content (~0.8), which occurs in our case, the crystallization of solid solution can be thermodynamically unfavorable due to the considerable lattice mismatch and the difference in crystal structure type between GaN (hexagonal) and GaP (cubic). The maximum value of *x* at which crystalline $GaP_{1-x}N_x$ solid solution could be obtained did not exceed 0.16 [11]. Two limiting alternatives are possible for the X-ray-amorphous material formed in the opal pores: (i) an amorphous GaPN solid solution and (ii) a material consisting of two separate amorphous phases, GaP and GaN. It is possible, in principle, that the substance formed is a mixture of these limiting cases.

In order to identify the nature of the materials formed in the opal voids, the Raman scattering spectra were studied. The data for the opal–GaP composite have confirmed that GaP introduced in voids has a nanocrystalline structure. We did not manage to measure Raman spectra for the opal–GaPN composite, because it appeared that all the emission lines of Ar-ion and Kr-ion lasers that were at our disposal gave rise to strong photoluminescence (see below), which made it impossible to resolve the weak spectral features associated with Raman scattering.

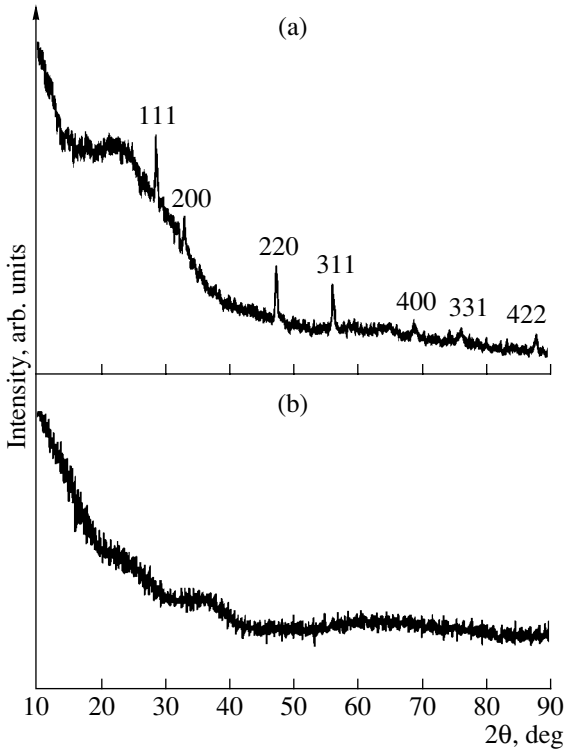

Fig. 1. X-ray diffraction patterns of (a) opal–GaP and (b) opal–GaPN composites.

The formation of separate amorphous phases in the opal voids hardly seems likely. Indeed, crystalline hexagonal GaN is formed at the same temperature of synthesis during annealing of Ga_2O_3 in a nitrogen hydride vapor [4], and crystalline cubic GaP is formed during annealing in a phosphorus hydride vapor (Fig. 1a). If the GaP and GaN phases were separated when a vapor mixture of nitrogen and phosphorus oxides is used, it might be expected that these separated phases would also be crystalline, since the synthesis conditions would be similar. The lack of any evidences of crystallinity in the diffraction pattern in Fig. 1b leads us to conclude that in this case an amorphous GaPN solid solution is formed in the opal voids. Taking into account the difference between the free energies of dissociation of nitrogen and phosphorus hydrides (ΔG_d^0 = 16.21 and −13.4 kJ/mol, respectively) [12], the X-ray-amorphous GaP_xN_{1-x} solid solution formed may be characterized by an inhomogeneous concentration distribution over the sample.

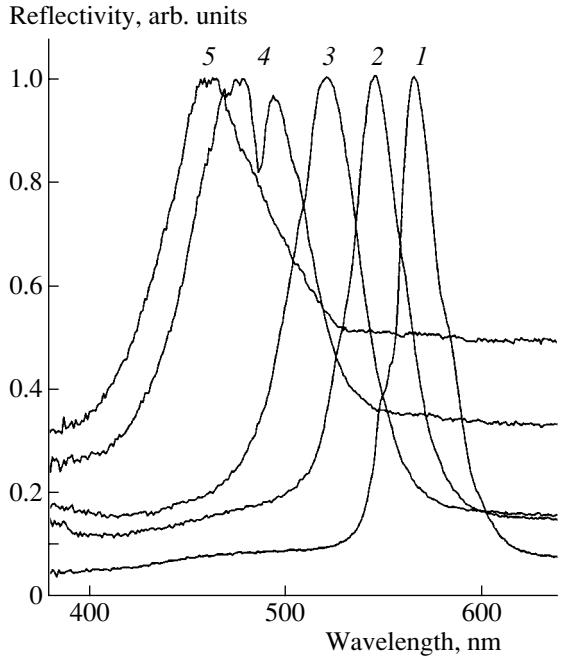

Fig. 2. The Bragg reflection spectra of the opal–GaPN composite at different angles of incidence of light: (*1*) 12°, (*2*) 30°, (*3*) 40°, (*4*) 57°, and (*5*) 65°.

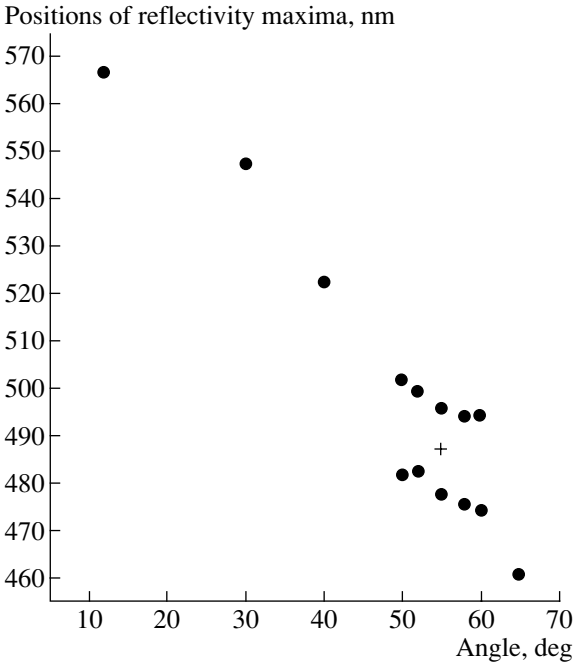

Fig. 3. Angular dependence of the positions of the Bragg reflection peaks. The cross lies in the middle of the line segment connecting the maximum in the lower branch with the minimum in the upper branch.

3. OPTICAL STUDIES: RESULTS AND DISCUSSION

In order to study the photonic crystal properties of the composites produced, we analyzed the specular light reflection and photoluminescence (PL) spectra.

3.1. Reflection Spectra

Figure 2 shows the reflection spectra of the opal–GaPN composite at various angles of incidence of light, recorded in *s*-polarization (a detailed report on the study of the light reflection spectra of the opal–GaP composite will be published elsewhere). The spectra demonstrate pronounced peaks, which are blue-shifted as the angle of incidence θ increases. The formation of these peaks and the specific shift in their angular dependence, which approximately obeys the well-known Bragg Law, are a direct result of the existence of PBG in photonic crystals.

As the angle of incidence increases, at $\theta \approx 50°$, an additional peak at a shorter wavelength appears in the reflection spectrum. The peak intensity increases and becomes comparable with the intensity of the long-wavelength peak at $\theta \approx 55°$. The spectra develop a clearly pronounced doublet structure. As the angle of incidence further increases, the intensity of the long-wavelength peak decreases, and only the short-wavelength peak remains.

The presence of this doublet structure in the reflection spectrum under oblique incidence of light is indicative of multiple Bragg diffraction [13], i.e., the simultaneous diffraction of light on a system of at least two intersecting crystal planes. One system of planes is the family of (111) growth planes parallel to the natural surface of the sample. The other system of nodal planes should cross the (111) planes at some angle.

In [13], the appearance of the doublet structure under oblique incidence of light was attributed to simultaneous diffraction on the (111) and (200) planes. However, a contribution to multiple diffraction must also be made by planes of the {111} family that are not parallel to the sample surface (hereafter, we denote these planes as $(11\bar{1})$). In this case, a considerably stronger effect of multiple diffraction should be expected precisely on the intersecting (111) and $(11\bar{1})$ planes, rather than on the (111) and (200) planes, because the spatial modulation of the dielectric constant in $\langle 200 \rangle$ directions is much weaker than the corresponding modulation in $\langle 111 \rangle$ directions. This fact is confirmed by numerical estimations and direct experimental observations [14]. Consequently, PBGs formed by {200} planes are much narrower than those arising from the Bragg diffraction on {111} planes.

The dependences of the Bragg reflection peaks on the angle of incidence, which are shown in Fig. 3, demonstrate two branches (lower and upper) separated by

an avoiding-crossing area [13]. The cross in the figure marks the point in the center of the line segment connecting the minimum of the upper branch with the maximum of the lower one. Our analysis has shown that, in the case of a weak periodic perturbation of the dielectric constant, the Bragg conditions are met in this point ($\lambda = \lambda_*$, $\theta = \theta_*$) simultaneously for the diffraction on three planes, (111), $(11\bar{1})$, and (200), of the face-centered cubic lattice. In the case of a face-centered cubic lattice, the coordinates of point (λ_*, θ_*) obey the following simple relations:

$$\frac{a}{\lambda_*}\sin\theta_* = \sqrt{3}/4, \quad (1)$$

$$\varepsilon_0 = 2\sin^2\theta_*, \quad (2)$$

where a is the distance between the centers of spheres in the opaline structure and ε_0 is the average dielectric constant of the structure.

The relations (1), (2) can be used for further characterization of photonic crystals. The substitution of the measured values $a = 245$ nm, $\lambda_* = 487.5$ nm, and $\theta_* \approx 55°$ in Eq. (1) shows that relation (1) is satisfied with good accuracy: $(a/\lambda_*)\sin\theta_* \approx 0.42$ and $\sqrt{3}/4 \approx 0.43$. This indicates that the structure of the sample under study corresponds to a face-centered cubic lattice.[1] If this is the case, relation (2) must also be satisfied, and the value $\varepsilon_0 = 2.0$ is obtained for wavelength λ_*. At the same time, ε_0 satisfies the relation

$$\varepsilon_0 = \varepsilon_a(1 - f) + \varepsilon_b f, \quad (3)$$

where ε_a and ε_b are, respectively, the average dielectric constants of the inter-sphere space and the spheres themselves, and f is the factor describing the filling of the structure with spheres. Then, using the known values ε_b and f [9] and the estimate for ε_0, we find $\varepsilon_a \approx 2.0$. The value ε_a obtained is the average dielectric constant for the space between spheres, which is partially filled with air and GaPN. Assuming as a rough approximation that ε_a is a linear function of the degree to which voids are filled with solid solution and taking into account the inaccuracy of gravimetric data, we estimate the dielectric constant of the synthesized amorphous GaPN as $\varepsilon_{GaPN} = 4.5$–6.0 in the spectral range of the avoiding-crossing area. This estimate, as well as the results of electron-probe microanalysis, indicate a high density of nitrogen in synthesized GaPN, since the dielectric constant ε_{GaN} of pure GaN is ~5.5 (at around 500 nm) [15].

[1] In several pure opals and synthesized composites, a considerable (over 10%) deviation from Eq. (1) was obtained upon the substitution of the measured (λ_*, θ_*) values in the left-hand side of Eq. (1), which indicated that the spatial symmetry of these photonic crystals differed from that of the face-centered cubic lattice.

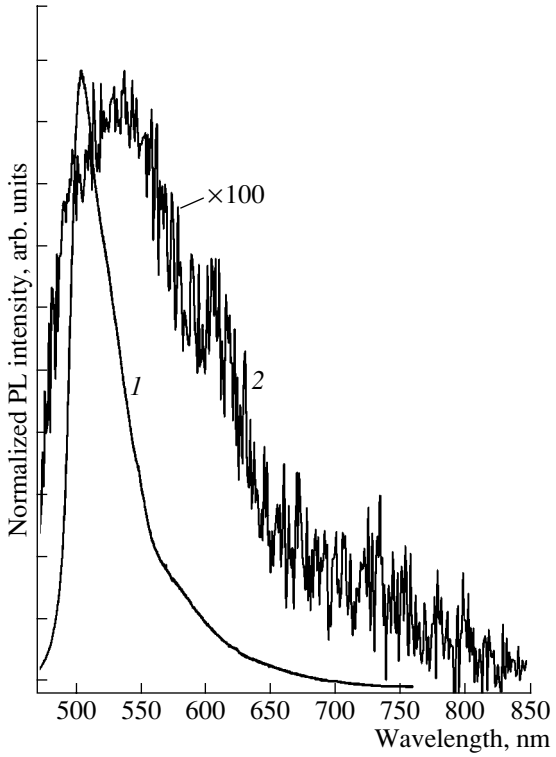

Fig. 4. PL spectra from disordered areas (characterized by a zero Bragg component in the reflection spectra) of (*1*) opal–GaPN and (*2*) opal–GaP composites.

3.2. Photoluminescence

The photoluminescence (PL) of the composites produced was studied at room temperature. The PL was excited with an Ar-ion laser at 457.9 nm. The measurements were taken on different areas of the sample surface: from well-ordered areas within selected domains characterized by strong Bragg reflection of light and from disordered areas with a zero Bragg reflection component. An optical microscope was used to select different areas on the sample surface. The laser beam was focused on the sample surface at normal angle of incidence with a microscope lens (×10) to within a single domain. The same objective collected the PL radiation, which was projected onto the spectrometer slit with a system of lenses and semitransparent mirrors. The detector was a Jobin Yvon CCD camera.

Figure 4 shows PL spectra from disordered areas of the composites. The opal–GaPN composites are characterized by a strong PL band (spectrum *1*) with a peak intensity more than two orders of magnitude higher than the intensity of the corresponding band in the opal–GaP composite (spectrum *2*). As shown in Fig. 4, in spite of the fact that the positions of PL peaks of both composites lie in the same spectral range, their shapes differ noticeably. The PL band from the opal–GaP composite is considerably broader than that from the opal–

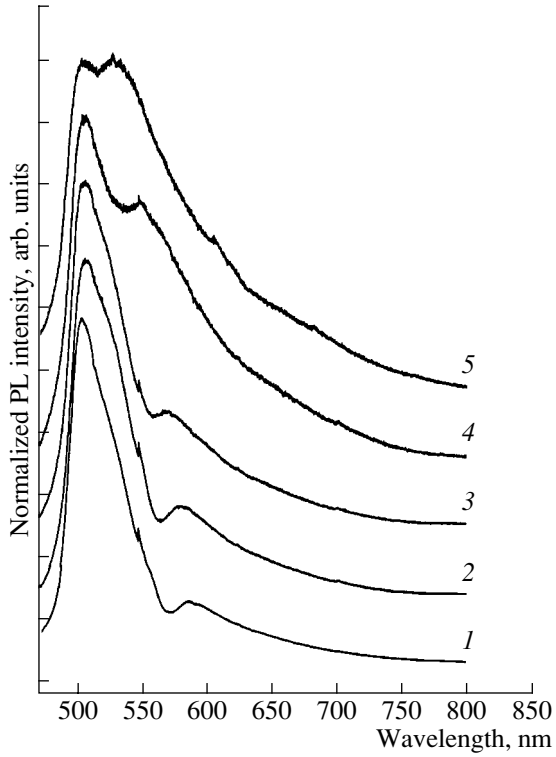

Fig. 5. PL spectra from well-ordered (within a single domain) areas of the opal–GaPN composite at different angles of emission exit relative to the normal to the sample surface: (*1*) 0°, (*2*) 14°, (*3*) 26°, (*4*) 45°, and (*5*) 51°. For convenience, the spectra are shifted along the ordinate. The surge in spectra at about 550 nm is due to the switching of the recording ranges.

GaPN and is shifted to longer wavelengths with respect to the latter.

The PL peaks of the opal–GaP composite are shifted substantially to shorter wavelengths with respect to the Bragg reflection peaks, which lie in the 680 nm range. In the opal–GaPN composite, the PL bands observed lie in the spectral range of PBG. This factor, combined with a high PL intensity, made it possible to observe manifestations of PBG in the luminescence spectra. Figure 5 shows the PL spectra from an ordered area of the opal–GaPN composite with different emission exit angles relative to the normal to the surface. The spectra demonstrate a dip, the position and shift of which correlate with the position and shift of the reflection spectra peaks as the exit angle increases. The dip in the PL spectra is caused by the fact that the intensity of radiation exiting at a definite angle relative to the (111) surface should strongly decrease in the spectral range satisfying the Bragg reflection conditions (due to the influence of PBG on the conditions of photon propagation).

In the case of opals filled with a semiconductor, the contribution to PL can be made by electron–hole radiative recombination within a semiconductor, as well as by emission from the opal matrix (e.g., that related to the oxygen vacancy in SiO_2) [3, 16, 17]. According to [18], PL spectra of amorphous SiO_2 at $T = 300$ K demonstrate two emission bands in the spectral range under study: a distinct, relatively narrow (with an FWHM of 0.19 eV) band at ~645 nm (1.92 eV) and a weaker and broader (FWHM 0.35 eV) band at ~516 nm (2.40 eV). In the spectra of bare opals and opals filled with ZnS, the peaks of broad PL bands related to SiO_2 emission correspond to an energy of 2.3 eV (~539 nm) [17]. The position of a broad (FWHM 0.5 eV) PL band in the opal–GaP composite can also be estimated as 2.30 eV (Fig. 4). Therefore, it may be assumed that the PL band observed in the opal–GaP composite is largely related to the emission from the opal matrix itself.

The PL band of the opal–GaPN composite (Fig. 4) differs considerably in shape, FWHM (0.2 eV), and position (505 nm, 2.45 eV) from the PL bands related to emission from the opal matrix [3, 16, 17]. We suppose that this band originates mainly from the PL of the X-ray-amorphous material synthesized in the opal voids. Taking into account the ambiguity of our conclusions about the nature of this material, we will discuss possible alternative origins of the band in question. If separate amorphous phases (see above) appeared in the opal voids, the band could be attributed to radiative recombination in GaP or GaN. At room temperature, the PL peak of crystalline GaP (2.3 eV [6]) is shifted to longer wavelengths with respect to the peak of the band under discussion. According to published data [6], the addition of a minor amount of nitrogen shifts the PL band of GaP to the long-wavelength (red) side of the spectrum. Taking this into account, we believe that the observed PL band cannot be related to emission from the amorphous phase of GaP (usually, the luminescence bands in amorphous materials are shifted to longer wavelengths relative to their positions in crystalline analogues). As was found in [19], a broad luminescence band of amorphous GaN lies at about 2.8 eV, and, therefore, it is considerably shifted to the short-wavelength side with respect to the PL band in the opal–GaPN composite. In the light of the above, one may only assume that the principal contribution to the luminescence observed in the sample under study comes from radiative recombination of nonequilibrium carriers in the amorphous phase of the semiconductor GaPN.

The results of calculation of the energy gap in $GaP_{1-x}N_x$ solid solution as a function of x were presented in [20]. For the estimated nitrogen content in our samples ($x = 0.8$), the absorption edge of the solid solution corresponds to direct transitions (Γ–Γ transition in the crystalline phase), and it should lie at about 2.6 eV [20]. This position of the energy gap edge correlates with the observed position of the PL emission peak (2.45 eV, Fig. 4) in the opal–GaPN composite. Further research is needed to definitively determine the nature of the PL bands observed.

4. CONCLUSION

The possibility of forming 3D photonic crystals based on the semiconductor composites opal–GaP and opal–GaPN has been demonstrated. The studies of optical spectra have shown that the structures obtained exhibit clearly pronounced properties of photonic crystals and can be regarded as promising objects for fundamental research and technical applications.

The Bragg reflection spectra of the opal–GaPN composite contain distinct features related to multiple diffraction of light on the systems of nonparallel crystallographic planes of the {111} family. It is shown that the spectral positions of these features and their dependence on the angle of incidence of light are directly related to the optical and geometrical parameters of the composite.

The PL spectra of opal–GaP and opal–GaPN composites have been studied. Owing to the fact that the energy position of PBG in the opal–GaPN composite falls within the broad emission band of the semiconductor material, it was possible to observe an appreciable modification of the emission spectrum related to the effect of the PBG. Thus, it was shown that a synthesized opal–GaPN structure can be used, in principle, for controlling the characteristics of spontaneous emission and can be regarded as a promising system in the design of low-threshold lasers.

ACKNOWLEDGMENTS

This study was supported by the Russian Foundation for Basic Research; the program "Low-Dimensional Quantum Structures" of the Presidium of the Russian Academy of Sciences; the program "Physics of Solid-State Nanostructures" of the Ministry of Industry, Science, and Technology of the Russian Federation; and a grant from NATO (PST. CLG. 978079).

REFERENCES

1. *Photonic Crystals and Light Localization in the 21st Century*, Ed. by C. M. Soukoulis (Kluwer, Dordrecht, 2001).
2. K. Bush and S. John, Phys. Rev. E **58**, 3896 (1998).
3. S. G. Romanov, R. M. De La Rue, H. M. Yates, and M. E. Pemble, J. Phys.: Condens. Matter **12**, 339 (2000).
4. Yu. Davydov, V. G. Golubev, N. F. Kartenko, *et al.*, Nanotechnology **11**, 291 (2000).
5. S. Nakamura and G. Fasol, *The Blue Laser Diode: GaN Based Light Emitters and Lasers* (Springer, Berlin, 1997).
6. C. W. Tu, J. Phys.: Condens. Matter **13**, 7169 (2001).
7. E. Yablonovitch, Phys. Rev. Lett. **58**, 2059 (1987).
8. V. G. Golubev, V. A. Kosobukin, D. A. Kurdyukov, *et al.*, Fiz. Tekh. Poluprovodn. (St. Petersburg) **35**, 710 (2001) [Semiconductors **35**, 680 (2001)]; V. G. Golubev, V. Yu. Davydov, N. F. Kartenko, *et al.*, Appl. Phys. Lett. **79**, 2127 (2001); G. Gajiev, V. G. Golubev, D. A. Kurdyukov, *et al.*, Phys. Status Solidi B **231**, R7 (2002).
9. V. G. Golubev, A. V. Il'inskii, D. A. Kurdyukov, *et al.*, in *Abstracts of 10th International Symposium on Nanostructures: Physics and Technologies* (St. Petersburg, 2002), p. 108.
10. G. Gadzhiev, V. G. Golubev, V. Yu. Davydov, *et al.*, in *Proceedings of III International Conference on Amorphous and Microcrystal Semiconductors* (St. Petersburg, 2002), p. 9; A. B. Pevtsov, V. G. Golubev, D. A. Kurdyukov, *et al.*, in *Abstracts of MRS Fall Meeting* (Boston, USA, 2002), p. 361; G. Gajiev, V. G. Golobev, D. A. Kurdyukov, *et al.*, in *Abstracts of 10th International Symposium on Nanostructures: Physics and Technologies* (St. Petersburg, 2002), p. 134.
11. W. G. Bi and C. W. Tu, Appl. Phys. Lett. **69**, 3710 (1996).
12. V. A. Rabinovich and Z. Ya. Khavin, *Brief Chemical Handbook* (Khimiya, Leningrad, 1977).
13. H. M. van Driel and W. L. Vos, Phys. Rev. B **62**, 9872 (2000).
14. A. Reynolds, F. Lopez-Tejeira, D. Cassagne, *et al.*, Phys. Rev. B **60**, 11422 (1999).
15. G. Yu, G. Wang, H. Ishikawa, *et al.*, Appl. Phys. Lett. **70**, 3209 (1997).
16. R. C. Schroden, M. Al-Daous, and A. Stein, Chem. Mater. **13**, 2945 (2001).
17. S. G. Romanov, A. V. Fokin, and R. M. De La Rue, Appl. Phys. Lett. **74**, 1821 (1999).
18. M. A. Stevens Kalceff, Phys. Rev. B **57**, 5674 (1998).
19. A. A. Andreev, Fiz. Tverd. Tela (St. Petersburg) **45**, 395 (2003) [Phys. Solid State **45**, 419 (2003)].
20. S. Miyoshi and K. Onabe, Jpn. J. Appl. Phys., Part 1 **37**, 4680 (1998).

Translated by D. Mashovets

Semiconductors, Vol. 37, No. 12, 2003, pp. 1406–1410. Translated from Fizika i Tekhnika Poluprovodnikov, Vol. 37, No. 12, 2003, pp. 1456–1460.

LOW-DIMENSIONAL SYSTEMS

Room-Temperature 1.5–1.6 μm Photoluminescence from InGaAs/GaAs Heterostructures Grown at Low Substrate Temperature

A. A. Tonkikh[1, 2]*, G. E. Tsyrlin[1, 2], V. G. Talalaev[3, 2], B. V. Novikov[3], V. A. Egorov[1, 2], N. K. Polyakov[1, 2], Yu. B. Samsonenko[1, 2], V. M. Ustinov[1], N. D. Zakharov[4], and P. Werner[4]

[1]*Ioffe Physicotechnical Institute, Russian Academy of Sciences, St. Petersburg, 194021 Russia*

[2]*Institute for Analytical Instrumentation, Russian Academy of Sciences, St. Petersburg, 198063 Russia*

[3]*St. Petersburg State University, St. Petersburg, 198504 Russia*

[4]*Max Planck Institute of Microstructure Physics, Halle Weinberg 2, D-06120 Halle, Germany*

**e-mail: alex234@newmail.ru*

Submitted May 23, 2003; accepted for publication June 2, 2003

Abstract—Heterostructures with In(Ga)As/GaAs quantum dots and quantum wells grown at low substrate temperature were studied by reflection high-energy electron diffraction, transmission electron microscopy, and photoluminescence methods. It is shown that InAs deposited onto (100) GaAs surface at low substrate temperature forms 2D clusters composed of separate quantum dots. Optical spectra of structures containing such clusters demonstrate emission in the 1.5–1.6 μm range. © *2003 MAIK "Nauka/Interperiodica"*.

1. INTRODUCTION

The development of laser diodes for the 1.55-μm wavelength for global optical fiber communication lines is a topical problem in modern optoelectronics [1]. In fact, only one approach has been devised up to now: the use of laser diodes with an active region based on semiconductor heterostructures with InGaAsP/InP quantum wells (QW). However, this system suffers from two fundamental drawbacks: (i) poor temperature behavior of laser diodes because of the weak confinement of electrons in the active region; (ii) low parameters of Bragg reflectors, caused by the small difference between the refractive indices of InGaAsP and InP and the low thermal conductivity of InGaAsP [2]. These shortcomings have stimulated research on the design of 1.55-μm laser diodes based on other systems. Research in several areas of this field is currently in progress; for example, growth of InAs quantum dots (QD) on InP substrates [3], growth of QWs in the GaAsSbN/GaAs system [4], and doping of a semiconductor material (e.g., GaN) with erbium [5]. We believe that the approaches based on GaAs substrates are highly promising, because they offer higher temperature stability of laser structures and the possibility of fabricating Al(Ga)As/GaAs Bragg reflectors in a single cycle of epitaxy. However, studies of Ga(In)As/GaAs and Ga(In)As(N)/GaAs systems were until recently based on the design of laser diodes for a wavelength of ~1.3 μm, with the active region based on arrays of InAs/GaAs QDs [6] or InGaAsN QWs [7]. Lately, studies of the emission from heterostructures of this kind near 1.55 μm have appeared. A high-intensity photoluminescence (PL) near 1.55 μm from InGaAsN/GaAs QW heterostructures was observed in [8]. In the same InGaAsN/GaAs system, PL at 1.3 and 1.55 μm was obtained from QD heterostructures [9]. The addition of Sb into the active region of a GaInNAs/GaAs QW laser [10] made it possible to fabricate a stripe laser emitting at a wavelength of 1.5 μm at room temperature, with a threshold current density of 3.5 kA/cm^2 and an output emission power of 22 mW. The possibility of obtaining long-wavelength (~1.7 μm) emission from structures with laterally associated InAs/GaAs quantum dots (LAQD) fabricated at low substrate temperature (~320–350°C) was demonstrated in [11]. The first observation of 1.55–1.6 μm electroluminescence at temperatures of up to 260 K from LAQD structures was reported in [12]. In the present study, we used the last method modified in several ways: (i) InAs was deposited onto a GaAs substrate at low temperature and a low growth rate; (ii) the effect of misorientation of the substrate surface in low-temperature InAs/GaAs deposition was studied; (iii) the low-temperature deposition of $In_{0.5}Ga_{0.5}As$ solid solution in metal-stabilized conditions was used.

2. EXPERIMENT

Growth experiments were performed in an EP1203 MBE setup using semiinsulating (100) GaAs substrates. The samples under study consisted of a GaAs buffer layer, a low-temperature active region, and two short-period GaAs/AlGaAs superlattices (SL) impeding the nonradiative recombination of carriers at the

interface with the substrate and in the surface region. Except in the case of the low-temperature active region, the sample growth temperature was 580°C. The samples under study differed in their methods of active region formation. In comparison with previous studies [11–13], we introduced several radical innovations, which can be conventionally divided into three types. First, InAs was deposited onto a GaAs substrate at low substrate temperature (350–410°C) and a slow growth rate (~0.03 Å/s); second, $In_{0.5}Ga_{0.5}As$ solid solution was deposited at low substrate temperature; third, InAs was grown on the vicinal surface of the substrate at a low rate, at temperatures below 300°C. The effective thickness of the InAs layer was three monolayers (ML) in all the samples, except those with InGaAs solid solution. The thickness of the InGaAs solid solution layer in the samples of the second type varied from 2 to 5 nm.

The As_4 flux was kept constant as the structure was grown, so that the In/As flux ratio was ~1/100 at an InAs growth rate of 0.03 Å/s, and the Ga/As flux ratio during the growth of GaAs was ~1/2. In the case of low-temperature layers in samples of the second type, InGaAs solid solution was grown in metal-stabilized conditions (without a direct flow of As_4 toward the substrate). The deposition of an In-containing layer was followed by the growth of a 5-nm-thick low-temperature GaAs layer to prevent the evaporation of InAs during the subsequent rise of temperature and growth of the high-temperature portion of the structure. For the third type of samples, vicinal (100) GaAs substrates were used, with the surface misoriented by 7° in the [011] direction. The substrate temperature was found by extrapolating the pyrometer data and the readings of the thermocouple of the sample heater. The deposition of In(Ga)As was monitored by means of reflection high-energy electron diffraction (RHEED).

PL was excited by an Ar-ion laser (488 nm, 2 W/cm^2) and detected by a cooled Ge photodetector (Edinburgh Instruments) at the monochromator output. A JEM 4010 microscope was used for transmission electron microscopy (TEM).

3. RESULTS AND DISCUSSION

Figure 1 shows a cross-sectional TEM image of a sample of the first type with an InAs layer of 3 ML effective thickness, covered with a 5-nm-thick GaAs layer at the same substrate temperature of 350°C. Analysis of the image shows that InAs is concentrated in nanoislands. The lateral size of the islands can be estimated as ~7 nm; their height, ~3 nm. One should note that the estimations of the typical size of InAs QDs obtained at deposition temperatures of 450–500°C are 12–14 nm (lateral size) and 4–6 nm (height) [14, 15]. Thus, in our case the characteristic size of InAs islands is smaller. A reduction in the size of InAs/GaAs islands with decreasing substrate temperature (in the range 420–500°C) was also observed in [16]. This fact is confirmed by comparing the PL spectra (Fig. 2) of samples

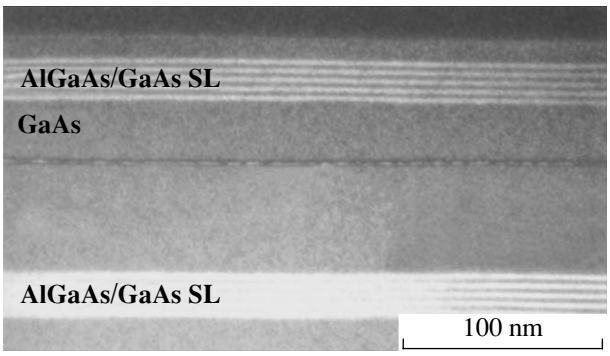

Fig. 1. Cross-sectional TEM image of the sample with 3 ML InAs deposited at a substrate temperature of 350°C.

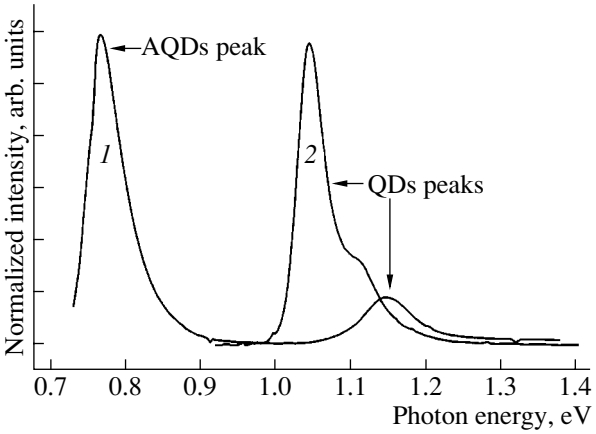

Fig. 2. PL spectra of structures with 3 ML InAs grown at substrate temperatures of (*1*) 350°C and (*2*) 480°C; recorded at a temperature of 300 K.

grown at low (spectrum *1*) and high (spectrum *2*) substrate temperatures. Spectrum *1* in Fig. 2 exhibits two specific features. The short-wavelength peak (1.15 eV) corresponds to the radiative recombination of carriers from the ground levels in isolated QDs. A comparison of the position of this peak with the peak energy of spectrum *2* for the sample with 3 ML of InAs deposited at a substrate temperature of 480°C led us to the conclusion that the exciton level in low-temperature QDs is 100 meV higher than in high-temperature ones. This indicates that the QDs are smaller in size, which is also confirmed by the TEM data (Fig. 1). The second specific feature of spectrum *1* is a new band at a wavelength of 1.6 μm (~0.78 eV). In [11], a similar PL band was attributed to the presence of LAQDs. The TEM image in Fig. 1 confirms the presence of LAQDs in our sample. As can be seen, InAs islands form conglomerates, which is not typical of InAs QD arrays grown at high substrate temperature [16]. However, based on this cross-sectional TEM image (Fig. 1), it is impossible to conclude whether InAs islands form chains or whether they are distributed in the form of 2D clusters over the

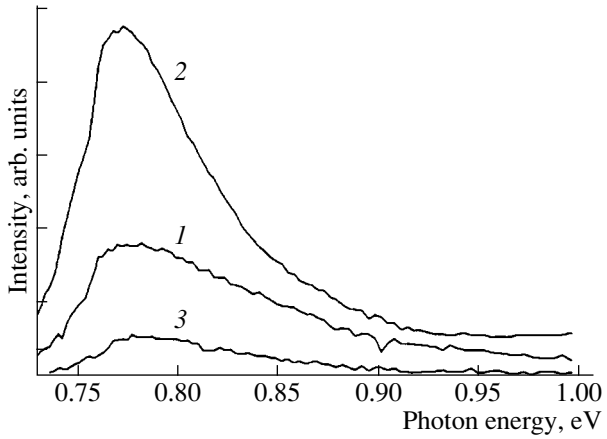

Fig. 3. PL spectra of structures with $In_{0.5}Ga_{0.5}As$ solid solution deposited onto a GaAs substrate at 350°C; recorded at 77 K. The thickness of $In_{0.5}Ga_{0.5}As$ layer: (*1*) 2, (*2*) 3, and (*3*) 5 nm.

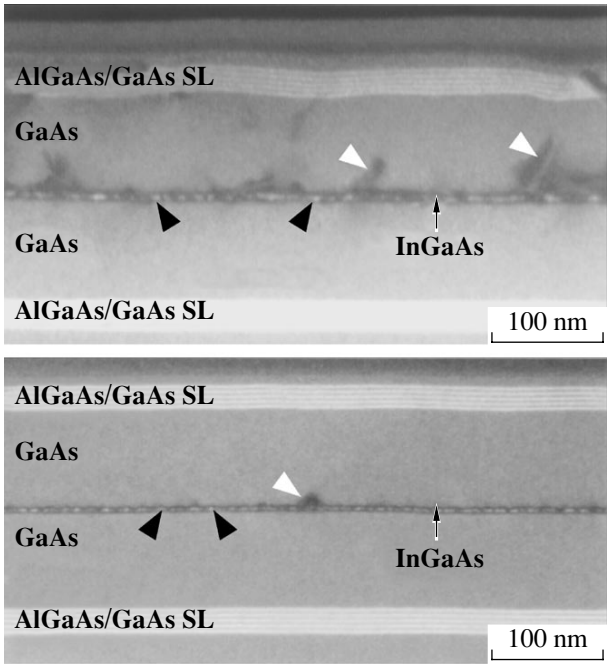

Fig. 4. Cross-sectional TEM images of the sample with a 5-nm-thick $In_{0.5}Ga_{0.5}As$ layer deposited onto GaAs at 350°C. Layer thickness: (top) 5 nm, (bottom) 3 nm.

GaAs surface. This problem will be discussed below on the basis of planar TEM images.

The second type of structure under study was represented by the samples with an active region formed by depositing a 50% InGaAs solid solution at low substrate temperature. RHEED and PL studies have proved that the properties of InGaAs/GaAs structures grown at low (~350°C) substrate temperature strongly depend on the ratio between the fluxes of Group III elements (Ga + In) and As_4. Preliminary experiments have shown that, with an excess of molecular As ((In + Ga)/As_4 flux ratio ~ 1/40), InGaAs islands are formed on the surface of the sample after the deposition of 23 Å of $In_{0.5}Ga_{0.5}As$ solid solution, which is indicated by the characteristic modification of the RHEED pattern. With a twofold reduction of the As_4 flux ((In + Ga)/As_4 ratio ~ 1/20), InGaAs islands were formed after the deposition of 34 Å of InGaAs solid solution. At the same time, in depositing In + Ga with the As_4 flow shut off (in this case, the background pressure in the growth chamber was $\sim 1 \times 10^{-6}$ Pa), no InGaAs islands were formed until the thickness of the growing films reached ~100 Å. In addition, it was noticed that, even during subsequent low-temperature growth of GaAs, the excess As flux results in the formation of InGaAs islands at the overgrowth stage. In attempts to deposit a $In_{0.5}Ga_{0.5}As$ layer with a thickness exceeding the above-mentioned critical thickness for the transition to island growth, mismatch dislocations were formed, and the optical properties of structures deteriorated. Thus, we have established that the growth of InGaAs solid solution at low substrate temperatures occurs in the planar mode only in metal-stabilized conditions, without a direct flow of arsenic toward the substrate surface. The most typical optical and structural properties of this type of sample are shown in Figs. 3 and 4.

Figure 3 shows PL spectra of structures of the second type, which, like structures of the first type, demonstrate a long-wavelength peak at about 1.6 μm. However, in contrast to structures of the first type, in this case it was possible to resolve the long-wavelength peaks only at low temperatures (77 K). Analysis of Fig. 4 allowed us to understand the source of the deterioration of optical properties for this type of sample at higher measurement temperatures. This figure shows cross-sectional TEM images of structures with 5- and 3-nm-thick $In_{0.5}Ga_{0.5}As$. White arrows indicate the mismatch dislocations, which partly relieve elastic stress in the structure. It is noteworthy that the density of the mismatch dislocations is considerably smaller in the sample with 3 nm of InGaAs. This fact is due to the lower total amount of InAs incorporated into the structure as compared to the sample with 5 nm of InGaAs. A comparison of data in Figs. 3 and 4 led to the conclusion that the PL intensity in samples of the second type is determined primarily by the density of the mismatch dislocations. Along with the observed mismatch dislocations, another specific feature of these images is the fact that the InGaAs layer is not solid but consists of a set of fine objects (marked with black arrows). These objects (islands) are enriched in InAs; their lateral size is ~7 nm. Thus, it follows from Fig. 4 that, even in epitaxy under 2D-growth conditions (no transition from 2D- to 3D-growth was observed in RHEED patterns), closely spaced InAs islands are formed in the structures under study, which is typical of samples of the first type, in which InAs islands were formed in the course of deposition.

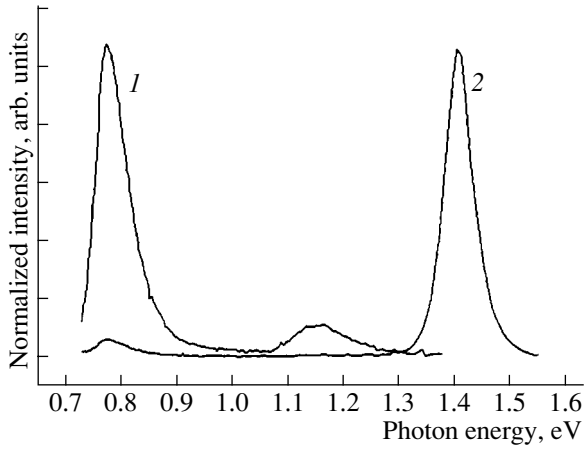

Fig. 5. PL spectra of structures with 3 ML InAs grown at 250°C on GaAs substrates: (*1*) misorientation of GaAs substrate by 7° in the [011] direction; (*2*) singular GaAs surface; recorded at 300 K.

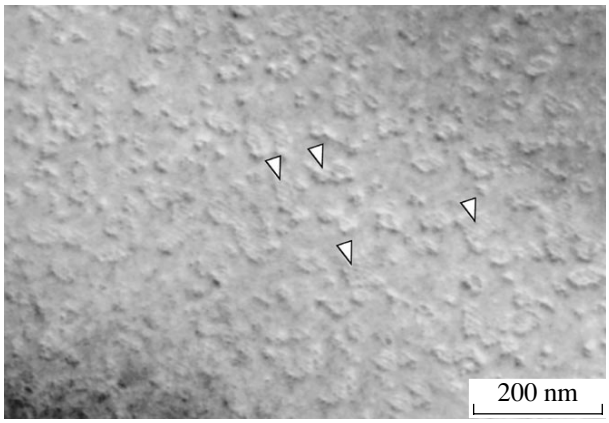

Fig. 6. Planar TEM image of the sample with 3 ML InAs deposited at 250°C onto a vicinal GaAs surface misoriented by 7° in the [011] direction.

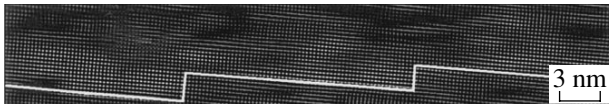

Fig. 7. High-resolution cross-sectional TEM image of the vicinal sample. Light areas: enriched with In; dark areas: GaAs matrix.

As suggested in [11], InAs/GaAs LAQDs are not formed during the deposition of InAs onto a GaAs substrate at substrate temperatures below 300°C owing to the low rate of surface migration of In atoms on the GaAs surface. We performed an experiment with InAs deposition onto a GaAs substrate at 250°C; two samples with the same amount of InAs were grown, which differed in the misorientation of their GaAs surfaces (the third type of sample). The effective thickness of InAs (3 ML) and other growth parameters, except for the surface temperature, were the same as for samples of the first type. PL studies (Fig. 5) have shown that, in the case of a singular GaAs surface, the PL peak of isolated QDs does disappear completely (spectrum *2*), and the intensity of the LAQD peak decreases. In contrast, the PL spectrum of a vicinal sample (spectrum *1*) contains an intense line in the 1.6-μm range, as well as a peak at 1.1 μm associated with isolated islands. A planar TEM image of the surface of a vicinal sample is shown in Fig. 6. It can be seen that clusters composed of InAs islands are formed on the surface of GaAs. The characteristic lateral size of InAs islands in clusters is 7.2 nm, whereas the cluster size varies over a wide range. Analysis of the high-resolution cross-sectional TEM image of the vicinal sample (Fig. 7) led us to the conclusion that the height of the InAs islands is 3.3 nm. It can be seen in Fig. 6 that, as a rule, InAs clusters include three to five rows of InAs islands, and the number of islands in a row, as well as the cluster size, vary over a wide range. The rows of InAs QDs are oriented in a direction normal to the surface misorientation, i.e., in the $[01\bar{1}]$ direction. This TEM image indicates the presence of laterally associated InAs QDs, which are responsible for the additional long-wavelength peak in the PL spectra.

4. CONCLUSION

It has been shown that the 1.6-μm band in PL spectra of In(Ga)As/GaAs can be obtained using several different methods. The structures of highest perfection are produced by depositing pure InAs onto a GaAs surface; however, the deposition of InGaAs solid solution under optimized growth conditions provides a similar result. It is shown also that conglomerates of InAs islands (laterally associated quantum dots) were formed in the structures under study. The emission peak at 1.6 μm dominates in the PL spectra of optimized structures at room temperature. The existence of steps on the vicinal surface of GaAs stimulates the formation of QD conglomerates at substrate temperatures below 300°C.

ACKNOWLEDGMENTS

This study was supported in part by the Ministry of Industry, Science, and Technology of the Russian Federation.

G.E.T. acknowledges the support of the Alexander von Humboldt Foundation.

REFERENCES

1. N. M. Margalit, Sh. Z. Zhang, and J. E. Bowers, IEEE Top. Lightwave **5**, 164 (1997).
2. N. A. Maleev, A. E. Zhukov, A. R. Kovsh, *et al.*, Fiz. Tekh. Poluprovodn. (St. Petersburg) **33**, 629 (1999) [Semiconductors **33**, 586 (1999)].
3. Y. F. Li, X. L. Ye, B. Xu, *et al.*, J. Cryst. Growth **218**, 451 (2000).

4. J. C. Harmand, G. Ungaro, J. Ramos, *et al.*, J. Cryst. Growth **227–228**, 553 (2001).
5. H. Shen, J. Pamulapati, M. Taysing, *et al.*, Solid-State Electron. **43**, 1231 (1999).
6. S. S. Mikhrin, A. E. Zhukov, A. R. Kovsh, *et al.*, Fiz. Tekh. Poluprovodn. (St. Petersburg) **36**, 1400 (2002) [Semiconductors **36**, 1315 (2002)].
7. V. A. Odnoblyudov, A. Yu. Egorov, A. R. Kovsh, *et al.*, Pis'ma Zh. Tekh. Fiz. **29** (10), 77 (2003) [Tech. Phys. Lett. **29**, 433 (2003)].
8. V. A. Odnoblyudov, A. Yu. Egorov, N. V. Kryzhanovskaya, *et al.*, Pis'ma Zh. Tekh. Fiz. **28** (22), 82 (2002) [Tech. Phys. Lett. **28**, 964 (2002)].
9. M. Sopanen, H. P. Xin, and C. W. Tu, Appl. Phys. Lett. **76**, 994 (2000).
10. L. H. Li, V. Sallet, G. Patriarche, *et al.*, in *Proceedings of International Workshop on GaAs Based Lasers for 1.3–1.5 μm Wavelength Range* (2003), p. 49.
11. M. V. Maximov, A. F. Tsatsul'nikov, B. V. Volovik, *et al.*, Appl. Phys. Lett. **75**, 2347 (1999).
12. A. E. Zhukov, B. V. Volovik, S. S. Mikhrin, *et al.*, Pis'ma Zh. Tekh. Fiz. **27** (17), 51 (2001) [Tech. Phys. Lett. **27**, 734 (2001)].
13. A. A. Tonkikh, V. A. Egorov, N. K. Polyakov, *et al.*, Pis'ma Zh. Tekh. Fiz. **28** (10), 72 (2002) [Tech. Phys. Lett. **28**, 434 (2002)].
14. M. Grundmann, J. Christen, N. N. Ledentsov, *et al.*, Phys. Rev. Lett. **74**, 4043 (1995).
15. I. Hapke-Wurst, U. Zeitler, H. W. Schumacher, *et al.*, Semicond. Sci. Technol. **14**, L41 (1999).
16. N. A. Cherkashin, M. V. Maksimov, A. G. Makarov, *et al.*, Fiz. Tekh. Poluprovodn. (St. Petersburg) **37** (7), 120 (2003) [Semiconductors **37**, 861 (2003)].

Translated by D. Mashovets

Semiconductors, Vol. 37, No. 12, 2003, pp. 1411–1413. Translated from Fizika i Tekhnika Poluprovodnikov, Vol. 37, No. 12, 2003, pp. 1461–1464.

LOW-DIMENSIONAL SYSTEMS

Lasing at 1.5 μm in Quantum Dot Structures on GaAs Substrates

A. E. Zhukov*, A. P. Vasil'yev, A. R. Kovsh, S. S. Mikhrin, E. S. Semenova, A. Yu. Egorov, V. A. Odnoblyudov, N. A. Maleev, E. V. Nikitina, N. V. Kryjanovskaya, A. G. Gladyshev, Yu. M. Shernyakov, M. V. Maximov, N. N. Ledentsov, V. M. Ustinov, and Zh. I. Alferov

Ioffe Physicotechnical Institute, Russian Academy of Sciences, St. Petersburg, 194021 Russia

**e-mail: zhukov@beam.ioffe.ru*

Submitted June 2, 2003; accepted for publication June 3, 2003

Abstract—Lasing at 1488–1515 nm in the temperature range 20–83°C was obtained in structures with an active region based on multiply stacked arrays of self-organized quantum dots grown on GaAs substrates. The threshold current density of a laser with four cleaved facets was 800 A/cm2 at room temperature. The method of wavelength extension is based on the use of a metamorphic buffer layer with an In content of about 20% intended for relieving the lattice mismatch stress. *© 2003 MAIK "Nauka/Interperiodica".*

1. INTRODUCTION

Recent progress in the design of injection lasers for the 1.3-μm wavelength range with an active region based on self-organized quantum dots (QD) on GaAs substrates [1, 2] has stimulated further research with the aim of advancing to longer wavelengths: up to 1.55 μm. These structures can serve as an alternative to conventional lasers for this spectral range, based on the InGaAsP/InP system, and they are promising for the design of monolithic vertical-cavity surface-emitting lasers (VCSELs).

As we have shown earlier [3], the lasing wavelength in structures based on self-organized InAs QDs can be raised in a controllable way by making the energy gap of the matrix embedding the QD array narrower. In particular, in the case of deposition onto InP substrates, the use of an $In_{0.53}Ga_{0.47}As$ matrix lattice-matched with the substrate allowed us to reach a lasing wavelength of 1.9 μm [4]. However, in the case of a GaAs substrate, InGaAs layers are lattice-mismatched with the substrate. In terms of the pseudomorphic deposition strategy, the energy gap of an InGaAs matrix is limited to about 1.25 eV, which, in turn, restricts the lasing wavelength of a QD laser to about 1.3–1.35 μm. A significant decrease in the energy gap in the InGaAs matrix embedding the QD array can be achieved if metamorphic heterostructures are used. As shown in [5], when special modes are used for the deposition of an InGaAs buffer layer, the stress is mainly relieved via the formation of mismatch dislocations localized near the interface. This method enables subsequent growth of dislocation-free InGa(Al)As layers with an In content of about 20%, which form the laser structure. The method was applied in [5], and 1.29 μm lasing was obtained in a laser based on two InGaAs quantum wells (QW), where the In content (about 40%) was higher than in the surrounding matrix.

In the present study, the concept of metamorphic growth is applied to produce lasers with an active region based on self-organized QDs. The lasing wavelength at room temperature was 1488 nm, with a threshold current density of 800 A/cm^2. The lasing was observed at temperatures of up to 83°C (1515 nm, 2.5 kA/cm^2).

2. EXPERIMENT

The structures for study were grown on (100) n^+-GaAs substrates in a Riber 32P MBE setup with a solid-state As precursor. Figure 1a shows the band diagram of the basic laser design, further denoted as MMQD1. The mole fraction of In was about 21% in all the layers of the laser structure, except in the active region. A silicon-doped InGaAs buffer of about 1.2 μm in thickness was deposited directly onto the GaAs surface. An undoped InGaAs layer of about 0.7 μm in thickness was used as the laser waveguide, confined by 1.6-μm-thick InAlGaAs *n*- and *p*-type emitter layers, which were doped with Si or Be, respectively, to a concentration of $(5–10) \times 10^{17}$ cm^{-3}. The ratio between the mole fractions of Al and Ga was about 3/5. Ten sheets of self-organized QDs were embedded in the middle of the waveguide layer. Each QD sheet was produced by depositing InAs with an effective thickness of 2.7 monolayers, covered with an $In_{0.4}Ga_{0.6}As$ QW 4 nm in thickness. The thickness of InGaAs spacers between QD sheets was 45 nm. The structure was terminated with an InGaAs contact layer of about 0.4 μm in thickness doped with Be to a concentration of 10^{19} cm^{-3}.

Thus, the structure of MMQD1 metamorphic lasers is close in design to typical QD lasers for the 1.3-μm wavelength range on GaAs substrates. However, the use of a metamorphic heterostructure with an In content of about 21% allows the matrix energy gap to be

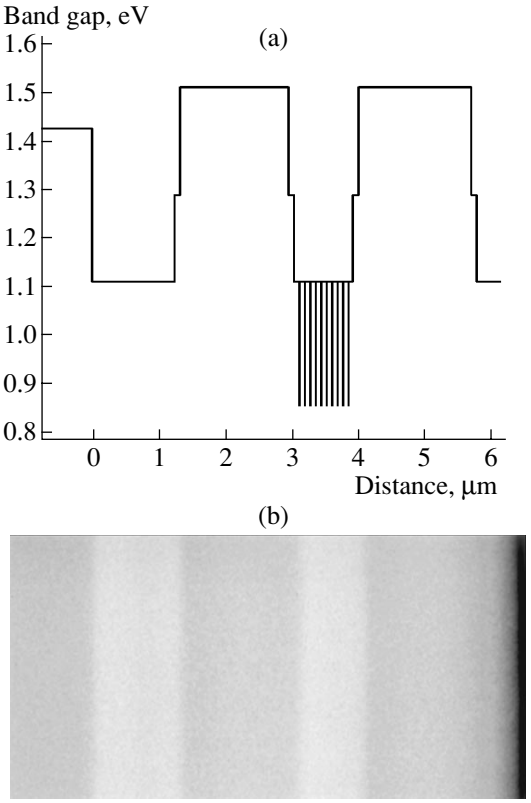

Fig. 1. (a) Band structure of the laser structure under study; (b) cross-sectional SEM image of the structure.

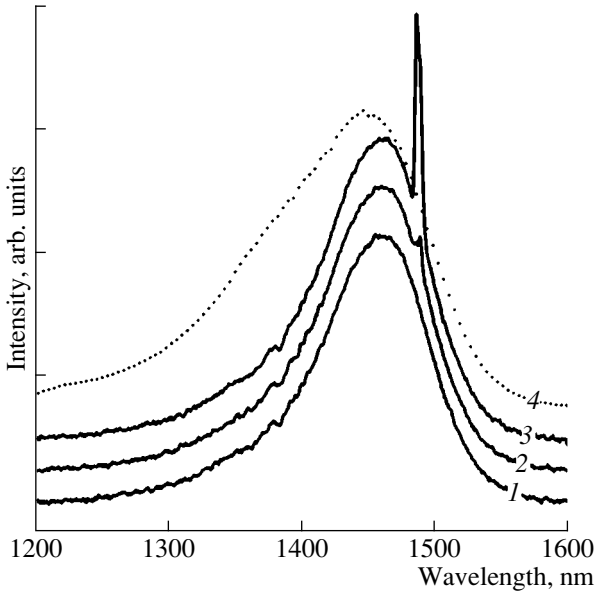

Fig. 2. Solid lines: EL spectra at different driving current densities: (*1*) 770, (*2*) 800, and (*3*) 830 A/cm^2. Dashed line: (*4*) PL spectrum of the laser structure etched in a H_2SO_4 : H_2O_2 : H_2O solution.

reduced to 1.12 eV at room temperature, so that the spectral position of the photoluminescence (PL) peak of the QD array reaches 1.45 μm. Also, the proposed method is an alternative to using InGaAs substrates (see, e.g., [6]), which are now not widely produced.

As can be seen, the mismatch stress in the structure under study is relieved in the InGaAs buffer layer, and the active region is noticeably remote from the GaAs substrate (on average, at a distance of 3 μm). This situation is undesirable from the point of view of applying the metamorphic growth concept for the fabrication of VCSELs, because the total thickness of a structure is limited to a few wavelengths (typically, no more than 2 μm). To test the possibility of reducing the overall thickness of the metamorphic laser structure, the MMQD2 design was used. The main difference between the MMQD2 and the basic MMQD1 design is that the former has no InGaAs buffer layer. The stress is relieved directly in the InGaAlAs:Si layer, which, therefore, serves as the lower emitter and the buffer layer. This makes it possible to bring the active region much closer to the interface with the GaAs substrate.

Lasers with four cleaved facets were produced from the structures grown. *n*- and *p*-type contacts were formed by depositing and fusing-in (450°C) AuGe/Ni/Au and AuZn/Ni/Au metal layers, respectively. The laser characteristics were studied in the temperature range 20–85°C with driving current pulses 0.2 μs in width. A Ge photodiode was used as the signal detector.

3. RESULTS AND DISCUSSION

Figure 1b shows a cross-sectional image, obtained by scanning electron microscopy (SEM), of the MMQD1 laser structure. Noteworthy is the high planarity of all the heterointerfaces, as well as the absence of microcracks, flaking, and other defects of the cleaved surface. The latter fact allows laser cavity mirrors to be formed by cleaving the facets, as in the case of non-metamorphic lasers on GaAs.

The threshold and spectral characteristics of lasers grown in the two different designs described above, MMQD1 and MMQD2, turned out to be very similar. Thus, we shall not discuss the differences between them any further.

Figure 2 shows a PL spectrum recorded at room temperature from the surface of a laser structure in which a contact layer and a fragment of the top emitter were removed. The PL line from the laser active region peaks at a wavelength of 1.45 μm, which corresponds to the PL peak from the QD array, measured in test structures. Thus, the blue shift of the PL line in laser structures with respect to test structures, which has been frequently observed in QD lasers for the 1.3-μm range, does not occur here.

Figure 2 also shows the electroluminescence (EL) spectra of the laser structure recorded from the facet with different driving currents. A lasing line appears at a wavelength of 1488 nm at a threshold current density

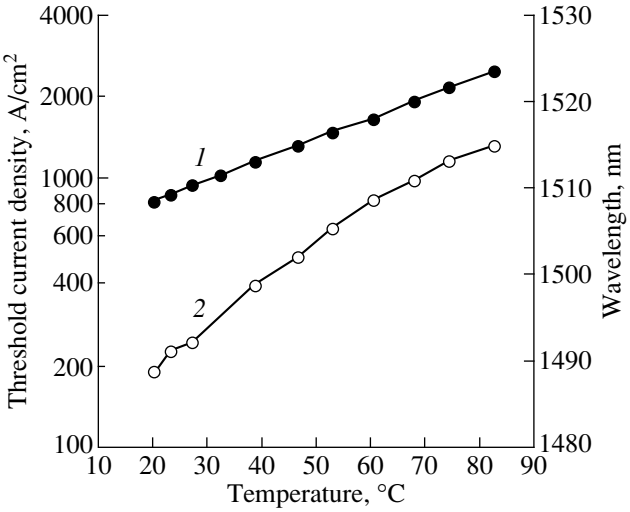

Fig. 3. Temperature dependences of (*1*) the threshold current density and (*2*) the lasing wavelength.

of 800 A/cm^2. The lasing line is appreciably red-shifted with respect to the PL peak, which is indicative of a considerable optical gain margin (the saturated gain considerably exceeds the internal loss). The threshold current densities achieved are to be compared with the best results obtained in lasers based on nitrogen-containing pseudomorphic QWs. As reported in [7, 8], lasing at 1.52 and 1.50 μm was obtained in InGaAsN and InGaAsNSb QW structures, respectively, with threshold current densities of 7 and 3.5 kA/cm^2.

Figure 3 shows the temperature dependences of the threshold current density and lasing wavelength. Lasing is observed up to the highest temperature of the experiment, 83°C. In this case, the wavelength is 1515 nm, and the threshold current density is 2.5 kA/cm^2. The temperature dependence of the lasing wavelength is described by the coefficient 0.5 nm/K, and the threshold current density by the characteristic temperature 60 K.

To conclude, it is worth noting the good electrical characteristics of both laser structures. The cutoff voltage of the current–voltage characteristic of the laser diodes is 0.8 V, which correlates with the expected energy of the ground-state optical transition. This indicates the absence of additional barriers for carrier injection within the metamorphic structure, e.g., at the interfaces between the buffer and the lower emitter, or between the top emitter and the contact layer. The series resistivity is estimated as 2×10^{-4} Ω cm^2.

4. CONCLUSION

Laser structures on GaAs substrates with an active region based on self-organized QDs have been fabricated using the metamorphic growth technique, and lasing in the 1.5-μm spectral range has been obtained. The proposed approach seems promising for the fabrication of VCSELs, as well as for progress toward longer wavelengths.

ACKNOWLEDGMENTS

The authors are grateful to V.M. Busov for the SEM study of the structure properties, Yu.G. Musikhin for the transmission electron microscopy studies, and to M.V. Baidakova for the X-ray diffraction studies.

This study was supported by the Joint Program of the Ioffe Institute and NSC-Nanosemiconductor-GmbH, Germany. A.E.Z. and V.M.U. acknowledge the support of the Russian Science Welfare Social Fund.

REFERENCES

1. A. R. Kovsh, N. A. Maleev, A. E. Zhukov, *et al.*, Electron. Lett. **38**, 1104 (2002).
2. A. E. Zhukov, A. R. Kovsh, S. S. Mikhrin, *et al.*, Physica E (Amsterdam) **17**, 589 (2003).
3. V. M. Ustinov and A. E. Zhukov, Semicond. Sci. Technol. **15**, R41 (2000).
4. V. M. Ustinov, A. E. Zhukov, A. Yu. Egorov, *et al.*, Electron. Lett. **34**, 670 (1998).
5. A. E. Zhukov, A. R. Kovsh, S. S. Mikhrin, *et al.*, Fiz. Tekh. Poluprovodn. (St. Petersburg) **37**, 1143 (2003) [Semiconductors **37**, 1119 (2003)].
6. K. Otsubo, Y. Nishijima, and H. Ishikawa, FUJITSU Sci. Technol. J. **34**, 212 (1998).
7. M. Fischer, D. Gollub, S. Moses, *et al.*, in *Abstract Book of International Workshop on GaAs Based Lasers for 1.3–1.5 μm Wavelength Range* (Wroclaw, Poland, 2003), p. 48.
8. L. H. Li, V. Sallet, G. Patriarche, *et al.*, in *Abstract Book of International Workshop on GaAs Based Lasers for 1.3–1.5 μm Wavelength Range* (Wroclaw, Poland, 2003), p. 49.

Translated by D. Mashovets

Semiconductors, Vol. 37, No. 12, 2003, pp. 1414–1420. Translated from Fizika i Tekhnika Poluprovodnikov, Vol. 37, No. 12, 2003, pp. 1465–1472.

PHYSICS OF SEMICONDUCTOR DEVICES

Properties of GaSb-Based Light-Emitting Diodes with Chemically Cut Substrates

E. A. Grebenshchikova, A. N. Imenkov, B. E. Zhurtanov, T. N. Danilova, A. V. Chernyaev, N. V. Vlasenko, and Yu. P. Yakovlev*

Ioffe Physicotechnical Institute, Russian Academy of Sciences, St. Petersburg, 194021 Russia

**e-mail: Yakovlev@iropto.ioffe.ru*

Submitted April 2, 2003; accepted for publication April 3, 2003

Abstract—Light-emitting diodes for the mid-IR (λ = 1.7–1.9 μm) spectral range were studied. The substrate of GaSb-based light-emitting chips was chemically cut into a conical–pyramidal shape, and the number of chip faces increased from six to ten. Studies of the emission spectra and far-field pattern have shown that chemical cutting raises the external quantum efficiency and makes the far-field pattern almost hemispherical. © *2003 MAIK "Nauka/Interperiodica".*

1. INTRODUCTION

The high refractive index of electroluminescent semiconductors hinders light extraction from the crystal of a light-emitting diode (LED). This is because only a small portion of the light generated in a semiconductor falls onto the external surface at an angle of incidence smaller than the angle of total internal reflection. Only this part of the emitted light passes (taking the transmission coefficient into account) across the surface. The rest is reflected inwards. Even for a spherical surface, only the part of the emitted light generated near the center of the sphere exits outwards. For example, in the case when light is emitted over the entire secant plane, only 11% can pass outwards after the first incidence onto a spherical surface. In a parallelepiped-shaped crystal, 8% of the radiation can cross six faces.

Different methods of texturing a semiconductor surface (formation of a system of pits) to change the angle of inward reflection have been discussed [1–3] in the hope that, after light passes several times across the semiconductor, it will fall onto the surface at an angle smaller than the total internal reflection angle and partially exit outwards. This method makes it possible to raise the fraction of extracted light to ~30% for visible and near-IR LEDs. In the mid-IR range, the multiple-pass technique does not provide the desired result due to the increasing role of absorption by free carriers, which is proportional to the wavelength squared. The reduction of the crystal size to reduce the path length for light impairs heat removal, and, consequently, diminishes the power of the LED. The band-to-band absorption is also more important in narrow-gap than in wide-gap semiconductors due to the lower ionization energy of impurities in the former.

The prospect of a tenfold increase in the efficiency of mid-IR LEDs by means of improving the exit of light from a crystal justifies new research in this area.

The present study considers the possibility of using chemical etching to cut a crystal into a shape that ensures the exit of emitted light. This is a continuation of our research on the design of mid-IR (1.6–2.4 μm) LEDs [4–7], and its goal is to enhance the emissivity of an LED crystal by making it into a special shape.

2. METHODS OF FABRICATING AND STUDYING ELECTROLUMINESCENT STRUCTURES

The LED structures for study were produced by liquid-phase epitaxy on (100) *n*-GaSb substrates that were 400 nm thick [4, 5]. The substrates were doped with Te to an electron density of 8×10^{17} cm^{-3}. First, an active undoped GaSb layer was grown, with rare-earth Gd added to improve the layer perfection. This layer was *p*-type, which is typical of undoped GaSb layers; the thickness of the layer was 1.5 μm. Later, a *p*-$GaAl_{0.34}SbAs$ confining layer with a wider energy gap was grown; it was doped with Ge to a hole density of 1×10^{18} cm^{-3}. Its thickness was 3.5 μm. On top, a 0.5-μm-thick *p*-GaSb contact layer was grown, which was heavily doped with Ge to a hole density of 8×10^{18} cm^{-3}. After that, the wafer was ground and polished to a thickness of 220 μm.

The chemical cutting was performed by contact photolithography as follows. At the first stage, a pattern in the form of squares with sides L = 480 μm and a step of S = 500 μm was formed on the substrate side to delineate the boundaries of single chips. The boundary channels were etched to a depth of 70 μm by electrochemical etching in a CrO_3-based etchant; their width was 160 μm. At the second stage of photolithography, a pattern of circles 300 μm in diameter was formed in the centers of the squares. By etching it in the same way, we obtained structures 140 μm high, each of which had the form of a pyramid at its base and a truncated cone

in its upper part, with a top area 200 μm in diameter (Fig. 1a). At the third stage, a window for ohmic contact 100 μm in diameter was produced by photolithography.

Contact layers were formed by successive deposition of Cr, Au + Te alloy, and Au in a VUP-4 vacuum installation. Then the contact layers were fired-in at a temperature of 250°C for 1 min. Contacts to the *p*-region were formed by successive deposition of Cr, Au + Te alloy, and Au onto the whole surface of the *p*-GaSb contact layer with subsequent firing-in in the above-mentioned mode. Then, the wafers were divided into separate chips. Each chip was mounted, with the epitaxial layer (epilayer) down, on a TO-18 LED crystal holder with a flat table.

For comparison with LEDs produced by the deep etching method, devices of conventional design (Figs. 1b, 1c) were fabricated. In this case, the above-described squares were formed on the *n*-side of one wafer (Fig. 1b) and the *p*-side of another (Fig. 1c), and 15-μm-deep channels were etched to form the separating grid. After repeated photolithography, round contacts 100 μm in diameter were formed at this side. An ohmic contact was formed over the total area of the opposite side. The wafers were divided into separate chips, and the chips were mounted on crystal holders, with the solid contact down.

Spectral characteristics of LEDs were recorded in a range of 1.4–2.4 μm in a setup using a CVI Laser Corporation monochromator (California, USA). The photodetector was an InSb photodiode shipped with an EG & G JUDSON preamplifier. The peak sensitivity of this photodiode (at $\lambda = 5$ μm) is 3.5 A/W, with the photoelectric threshold at 5.3 μm. The signal was recorded using a Stanford Research Systems selective voltmeter (USA). The average emission power of the LEDs was determined as a quantity proportional to the integral of the spectral curve, taken over the entire spectrum. The following parameters were taken into account: the fraction of light incident on the photodetector, reflectivity of the diffraction grating, photodetector sensitivity at the given wavelength, and preamplifier gain, as well as the modification of the signal by the selective voltmeter (the output amplitude differs from the input signal amplitude by the coefficient of the first harmonic in the Fourier transform of the square-wave signal into the sum of sinusoidal signals).

Additionally, control measurements of the average emission power of LEDs were taken using an Orphir NOVA milliwattmeter (Israel).

The far-field pattern of the LED emission was studied using an original setup in which the LED was rotated around the axis lying in the *p*–*n* junction plane. Two directions of axis were chosen: parallel to the sides of the square limiting the *p*–*n* junction plane or along its diagonal. For this purpose, an LED was turned by 45°. The far-field patterns were obtained in two planes. One of these was parallel to the side faces of a chip, the other was at an angle of 45° to it. An LED was driven by square current pulses with a duty cycle of 50% and a repetition rate of about 1 kHz. The light emitted was detected by an uncooled PbSe photoresistor situated at a distance of 5 cm from the LED; the width of the photosensitive area was 1 mm; its length, 4 mm.

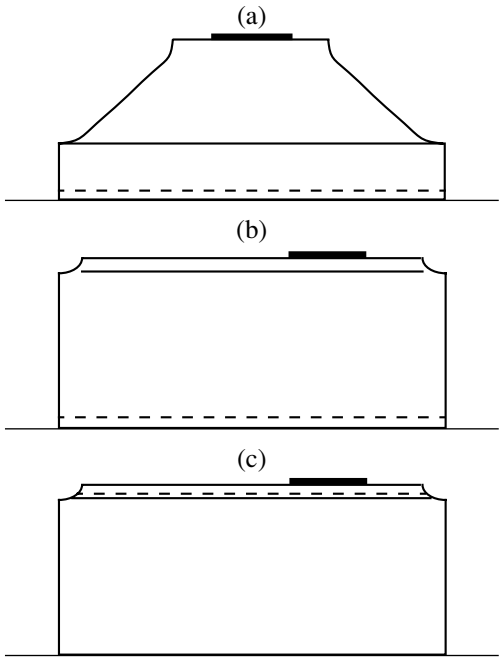

Fig. 1. Designs of three types of LED chips: (a) with a conical–pyramidal substrate part; (b) in the shape of a parallelepiped with its epitaxial part soldered to the crystal holder; (c) in the shape of a parallelepiped with its substrate part soldered to the crystal holder.

The electrical signal obtained was amplified by a V6-9 selective voltmeter, lock-in detected, and recorded by an electronic recorder, and it was also fed into a computer for processing. The measurements were done at room temperature (297 K).

3. EMISSION SPECTRA

The emission spectra of LEDs with different crystal shapes turned out to be different (Fig. 2). First, we will discuss the emission spectra at small currents (50–150 mA). In the case of the parallelepiped-shaped crystal with substrate soldered to the crystal holder (Fig. 2, curve *1*), a spectral doublet is observed with peaks at 1.76 and 1.9 μm (the photon energies are 0.705 and 0.65 eV; the FWHM of bands, 0.06 and 0.07 eV, respectively).

A similar crystal with epilayer soldered to the crystal holder actually emits a single band, with its parameters nearly coinciding with those of the long-wavelength band of the doublet mentioned above. The peak wavelength is 1.87 μm (0.66 eV); the FWHM, 0.06 eV (Fig. 2, curve *2*).

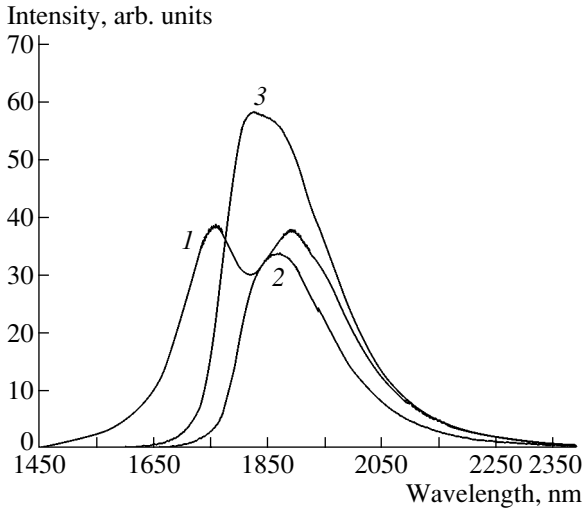

Fig. 2. Emission spectra (at 150 mA current) for LEDs of three designs: (*1*) standard parallelepiped with its substrate part soldered to the holder; (*2*) the same with the epitaxial part soldered to the holder; and (*3*) with a conical–pyramidal deep-etched substrate part.

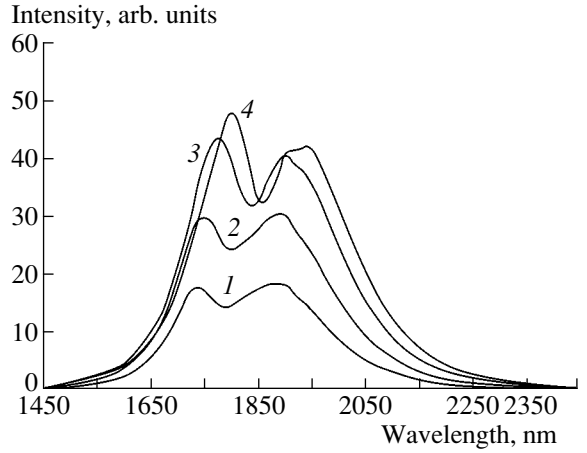

Fig. 3. Emission spectra of a parallelepiped-shaped LED with substrate soldered to the sample holder at different currents: (*1*) 50, (*2*) 100, (*3*) 200, and (*4*) 300 mA.

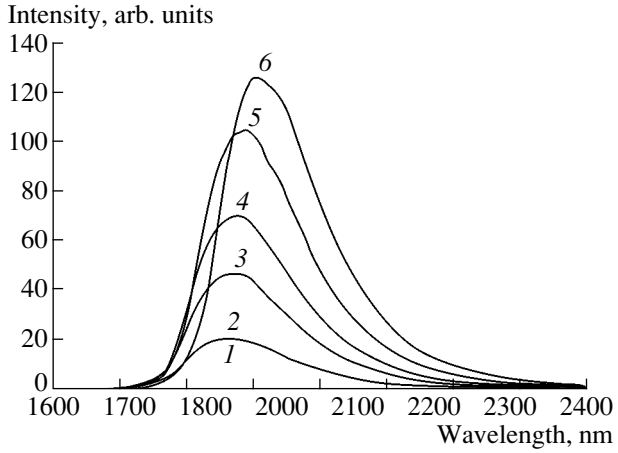

Fig. 4. Emission spectra of a parallelepiped-shaped LED with epitaxial part soldered to the sample holder. Current: (*1*) 50, (*2*) 100, (*3*) 200, (*4*) 300 (*5*) 500, and (*6*) 800 mA.

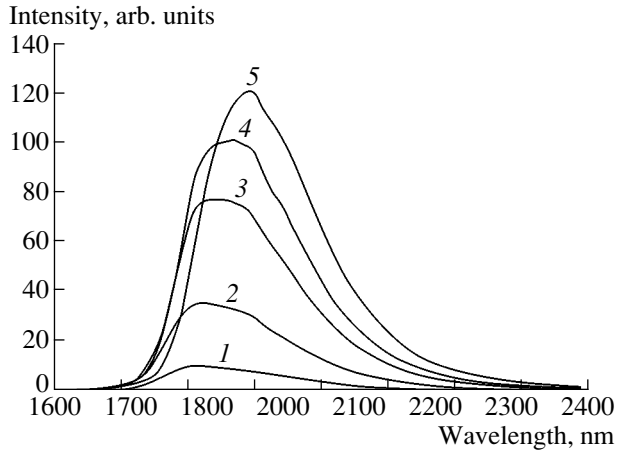

Fig. 5. Emission spectra of an LED with a deep-etched conical–pyramidal substrate part. Current: (*1*) 40, (*2*) 100, (*3*) 200, (*4*) 275, and (*5*) 395 mA.

The deep-etched pyramidal crystal emits a single wide band with a nearly flat peak at a wavelength of 1.83 μm (0.68 eV), with an FWHM of 0.08 eV (Fig. 2, curve *3*).

LEDs with substrate soldered to the crystal holder (Fig. 3) exhibit a red shift of the short-wavelength band over the whole range of currents from 50 to 300 mA. The long-wavelength band of the doublet shifts only at higher currents, above 200 mA. For LEDs with the contact epilayer soldered to the crystal holder (Figs. 4, 5), the shape of the emission spectra does not depend on current in the range 50–250 mA. As the current is further increased, the spectra are shifted to longer wavelengths.

The dependence of the intensity of emitted light on current is sublinear at currents above 100 mA (Fig. 6). In the LEDs mounted on the crystal holder with their contact epilayer down, a superlinear dependence of the intensity of emitted light on current is observed at currents below 50 mA (Fig. 6, curves *2*, *3*). When the substrate of a crystal is soldered to the crystal holder, the superlinear portion of the characteristic is not observed (Fig. 6, curve *1*). At currents below 200 mA, these LEDs show higher emission efficiency than the LEDs with epilayer soldered to the crystal holder. However, at currents of 200–250 mA, the intensity of light emitted by the former ceases to grow with increasing current, and they become inferior to LEDs with deep etching of the substrate part and the emitting part close to the crystal holder. As regards the intensity of the long-wavelength band, they are also inferior at small currents.

Table 1 lists the external quantum efficiencies of the emission, η_{ext}, at a current of 300 mA for LEDs whose light–current characteristics are shown in Fig. 6. Also listed are the average emission wavelengths λ and the photon energies $h\nu$ used in the calculation of the external quantum efficiency. As can be seen from Table 1, LED no. 3 with a deep-etched substrate part shows the

highest external quantum efficiency of emission as compared with parallelepiped-shaped LEDs.

Thus, deep etching of the substrate part of the wafer with the formation of a pyramidal–conical LED chip and mounting on the crystal holder with the epitaxial side down provides better conditions for the exit of light of the long-wavelength emission band than the standard design, especially at high currents.

4. FAR-FIELD PATTERN

Each shape of the LED crystal is found to have a specific far-field pattern of emission (Figs. 7–9).

In the case of the parallelepiped-shaped crystal with substrate soldered to the crystal holder (Fig. 7), the intensity of emitted light is the highest in the direction normal to the epilayer, and it falls smoothly as the angle of deviation from this direction increases. In the plane parallel to the side faces, the intensity of light emitted at intermediate angles is smaller than in the plane containing the diagonal of the epilayer. The difference between these intensities is the greatest at angles of +70° and –70°.

In the case when a similar crystal is soldered to the crystal holder with its contact epilayer down (Fig. 8), the intensity of emitted light shows peaks at deviation angles of +40° and –40°, with a sharp dip in between. In the plane parallel to the side faces, the intensity at intermediate deviation angles is also lower than in the plane containing the epilayer diagonal.

In the case of crystals with a deep-etched substrate part soldered to the crystal holder with the contact epilayer down, a weak angular dependence of the emission intensity is typical (Fig. 9). In this weak dependence, the intensity of the light emitted first increases by 10–15% as the angle changes from zero to 70°–80° and then drops abruptly to zero at an angle of 110°, which means that there is virtually a plateau in the range of angles from –80° to 80°. We can say that the emission is omnidirectional.

In the scanning plane parallel to the side faces, the intensity of light emitted at intermediate deviation angles is 10–15% lower than in the plane containing the diagonal of the epilayer.

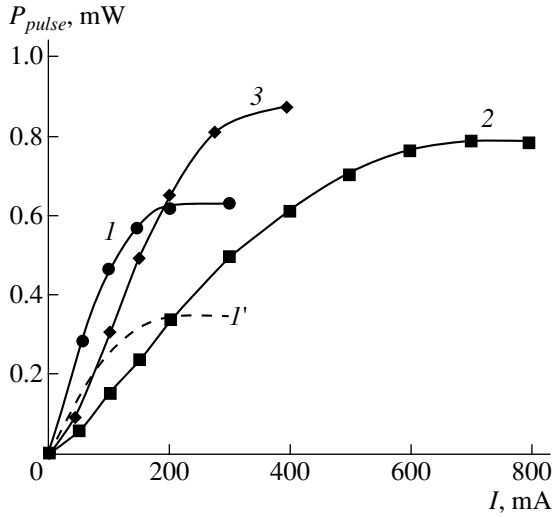

Fig. 6. Pulsed emission power vs. current at the pulse frequency 512 Hz and duty cycle 50%: (*1*–*3*) for the three LED designs mentioned in the caption to Fig. 2; (*1*') for the long-wavelength band of the LED of the first design.

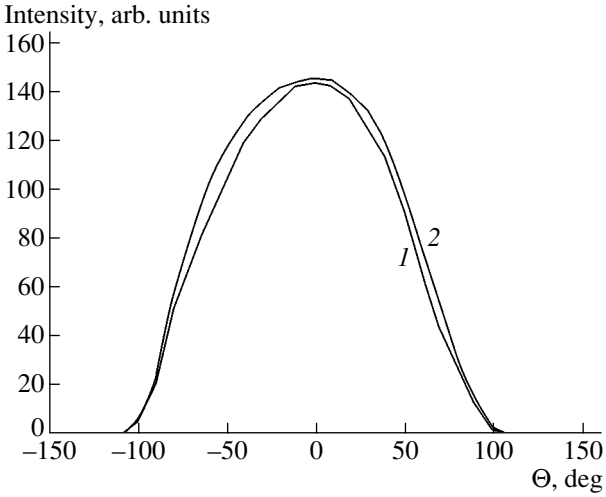

Fig. 7. Far-field pattern of a parallelepiped-shaped LED with substrate soldered to the sample holder for two planes perpendicular to the *p*–*n* junction plane: (*1*) parallel to the lateral faces of the chip and (*2*) containing the diagonal of the *p*–*n* junction plane.

5. DISCUSSION

The smallest distortion of the emission spectra is observed for chips mounted on the crystal holder with their substrate down, i.e., with the emitting epilayer facing outwards. This is because these crystals have a short optical path for the exit of emitted light across the wide-bandgap epilayer. It is worth noting that the difference between the energy gap and the energies of the short- and the long-wavelength spectral peaks are equal to, respectively, the ionization energy of a single-charged acceptor (0.02 eV) and its approximately quadrupled value. This fact suggests that double-charged acceptors are involved in the emission process. Double-charged acceptors are formed when Ga occupies Sb sites in the crystal lattice; this is typical of GaSb, which is distinguished by a significant nonstoichiometry. It is not nec-

Table 1

No.	P, mW	λ, μm	$h\nu$, eV	η_{ext}, %
1	0.62	1.85	0.67	0.31
2	0.49	1.87	0.663	0.24
3	0.83	1.86	0.667	0.42

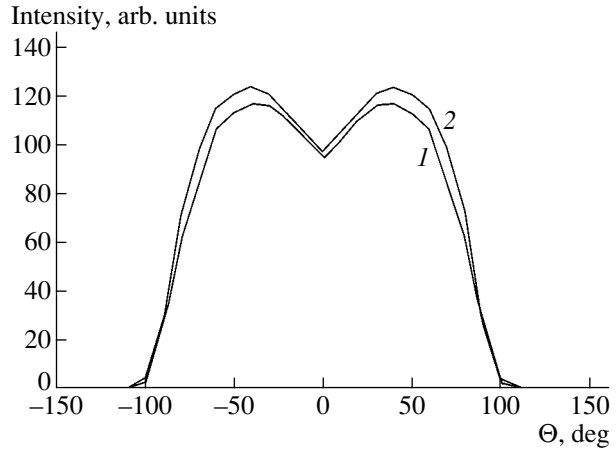

Fig. 8. Far-field pattern of a parallelepiped-shaped LED with its epitaxial part soldered to the sample holder. The measurement conditions were the same as in Fig. 7.

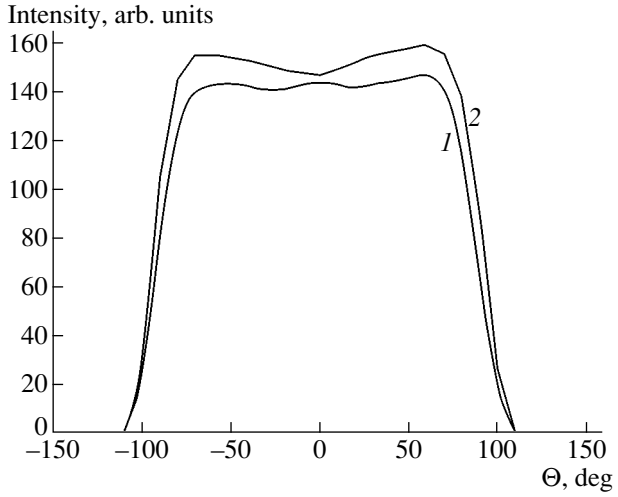

Fig. 9. Far-field pattern of an LED with deep-etched conical–pyramidal substrate part. The measurement conditions were the same as in Fig. 7.

essary to assume the presence of other acceptors because they were not introduced intentionally, and the epilayer was purified with Gd.

The presence of only the long-wavelength emission band in the case when the LED chip is soldered to the crystal holder with its epilayer side down indicates a strong absorption of the short-wavelength band in the chip bulk, i.e., in GaSb. This is basically band-to-band absorption (via the "tails" of allowed bands), since the long-wavelength band is absorbed to a much lesser extent. In this case, a short optical path exists only for light generated near the lateral faces of the chip, and the contribution of this light is small.

The short-wavelength band is noticeable in the emission spectra of deep-etched crystals. If the spectrum is represented in the form of two bands, the short-wavelength band is only twice as weak as the long-wavelength one. This indicates that deep etching makes the optical path for the emitted light shorter.

The light–current dependences demonstrate the advantage of the LED in which the chip is mounted on the crystal holder with its substrate down (in this case, the generating region is close to the outer surface) at low currents (below 200 mA). However, if a comparison is made for a long-wavelength weakly absorbed band, this advantage vanishes. At high operating currents (about 800 mA), chips mounted in such a way that the generating region is close to the heat-transfer surface of the sample holder are undeniably preferable. LEDs with the generating region close to the outer surface with an ohmic contact on it have one more undesirable effect: the light emitted is concentrated under the contact, which results in a strong decrease in the differential efficiency as the current increases and a high current density under the contact. The latter effect suppresses the superlinear portion of the light–current characteristic with small currents. The contribution of the nonradiative Auger recombination also increases because of the increase in the density of nonequilibrium carriers. The emission efficiency decreases.

The recombination current I_c concentrated under the round contact (in an area much smaller than that of the emitting layer) is related to the current I outside of it by

$$I = 2I_\sigma(1 + \sqrt{1 + I_c/I_\sigma}), \qquad (1)$$

where $I_\sigma = 2\pi\sigma b\beta kT/q$; σ is the average conductivity of the p-region; b, its thickness; kT, the thermal energy; q, the elementary charge; and β, the index of mono- ($\beta = 1$) or bimolecularity ($\beta = 0.5$) of the recombination process. For $\beta = 1$, $KT/q = 0.0256$ V, $b = 5$ μm, and $\sigma = 200\ \Omega^{-1}\,\mathrm{cm}^{-1}$, we obtain $I_\sigma = 16$ mA. For these transport parameters of the epilayer, in accordance with (1), the current starts to concentrate under the contact at 100 mA, when 80% of the current flows outside the contact. At 250 mA, only half the current appears not to be under the contact. This calculation correlates with the experiment. At small currents $I < 4I_\sigma = 64$ mA, when the spreading is complete, relation (1) is invalid, and the ratio of currents under the contact and outside of it equals the ratio of the contact area to the area of the GaSb contact layer not covered by the contact plate. In our case, it equals 3%.

Therefore, the effect of the concentration of emitted light under the ohmic contact makes a small-area ohmic contact on a thin p-region undesirable.

Now we will discuss heat removal.

The thermal resistance of a parallelepiped-shaped chip is given by

$$R_T = \frac{H}{S\chi}, \qquad (2)$$

Table 2

No.	dP/dI, mW A^{-1}	$h\nu$, eV	η_{ext}, %	η_F, %	η_{int}, %	η_{exit}, %
1	5.2	0.67	0.78	0.6	58	1.37
2	1.85	0.663	0.28		58	0.48
3	3.92	0.667	0.59		58	1.02

where H is the height of the parallelepiped, S is its area, and χ is the thermal conductivity. For $H = 220$ μm and $S = 0.0025$ cm^2 and $\chi = 0.336$ W/(cm K), we obtain $R_T = 26$ K/W. This thermal resistance is obtained for uniform heat release in the emitting layer and for a crystal mounted on the crystal holder with its substrate down. The concentration of the recombination under the contact raises the thermal resistance severalfold.

Heat is released in the emitting layer mainly due to nonradiative recombination, and, therefore, the thermal resistance should be calculated using Eq. (2) when this mechanism dominates. If the internal quantum efficiency of emission is high, heat is mainly released upon absorption of light in the semiconductor bulk. In the case of uniform absorption of light, the heat resistance is half of that given by Eq. (2), irrespective of the position of the emitting layer. This gives us wide scope for the choice of shape of the LED chip.

The thermal resistance of the crystal holder employed (TO-18 crystal holder, gold-plated, Au layer ~0.2 μm in thickness) is primarily concentrated in the nickel table with thickness $\delta = 0.02$ cm and diameter $D = 0.4$ cm and can be expressed by the approximate relation

$$R_H = \frac{1}{2\pi\chi\delta}\ln\frac{\pi D}{L}, \qquad (3)$$

where L is the crystal perimeter and χ is the thermal conductivity of Ni. For $L = 0.2$ cm and $\chi = 0.59$ W/(cm K), we have $R_H = 25$ K/W, i.e., nearly the same value as that obtained from Eq. (2) for a semiconductor chip. The thermal resistivity of a thin (0.2 μm) Au coating of the crystal holder is negligible. This estimate demonstrates that the thermal resistance of the crystal holder makes a significant contribution to the shift of the long-wavelength spectral band as the current rises both in LED crystals of pyramidal–conical shape and those of standard shape at high currents (>200 mA). The red shift of the short-wavelength band, which occurs even at small currents, is related to the concentration of emitted light under the contact, accompanied by the corresponding increase in the optical path for emitted light.

Now we move on to analyze the far-field pattern of the emission.

In the standard LED design with a parallelepiped-shaped chip soldered to the crystal holder with its substrate down, the far-field pattern of emission is close to cosine, because the emitted light mainly exits across the surface of the epitaxial part (~75%). The predominant exit of light across the lateral faces (~67%) is observed in the far-field patterns of parallelepipeds soldered to the crystal holder with their epitaxial part down. The intensity of emitted light at zero angle is defined only by its exit across the upper face parallel to the table of the crystal holder. For nonzero angles, the emission across the lateral faces is added. One lateral face is to be taken into account in the summation in the case of scanning in planes parallel to lateral faces, and two, in the case of diagonal scanning. Therefore, the intensity of emitted light is higher in diagonal directions. The analysis of far-field patterns shows that the intensity distribution of light emitted across any face is cosine.

In the case of deep etching, when the chip has the shape of a pyramid with smoothed faces placed on a parallelepiped-shaped pedestal, the emission is nearly omnidirectional, as in the case of a spherical chip. This is due to the increase in the number of light-transmitting faces from five to nine, four of which are inclined at an angle of ~45° relative to the emitting region. The inclined faces are rather convex, which enhances the exit of emitted light and reduces the directionality and number of light passes within the chip.

Furthermore, deep etching makes the optical path of emitted light shorter, thus reducing the absorption, which is manifested by the presence of the short-wavelength band in the emission spectrum.

Thus, chemical cutting of an LED chip brings the far-field pattern of emission closer to that corresponding to a spherical chip, thus enhancing the exit of emitted light.

Now we estimate the internal quantum efficiency of emission, η_{int}, for the case of electron transitions between the conduction band and the levels of natural double-charged acceptors in GaSb. First, the differential external quantum efficiency η_{ext} for LEDs of different designs is determined from the experimentally defined derivative of the emission power with respect to current dP/dI and the average photon energy $h\nu$ (Table 2). Here, the current chosen (50 mA) is small enough so that its concentration under contact is weak (3%) but sufficient for deep levels, which are of no interest to us, to be saturated. We use the condition that, in the case of LEDs with the epitaxial part in the frontal position, light mainly exits across the thin nonabsorbing epilayers. The external quantum efficiency of emission across the top face η_F can be calculated using the ratio of the intensities of light emitted in the directions normal to

the lateral and top faces, f, and the fact that we have mirror reflection from the crystal holder:

$$\eta_F = \frac{\eta_{ext}}{1+2f}. \quad (4)$$

For the experimental value $f = 0.15$, we obtain $\eta_F = 0.47\%$ (Table 2). Using η_F and the theoretical fraction of light exiting across a single face η_{th}, which is 1.07% for GaSb, we determine η_{int}, taking into account that the fraction γ of current is concentrated under the contact:

$$\eta_{int} = \frac{\eta_F}{(1-\gamma)\eta_{th}}. \quad (5)$$

The value obtained, $\eta_{int} = 58\%$, is quite sufficient to use electroluminescence involving double-charged acceptors in LEDs. Now, each LED design can be characterized by a coefficient describing the exit of emitted light $\eta_{exit} = \eta_{ext}/\eta_{int}$. At small current (50 mA), the highest exit coefficient of 1.34% is obtained for the LED with a parallelepiped-shaped chip soldered to the crystal holder with its substrate down (Table 2). The LED with the same shape of chip but soldered to the holder with the opposite side down has an exit coefficient that is inferior to the preceding LED by a factor of 3, due to the longer optical path of the emitted light to the face. The LED with a deep-etched substrate part is exceeded by the high-efficiency diode by only a factor of 1.3. However, at high currents ($I > 200$ mA), the former demonstrates the highest external quantum efficiency of emission owing to better heat removal, the absence of current concentration under the contact, and the additional output of emitted light across four new inclined faces.

6. CONCLUSION

Multistage photolithography with electrochemical etching allows one to substantially modify the shape of the LED chip, the emission spectrum, its far-field pattern, and the exit coefficient. The method allows one to fabricate a perfect standard parallelepiped-shaped chip mountable on a crystal holder with its substrate or epitaxial part down. In the first design, an undistorted exit of emitted light across the front face is achieved at currents below 200 mA, when the current concentration under the ohmic contact is insignificant. When the chip is soldered to the crystal holder with its epitaxial part down, the range of operating currents expands to 800 mA owing to better heat removal, but the short-wavelength emission is strongly suppressed due to the longer path from the emission region to the front face of the chip.

Deep etching of the substrate part allows the chip to be shaped into the form of a truncated pyramidal–conical structure on a thin pedestal, which contains the epitaxial part. The mounting of this chip on the sample holder, with its epitaxial part down, provides high operating currents and reduces the absorption of the short-wavelength component of the emitted light. This design offers advantages over the others at currents above 200 mA.

ACKNOWLEDGMENTS

The authors are grateful to E.V. Kuznetsova and S.S. Evdokimova for assembling LEDs.

REFERENCES

1. Zh. I. Alferov, V. M. Andreev, D. Z. Garbuzov, *et al.*, Zh. Tekh. Fiz. **46**, 1066 (1976) [Sov. Phys. Tech. Phys. **21**, 625 (1976)].
2. I. Schnitzer, E. Yablonovitch, C. Caneau, *et al.*, Appl. Phys. Lett. **63**, 2174 (1993).
3. R. Windishc, P. Heremans, P. Kiessel, *et al.*, Appl. Phys. Lett. **74**, 2256 (1999).
4. A. A. Andaspaeva, A. N. Baranov, A. A. Guseĭnov, *et al.*, Pis'ma Zh. Tekh. Fiz. **15** (18), 71 (1989) [Sov. Tech. Phys. Lett. **15**, 734 (1989)].
5. A. A. Andaspaeva, A. N. Baranov, A. A. Guseĭnov, *et al.*, Fiz. Tekh. Poluprovodn. (Leningrad) **24**, 1708 (1990) [Sov. Phys. Semicond. **24**, 1067 (1990)].
6. T. N. Danilova, B. E. Zhurtanov, A. P. Zakgeĭm, *et al.*, Fiz. Tekh. Poluprovodn. (St. Petersburg) **33**, 239 (1999) [Semiconductors **33**, 206 (1999)].
7. B. Zhurtanov, É. V. Ivanov, A. N. Imenkov, *et al.*, Pis'ma Zh. Tekh. Fiz. **27** (5), 1 (2001) [Tech. Phys. Lett. **27**, 173 (2001)].

Translated by D. Mashovets

Semiconductors, Vol. 37, No. 12, 2003, pp. 1421–1424. Translated from Fizika i Tekhnika Poluprovodnikov, Vol. 37, No. 12, 2003, pp. 1473–1476.

PHYSICS OF SEMICONDUCTOR DEVICES

MOCVD GaInAsP/GaInP/AlGaInP Laser Structures Emitting at 780 nm

D. A. Vinokurov*, S. A. Zorina, V. A. Kapitonov, A. Yu. Leshko, A. V. Lyutetskiĭ, D. N. Nikolaev, N. A. Pikhtin, A. L. Stankevich, N. V. Fetisova, V. V. Shamakhov, and I. S. Tarasov

Ioffe Physicotechnical Institute, Russian Academy of Sciences, Politekhnicheskaya ul. 26, St. Petersburg, 194021 Russia

**e-mail: dmitry.vinokurov@pop.ioffe.rssi.ru*

Submitted May 19, 2003; accepted for publication May 20, 2003

Abstract—Metal-organic chemical vapor deposition (MOCVD) was used to form laser heterostructures in the system of GaInAsP/GaInP/AlGaInP solid solutions. The design of the laser structure was chosen on the basis of the calculated band offsets at the heteroboundaries in the active region of the waveguide. A maximal optical power of 320 mW is attained at the output of the mesa-stripe diode laser with a stripe width of $W = 5$ μm in continuous-wave mode at 780 nm. © *2003 MAIK "Nauka/Interperiodica".*

INTRODUCTION

Diode lasers emitting at 780 nm are widely used in computer memory systems, for high-resolution laser printing, in spectroscopy, medicine, and for pumping solid-state lasers. Traditionally, such lasers are fabricated on the basis of an AlGaAs/GaAs system with an AlGaAs active region.

However, structures with an aluminum-free active region have better power characteristics in the range from 800 to 980 nm [1, 2]. Moreover, the threshold of catastrophic optical mirror damage (COMD) obtained in such structures was nearly twice as large as that for AlGaAs/GaAs-based lasers [3]. This circumstance can be explained by the high susceptibility of aluminum to oxidation, which results in enhanced concentration of oxygen in the active region and, therefore, leads to the bulk degradation of the laser structure. Moreover, the higher surface-recombination rate in Al-containing layers as compared to that in GaInAsP-based layers also reduces their COMD level [3].

However, the production of GaInAsP/GaInP high-power diode lasers with an operation wavelength shorter than 800 nm encounters a number of difficulties.

(i) GaInAsP solid solutions that match GaAs substrates and have band gaps corresponding to a lasing wavelength between 700 and 800 nm fall in an unstable region [4, 5]. This may cause spinodal decomposition of the solid solution and, hence, impair the power and threshold characteristics of lasers.

(ii) Because of a small band offset on the boundary between the active region and the waveguide layers in GaInP/GaInAsP heterostructures [6], the emission of carriers from the active region becomes important for lasing at 760–780 nm. By using materials with wider band gaps, such as AlGaAs and AlGaInP, one can diminish the leakage.

The problems specified are mainly solved by the following means.

(1) Using a wide-gap AlGaAs emitter layer, GaInP waveguide layer, and GaInAsP active region [7] allows one to increase the band offset at the boundary between the active region and the waveguide. However, in the range of commonly used compositions x, the heterojunction $Al_xGa_{1-x}As$/GaInP may turn to be of the second type (this will be shown below), which additionally increases the loss in the laser system.

(2) Laser structures containing tensile-stressed strained active region GaAsP and an AlGaAs-based waveguide and emitter layers are considered in [8–10]. There, the problem of solid-solution instability in the active region is solved. However, high strain (1%) in the GaAsP layer with the band gap corresponding to a wavelength of 760 nm and the complexity of the procedure required for the formation of an AlGaAs/GaAsP boundary promote the degradation of lasers. Nevertheless, an unprecedentedly high emission power of 6.4 W at 780 nm was obtained in this system with a stripe width of 100 μm [8].

(3) Lasing in the range 700–780 nm was obtained in a system with the quaternary solid solutions AlGaInP and GaInAsP used as materials for the emitter and the active layers, respectively [3, 11]. The waveguide layers were formed of GaInP. The power emitted by such structures was as high as 3 W at 732 nm with an aperture of 100 μm.

EXPERIMENTAL

The heterostructures under study were obtained by metal-organic chemical vapor deposition (MOCVD) using an Emcore GS3100 setup with a vertical reactor. The growth proceeded in conditions of a reduced pressure of 77 Torr, a substrate-holder rotational velocity of

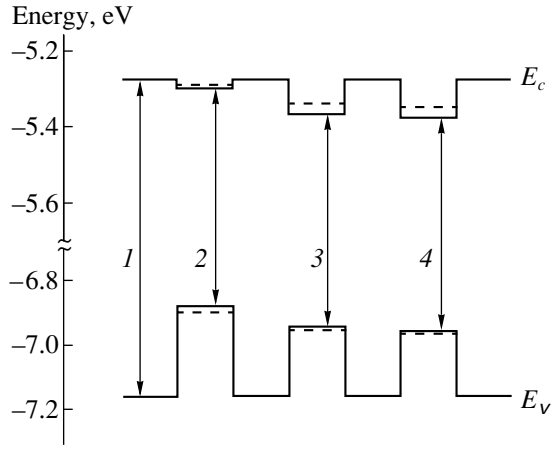

Fig. 1. Energy-band diagram of a double heterostructure including wide-gap solid solution $Ga_{0.51}In_{0.49}P$ and an active region of Ga(In)AsP: (*1*) $Ga_{0.51}In_{0.49}P$, (*2*) $GaAs_{0.77}P_{0.23}$, (*3*) $Ga_{0.8}In_{0.2}As_{0.6}P_{0.4}$, and (*4*) $Ga_{0.74}In_{0.26}As_{0.53}P_{0.47}$. Dashed lines indicate the size-quantization levels.

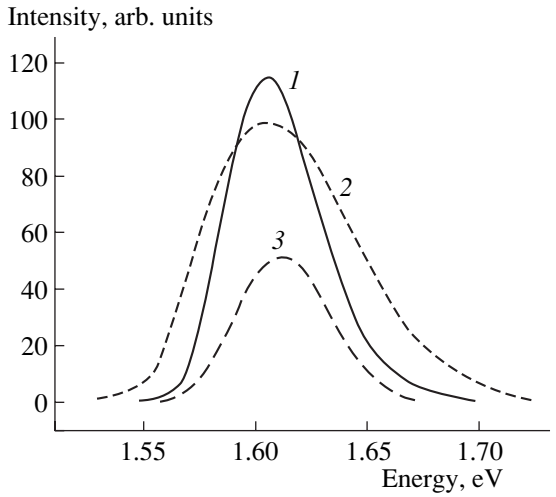

Fig. 2. Photoluminescence spectra of Ga(In)AsP-system solid solutions at 300 K: (*1*) $Ga_{0.74}In_{0.26}As_{0.53}P_{0.47}$, (*2*) $Ga_{0.8}In_{0.2}As_{0.6}P_{0.4}$, and (*3*) $GaAs_{0.77}P_{0.23}$.

1000 rpm, and a temperature of 700°C. As reactants, we used trimethylgallium (TMGa), trimethylindium (TMIn), trimethylaluminum (TMAl), arsine (AsH_3), and phosphine (PH_3). Bicyclopentadienylmagnesium (Cp_3Mg) and monosilane (SiH_4) were the *n*- and *p*-type dopants, respectively. Hydrogen was employed as the carrier gas.

GROUNDS FOR THE CHOICE OF DESIGN OF THE LASER HETEROSTRUCTURE

Photoluminescence (PL) spectra were studied for isotype double heterostructures $Ga_{0.51}In_{0.49}P/Ga(In)AsP/Ga_{0.51}In_{0.49}P$ grown on GaAs (100) substrates. The structures were undoped, and the electron concentration due to background impurities did not exceed 5×10^{15} cm^{-3}. As the active-region material, we used strained $GaAs_{0.77}P_{0.23}$ ($\Delta a/a = -0.8\%$) and $Ga_{0.74}In_{0.26}As_{0.53}P_{0.47}$ ($\Delta a/a = 0.2\%$), as well as $Ga_{0.8}In_{0.2}As_{0.6}P_{0.4}$ matched with the GaAs lattice.

For each of these solid solutions, the band offsets with respect to $Ga_{0.51}In_{0.49}P$ were preliminarily calculated according to [12] and taking into account stresses. The band-gap values were derived from the interpolation dependences [13]. The size-quantization effects were also taken into consideration. The compositions were chosen based on the condition that, with stresses and size-quantization effects taken into account, the PL band peaks at 770 nm. Figure 1 shows the schematic representation of the conduction and the valence band in the solid solutions analyzed with respect to those in $Ga_{0.51}In_{0.49}P$; the dashed line indicates the first quantization level. In all of the cases presented, the transition is seen to be of type I. Strained quaternary and ternary $GaAs_{0.77}P_{0.23}$ solid solutions have, respectively, the deepest and the shallowest electronic quantum wells.

Figure 2 shows the PL spectra typical of solid solutions at 300 K. It can be seen that the PL peak intensity for the ternary solid solution is substantially lower than those for the quaternary solutions. This fact may be related to the shallower electronic quantum well in GaAsP compared to that in the quaternary solid solutions and, therefore, the easier thermal emission of carriers from it. Because of this circumstance, we chose the quaternary solid solutions for the active region. Studying the PL spectra of the quaternary solid solutions, we found that the half-width of the spectrum of an unstrained SS (75 meV) appreciably exceeds that of a strained one (50 meV), and the spectrum is noticeably extended into the high-energy region. These special features of the PL spectrum of an unstrained solid-solution layer can be explained by its inhomogeneous composition, which may result from decomposition of the solid solution in the unstable region [14–16]. The PL spectrum of a strained solid solution corresponds to the spectra of homogeneous solid solutions described in [17] despite the fact that its composition also falls in the unstable region. In this case, the homogeneity of the deposited layer is due to stresses between the layer and the substrate. It is known [18] that the elastic energy of the substrate produces a stabilizing effect on unstable solid solutions and hinders their decomposition. From the analysis of PL spectra, we chose a strained quaternary solid solution as the material for the active region of the laser heterostructure.

The properties of a laser structure also largely depend on the morphology and the crystal quality of the emitter and the waveguide layers. As a waveguide layer, we used $Ga_{0.51}In_{0.49}P$ since it has the widest band gap of aluminum-free solid solutions. The emitter was made of a $(Al_xGa_{1-x})_{0.51}In_{0.49}P$ ($x = 0.18$) solid solution. This material was chosen because its heterojunction with

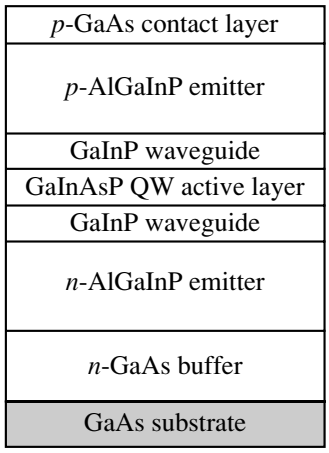

Fig. 3. Schematic representation of laser heterostructure GaInAsP/GaInP/AlGaInP.

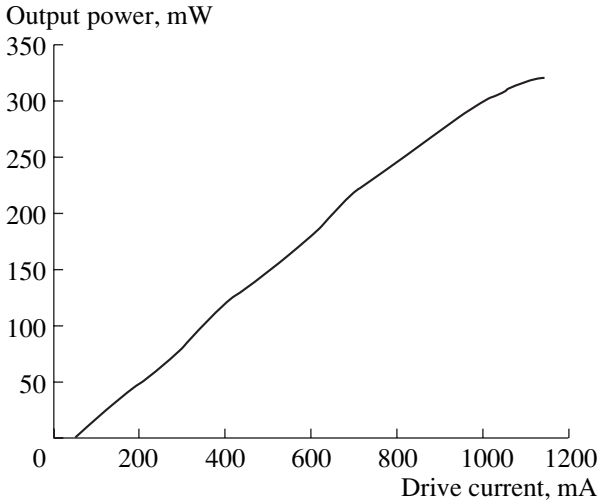

Fig. 4. Power–current characteristic of a GaInAsP/GaInP/AlGaInP-based heterolaser in cw lasing mode at 293 K (cavity length L = 2000 μm and stripe width W = 5 μm).

$Ga_{0.51}In_{0.49}P$ is of type I within the entire range of compositions [19], while according to our calculations performed following [12], the heterojuction between $Al_xGa_{1-x}As$ and $Ga_{0.51}In_{0.49}P$ is of type II within the composition range $0.15 \le x \le 0.6$. Using the compositions in this range results in an additional loss of radiation. Moreover, the fabrication of such layers with a high aluminum content encounters a number of technological difficulties. First, it is not easy to ensure a sufficiently high concentration of the *n*-type impurity; second, the high activity of aluminum during the growth broadens the junction at the GaInP/GaAs boundary and, thus, impairs the quality of the laser structure. The lattice mismatch of the solid solutions used for the emitter and the waveguide layers with the substrate did not exceed $\Delta a/a = \pm 0.1\%$. The PL bands for $Ga_{0.51}In_{0.49}P$ and $(Al_xGa_{1-x})_{0.51}In_{0.49}P$ at room temperature peaked at 1.88 and 2.05 eV, respectively.

RESULTS

Laser heterostructures were grow on n^+-GaAs (100) substrates. Figure 3 shows the schematic arrangement of layers in the structure: the 0.5-μm-thick *n*-GaAs buffer layer, the 1-μm-thick *n*- and *p*-$(Al_{0.18}Ga_{0.72})_{0.51}In_{0.49}P$ emitter layers, undoped 0.3-μm-thick $Ga_{0.51}In_{0.49}P$ waveguide layers, the quantum well in a strained 100-*A*-thick $Ga_{0.74}In_{0.26}As_{0.53}P_{0.47}$, and the 0.3-μm-thick *p*-GaAs contact layer.

Mesa-stripe diode lasers with a stripe width W = 4–7 μm and the operation wavelength λ = 780 nm were fabricated from the separate-confinement laser heterostructures GaInAsP/GaInP/AlGaInP/GaAs. For the production of a mesa-stripe structure, we employed an Alcatel dry plasma etching setup. The mesa stripe was formed by etching a 10-μm-wide groove to the required depth in the passive region of the heterostructure. The depth was measured by a CamScan-S4-90FE electron scanning microscope using secondary electron microscopy. After the etching, an insulating SiO_2 layer of thickness d = 0.15 μm was deposited onto the passive region. Then, the *p*- and *n*-regions were coated with ohmic contacts of Au/Zn/Au and Au/Ge/Au, respectively. The diodes to be studied were mounted on a copper heat sink with their stripe contact down. The edges of the Fabry–Perot cavity were coated with SiO_2/Si dielectric mirrors. The output power attained in the continuous-wave (cw) mode of the lasers thus obtained was as high as 320 mW, and the lasing threshold was observed at I_{th} = 50 mA. The power–current characteristic is shown in Fig. 4.

CONCLUSIONS

In this study, we analyzed the compositions of an Al-free laser heterostructure emitting at a wavelength of about 780 nm.

Theoretical calculation of the band offsets between the Ga(In)AsP-based active region (λ = 770 nm) and the waveguide GaInP layer showed that the shallowest and the deepest electronic quantum wells are obtained in case of the ternary $GaAs_{0.77}P_{0.23}$ and the strained quaternary $GaAs_{0.77}P_{0.23}$ solid-solution layers, respectively. Photoluminescence data indicated that $Ga_{0.74}In_{0.26}As_{0.53}P_{0.47}$ is the most suitable material for the active region.

Based on the results of preliminary analysis, we formed GaInAsP/GaInP/AlGaInP laser heterostructures with a strained active region and an emission wavelength of 780 nm; these structures were then used for the production of mesa-stripe laser diodes. For the laser diodes with the stripe width W = 5 μm and cavity length L = 2 mm, the peak output power and threshold current were 320 mW and 50 mA, respectively.

ACKNOWLEDGMENTS

We thank A. I. Murashova and Z. N. Sokolova for fruitful discussion of the results.

This study was supported by the Russian Foundation for Basic Research (project nos. 01-02-17851 and 01-02-17842) and the interdisciplinary scientific and technological program of the Russian Federation "Physics of Solid-State Nanostructures."

REFERENCES

1. J. K. Wade, L. J. Mawst, D. Botez, and J. A. Morris, Electron. Lett. **34**, 1100 (1998).
2. A. Al-Muhanna, L. J. Mawst, D. Botez, *et al.*, Appl. Phys. Lett. **73**, 1182 (1998).
3. L. J. Mawst, S. Rusli, A. Al-Muhanna, and J. K. Wade, IEEE J. Sel. Top. Quantum Electron. **5**, 785 (1999).
4. R. Kudela and M. Morvic, Phys. Status Solidi A **95**, K1 (1986).
5. L. S. Vavilova, V. A. Kapitonov, A. V. Murashova, and I. S. Tarasov, Fiz. Tekh. Poluprovodn. (St. Petersburg) **34**, 1307 (2000) [Semiconductors **34**, 1255 (2000)].
6. W. E. Plano, K. S. Major, and D. F. Welch, IEEE Photonics Technol. Lett. **6**, 465 (1994).
7. T. Fukunaga, M. Wada, H. Asano, and T. Hayakawa, Jpn. J. Appl. Phys. **34**, L1175 (1995).
8. G. Erbert, F. Bugge, A. Knauer, *et al.*, IEEE J. Sel. Top. Quantum Electron. **5**, 780 (1999).
9. J. Sebastian, G. Beister, F. Bugge, *et al.*, IEEE J. Sel. Top. Quantum Electron. **7**, 334 (2001).
10. F. Agahi, K. M. Lau, H. K. Choi, *et al.*, IEEE Photonics Technol. Lett. **7**, 140 (1995).
11. N. Tansu, D. Zhou, and L. J. Mawst, IEEE Photonics Technol. Lett. **12**, 603 (2000).
12. M. P. C. M. Krijn, Semicond. Sci. Technol. **6**, 27 (1991).
13. R. E. Nahory, M. A. Pollack, W. D. Johnston, Jr., and R. L. Barns, Appl. Phys. Lett. **33**, 659 (1978).
14. S. Mukai, J. Appl. Phys. **54**, 2635 (1983).
15. E. Kuphal, J. Cryst. Growth **67**, 441 (1984).
16. N. A. Bert, L. S. Vavilova, I. P. Ipatova, *et al.*, Fiz. Tekh. Poluprovodn. (St. Petersburg) **33**, 544 (1999) [Semiconductors **33**, 510 (1999)].
17. S. Mukai, M. Matsuzaki, and J. Shimada, Jpn. J. Appl. Phys. **19**, L505 (1980).
18. M. Quillec, C. Daguet, J. L. Benchimol, and H. Launios, Appl. Phys. Lett. **40**, 325 (1982).
19. M. O. Watanabe and Y. Ohba, Appl. Phys. Lett. **50**, 906 (1987).

Translated by A. Sidorova

Semiconductors, Vol. 37, No. 12, 2003, pp. 1425–1427. Translated from Fizika i Tekhnika Poluprovodnikov, Vol. 37, No. 12, 2003, pp. 1477–1479.

PHYSICS OF SEMICONDUCTOR DEVICES

Picosecond High-Voltage Drift Diodes Based on Gallium Arsenide

A. V. Rozhkov* and V. A. Kozlov

Ioffe Physicotechnical Institute, Russian Academy of Sciences, Politekhnicheskaya ul. 26, St. Petersburg, 194021 Russia

**e-mail: rozh@hv.ioffe.rssi.ru*

Submitted July 8, 2003; accepted for publication July 14, 2003

Abstract—Experimental results of studying the dynamics of recovery of diodes based on lightly doped epitaxial layers of gallium arsenide are reported. The diodes under consideration belong to the class of drift diodes with step recovery and are designed to operate in circuits for shaping and generating picosecond pulses. The obtained values of the reverse-voltage recovery rate ($dU/dt \approx 2000$ V/ns) far exceed the published ultimate recovery rates for picosecond-response diodes with charge accumulation and are unprecedentedly high for step-recovery drift diodes. © *2003 MAIK "Nauka/Interperiodica".*

The possibility of using the fast drift mechanism for the recovery of blocking voltage was ascertained for the first time in studies of high-voltage silicon diodes [1]. At present, silicon drift step-recovery diodes (SRDs) are generally accepted as switching components in oscillator circuits that form nanosecond and subnanosecond kilovolt voltage pulses [2, 3]. In our opinion, there are good prospects for the use of other semiconductors with a wider band gap (compared to Si), a higher mobility of nonequilibrium charge carriers, and, consequently, a higher drift velocity for comparable values of electric-field strength. Recently, the first results of studying drift SRDs based on gallium arsenide [4] and silicon carbide [5] were reported. As far as we know, the smallest reported values of the blocking-voltage recovery time in drift SRDs are within the subnanosecond range. Until recently, the picosecond range of recovery times remained accessible only to diodes with charge accumulation and to the new generation of silicon drift SRDs [6].

Liquid-phase epitaxy from a confined solution (melt) of gallium arsenide in gallium was used as the base technology for growing the p^+–p^0–n^0–n^+ diode structures under investigation. The main efforts in using this technology were directed at the formation of fairly narrow *p*- and *n*-type regions (with a width of 1–10 μm) with an extremely low concentration of charge carriers at the boundary of the space-charge region (SCR). When fabricating the diode structures, we paid special attention to studying the effect of variations in the conditions of both the chemical treatment of the substrate and the thermal annealing of the solution–melt on the main electrical parameters of the *p*–*n* junction and its position in relation to the interface between the substrate and epitaxial layer. The ultimate electrical parameters of the diode structures were as follows: the highest blocking voltage $U_{p-n} = 220$ V; typical values of currents through the *p*–*n* junction when reverse-biased with a voltage ranging from 0 to $0.9U_{p-n}$ were $\lesssim 1$ μA at room temperature and $\lesssim 10$ μA at 200°C; the hole lifetime in the *n*-type base $\tau_p \approx 20$–60 ns; the concentration of residual impurities was $\lesssim 10^{14}$ and $\lesssim 5 \times 10^{15}$ cm^{-3} in the *p*–*n*-junction region and at the boundary of the n–n^+ regions, respectively; the thickness of the p^0- and n^0-type regions was $W_p \approx 3$–5 μm and $W_n \approx 5$–12 μm, respectively; and the capacitance of the *p*–*n* junction with an area of $S \approx 3 \times 10^{-4}$ cm^2 was $C_{p-n} \leq 2$ pF. The forward-biased diodes had fairly low differential resistances; the voltage drops across the diodes were $\lesssim 1.4$ V at a forward-current density of ~100 A/cm^2.

Dynamic parameters were measured in the mode of pulsed supply of the forward and reverse currents; this mode is typical of drift diodes. We used two of the known methods for feeding the forward current to the diodes. In the first method, the measurement circuit was designed so that the decay time of the forward current coincided very closely with the rise time of the reverse current. In this scheme of drift-SRD connection, the duration of the forward-current pulse could be varied from 2 to 10 ns and the pulse amplitude was varied in the range of several hundreds of milliamperes. In the other design of the measurement circuit, a controlled delay between the rise time of the reverse current and the decay time of the forward current was introduced. Characteristic values of the delay time ranged from 2 to 7 ns; the amplitude and width of the forward-current pulse were $I_f = 0.1$ A and $T_f = 1.0$ ns, respectively. In both schemes of drift-SRD connection, the charge Q that accumulated during the flow of forward current was equal to 0.1–5 nC by the time of the onset of the reverse-current rise.

Dispersal of the charge accumulated in the base begins at the second stage of diode-structure switching by the reverse current. The hole current through the

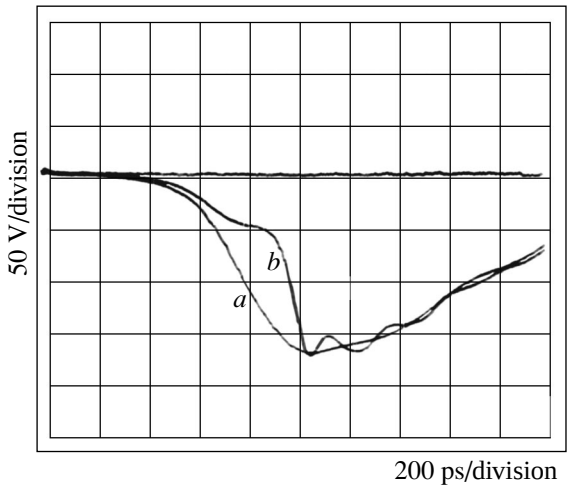

Oscilloscope patterns for (*a*) initial switching pulse and (*b*) the pulse formed across a 50-Ω load resistor during switching of a GaAs drift SRD.

p–*n* junction was controlled by the rise time of the reverse-current pulse. In our experiments, the shortest reverse-voltage rise time (T_r) was ~500 ps (see figure), which was much less than the hole lifetime (τ_p) in the base. Since the charge transported by the reverse current I_r in the drift SRDs under investigation is practically equal to the charge Q, the reverse-current amplitude at the instant of time T_0 when the hole concentration diminishes to zero is strictly controlled by the amplitude and width of the forward-current pulse or by the delay between the onset of the reverse-current rise and the onset of the forward-current decay. The recovery of the voltage across the formed space-charge region sets in at the instant of time T_0. The duration of the reverse-current decay corresponds to the rise time t_r of the voltage pulse formed across the load resistor.

The figure shows oscilloscope patterns of an initial switching pulse and a voltage pulse formed across a 50-Ω load resistor. These oscillograms indicate that the switching rates of drift SRDs are fairly high and the voltage rise times are unprecedentedly short for drift diodes. However, these rise times are consistent with the drift velocity v_n of charge carriers in the base; the largest values of v_n are limited by the saturation velocity $v_s = 10^7$ cm/s. The importance of the results obtained can be seen from the data listed in the table, where the main parameters of experimental GaAs drift SRDs and diodes with charge accumulation (SRDs) are given with the companies and institutes that manufactured them.

It is noteworthy that the absolute values of switching time t_r for GaAs drift SRDs are comparable with those of the best charge-accumulation diodes (SRDs) produced by well-known companies. GaAs drift SRDs are far superior to the aforementioned SRDs with respect to such parameters as the operating voltage and the voltage-rise rate dU/dt. The latter is most important when using such switches in the circuits of short-pulse modulators for ultrawideband electronics [2]. It is also worth mentioning that the operating temperatures of GaAs-based device structures are higher than those of Si-based structures. This consideration gives reason to hope that a higher pulse-repetition frequency will be attained while retaining a fairly high efficiency of generation of ultrashort pulses. At present, we can report as the first results the output parameters of pulsed oscillators that are fabricated on the basis of GaAs drift SRDs and feature pulse amplitudes as large as 600 V, pulse widths of $\leq$0.5 ns, and pulse-repetition frequencies as high as 1 MHz. A more detailed study of the efficiency and reliability of GaAs drift SRDs at higher pulse-repetition frequencies (including circuits connected in series) and the prospects for using these SRDs in practice is the subject of our future research.

Parameters of experimental GaAs- and Si-based drift step-recovery diodes (DSRDs) and diodes with charge accumulation (SRDs) (with indication of the manufacturer)

Manufacturer	Diode type	U_{p-n}^{br}, V	τ_p, ns	t_r, ps	Q, nC	dU/dt, V/ns
Hewlett Packard	SRD	25	25	75	0.3	330
Hewlett Packard	SRD	60	100	250	1.5	240
Alpha	SRD	45	25	200	0.8	225
Alpha	SRD	75	200	400	1.4	190
MACom	SRD	30	8	70	0.2	430
MACom	SRD	50	15	150	0.7	330
Ioffe Institute	GaAs DSRD	500	200	200	100	2500
Ioffe Institute	GaAs DSRD	220	40	100	2.5	2000
Ioffe Institute	Si DSRD	500	20000	500	800	1000
Ioffe Institute	Si DSRD	200	5000	200	9.0	1000

Note: U_{p-n}^{br} stands for the breakdown voltage.

ACKNOWLEDGMENTS

This study was supported in part by the Russian Foundation for Basic Research (project no. 02-02-08028) and ZAO Pulse Technologies.

We thank S.V. Zazulin and A.F. Kardo-Sysoev for their assistance in carrying out the experiments and for helpful comments when discussing the results obtained.

REFERENCES

1. I. V. Grekhov, V. M. Efanov, A. F. Kardo-Sysoev, and S. V. Shendereĭ, Pis'ma Zh. Tekh. Fiz. **9**, 435 (1983) [Sov. Tech. Phys. Lett. **9**, 188 (1983)].
2. A. F. Kardo-Sysoev, in *Ultra Wide Band Rada Technology*, Ed. by D. Taylor (CRC Press, Boca Raton, FL, 2001), Chap. 9.
3. V. A. Kozlov, I. A. Smirnova, S. A. Moryakova, and A. F. Kardo-Sysoev, in *Proceedings of 25th International Power Modulator Conference PMC 2002* (Hollywood, CA, 2002), p. 441.
4. V. I. Korol'kov, A. V. Rozhkov, and L. A. Petropavlovskaya, Pis'ma Zh. Tekh. Fiz. **27** (17), 46 (2001) [Tech. Phys. Lett. **27**, 731 (2001)].
5. I. V. Grekhov, P. A. Ivanov, A. O. Konstantinov, and T. P. Samsonova, Pis'ma Zh. Tekh. Fiz. **28** (13), 24 (2002) [Tech. Phys. Lett. **28**, 544 (2002)].
6. V. A. Kozlov, I. A. Smirnova, S. A. Moryakova, and A. F. Kardo-Sysoev, in *Book of Abstracts of the 13th International Conference CrimMiCo 2003* (Sevastopol, 2003).

Translated by A. Spitsyn

Semiconductors, Vol. 37, No. 12, 2003, pp. 1428–1429. Translated from Fizika i Tekhnika Poluprovodnikov, Vol. 37, No. 12, 2003, pp. 1480–1481.

PHYSICS OF SEMICONDUCTOR DEVICES

Impact-Ionization Wave Breakdown and Generation of Picosecond Pulses in the Ultrahigh-Frequency Band in GaAs Drift Step-Recovery Diodes

V. A. Kozlov*, A. V. Rozhkov, and A. F. Kardo-Sysoev

Ioffe Physicotechnical Institute, Russian Academy of Sciences, St. Petersburg, 194021 Russia

**e-mail: kozlov@mail.ioffe.ru*

Submitted July 17, 2003; accepted for publication July 18, 2003

Abstract—It is shown experimentally for the first time that the operation of GaAs drift step-recovery diodes produced on the basis of p^+–p^0–n^0–n^+ is accompanied by the generation of ultrahigh-frequency oscillations in the form of trains of short pulses with a duration of ~10 ps. The amplitude and repetition frequency of these pulses are as high as ~100 V and ~(10–100) GHz, respectively. The phenomena of delayed reversible wave breakdown and excitation of ultrahigh-frequency oscillations in the structures of GaAs step-recovery diodes are found to open up new avenues for progress both in the physics and technology of semiconductor devices based on GaAs structures and in the technology of ultrahigh-frequency systems and devices that deal with pulsed signals of picosecond-scale duration. © *2003 MAIK "Nauka/Interperiodica".*

Kozlov *et al.* [1] were the first to report the phenomena of delayed impact-ionization wave breakdown in high-voltage silicon p^+–n–n^+ structures of drift step-recovery diodes (DSRDs) and the excitation of microwave oscillations in these diodes, which are typical of an avalanche transit-time diode operating in the impact avalanche and transit time (IMPATT) mode. The main special feature of microwave oscillations in the structures under consideration is the method of generating these oscillations. In this method, the structure of the diode is forced into the mode of avalanche-breakdown microwave oscillations due to an abrupt (over a period of 10^{-9} s) recovery of the blocking properties of the diode that operates in the DSRD mode rather than due to an external pulse source (as is the case for conventional avalanche diodes). In subsequent studies, we managed to initiate microwave oscillations for the IMPATT mode in various Si DSRD structures that differed in the response speed and parameters of their layers, which made it possible to excite microwave oscillations in the frequency range from hundreds of megahertz to several gigahertz. Independent studies [2] have shown that similar microwave oscillations can also be obtained for diodes based on silicon-on-sapphire (SOS) structures in a mode similar to the DSRD mode in the case of abrupt recovery of p^+–p^0–n^+ junctions without a base n^0-type layer. Attempts to attain the trapped plasma avalanche transit-time (TRAPATT) mode of delayed impact-ionization breakdown in the structure of SOS diodes failed [2].

In this paper, we report the results of experimental observation and study of the phenomena of delayed wave breakdown and excitation of microwave oscillations in the IMPATT and TRAPATT modes in DSRD structures based on gallium arsenide. Since gallium arsenide differs from silicon not only in energy-band structure but also in the type of field dependence of the charge-carrier mobility (a nonmonotonic dependence with a maximum), it was assumed that TRAPATT oscillations at frequencies higher than 10 GHz can be excited in GaAs diode structures operating in the DSRD mode. Excitation of TRAPATT oscillations in silicon DSRDs appeared to be impossible despite the fact that the possibility of reversible delayed wave breakdown in silicon DSRD structures was verified experimentally [1].

In our experiments aimed at revealing the existence of IMPATT and TRAPATT oscillations in DSRDs based on GaAs, we used high-voltage drift diode structures with a picosecond-scale response speed [3]. The p^+–p^0–n^0–n^+ structures were tested using a pulse-actuated circuit designed for the formation of bell-shaped picosecond-scale electrical pulses with the rise time corresponding to the response speed of the DSRD structure. In order to attain the necessary modes of the charge-carrier injection and extraction in GaAs-based DSRD structures, we employed circuitry based on the use of drift step-recovery silicon transistors as the primary switches; these transistors ensured a high efficiency and a high-frequency response of circuits for generating picosecond-scale electrical pulses.

Figure 1 shows oscilloscope traces of electrical pulses generated by a GaAs DSRD in the following three modes: (1) generation of picosecond monopulses with the DSRD operating without avalanche breakdown in the p^0–n^0 junction of the structures (Fig. 1a, curves *1*); (2) generation of microwave oscillations in the IMPATT mode at a frequency of ~6 GHz (Fig. 1a,

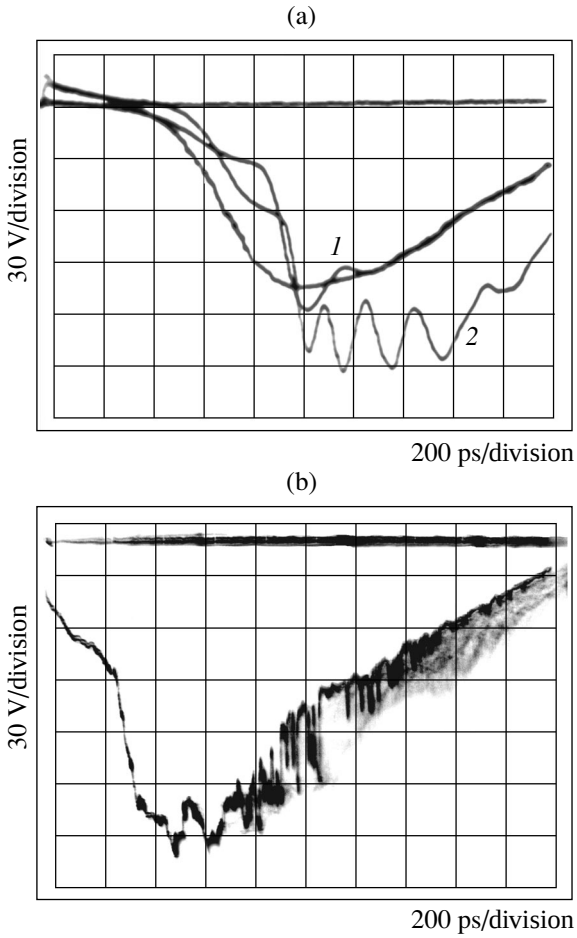

Fig. 1. The shape of pulses generated by GaAs DSRDs: (a) (*1*) monopulses with a picosecond-scale duration in the mode without avalanche breakdown of the p^0–n^0 junction and (*2*) microwave oscillations in the IMPATT mode at a frequency of ~6 GHz; (b) microwave oscillations in the TRAPATT mode at a frequency of ~50 GHz.

curve *2*); and (3) generation of microwave oscillations in the TRAPATT mode at a frequency of ~50 GHz (Fig. 1b). It is noteworthy that the microwave oscillations were recorded using a stroboscopic oscilloscope to trace the shape of the voltage pulse across the 50-Ω load resistor. The parasitic inductance and capacitance of both the measurement circuit and the DSRD power supply itself were designed so that we could detect the processes with a time resolution of ~50 ps. In this context, we could not estimate with confidence the amplitude of microwave oscillations in the TRAPATT mode; we plan to perform additional measurements in the mode of direct (nonstroboscopic) detection of microwave processes in a microwave cavity.

Thus, we studied several variants of operation of GaAs-based DSRDs with a picosecond-scale response speed under conditions of avalanche impact-ionization breakdown of the p^0–n^0 junction. We ascertained for the first time that these DSRDs can be used for the generation of microwave power in a frequency range from several gigahertz to several tens of gigahertz; we showed that the mode of TRAPATT oscillations is attainable for GaAs diodes with step recovery, in contrast to what is observed in Si structures. We do not claim that the results obtained offer an adequate theoretical explanation for the microwave effects observed; rather, the interpretation of the microwave oscillations is qualitative, especially in the case of the TRAPATT mode with DSRDs based on wave delayed impact–ionization breakdown of GaAs. Nevertheless, the results obtained in this study make it possible to conclude with a degree of confidence that DSRDs based on GaAs structures can be used with good results to generate high-power high-voltage electrical and optical signals with a picosecond-scale duration. The generation of high-power picosecond-scale electrical and optical monopulses will be verified experimentally using methods similar to those described by Alferov *et al.* [4–6].

This study was supported in part by the Russian Foundation for Basic Research (project no. 02-02-08028, “Innovations”) and by ZAO Pulse Technologies.

We thank S.V. Zazulin for help in performing the experiments to test the characteristics of microwave oscillations in DSRDs based on GaAs and I.A. Smirnova for her assistance at certain stages of preparation of the samples.

REFERENCES

1. V. A. Kozlov, A. F. Kardo-Sysoev, and V. I. Brylevskiĭ, Fiz. Tekh. Poluprovodn. (St. Petersburg) **35**, 629 (2001) [Semiconductors **35**, 608 (2001)].
2. S. A. Darznek, S. K. Lyubutin, S. N. Rukin, and B. G. Slovikovskiĭ, Fiz. Tekh. Poluprovodn. (St. Petersburg) **36**, 629 (2002) [Semiconductors **36**, 599 (2002)].
3. A. V. Rozhkov and V. A. Kozlov, Fiz. Tekh. Poluprovodn. (St. Petersburg) **37**, 1477 (2003) [Semiconductors **37**, 1425 (2003)].
4. Zh. I. Alferov, V. M. Efanov, Yu. M. Zadiranov, *et al.*, Pis’ma Zh. Tekh. Fiz. **12**, 1281 (1986) [Sov. Tech. Phys. Lett. **12**, 529 (1986)].
5. Zh. I. Alferov, I. V. Grekhov, V. M. Efanov, *et al.*, Pis’ma Zh. Tekh. Fiz. **13**, 1089 (1987) [Sov. Tech. Phys. Lett. **13**, 454 (1987)].
6. Zh. I. Alferov, E. L. Portnoĭ, A. B. Zhuravlev, and N. N. Stel’makh, Pis’ma Zh. Tekh. Fiz. **12**, 1093 (1986) [Sov. Tech. Phys. Lett. **12**, 452 (1986)].

Translated by A. Spitsyn

Semiconductors, Vol. 37, No. 12, 2003, p. 1430. Translated from Fizika i Tekhnika Poluprovodnikov, Vol. 37, No. 12, 2003, p. 1482.

PERSONALIA

Vladimir Idelevich Perel'
(On His 75th Birthday)

Recently, Vladimir Idelevich Perel', an outstanding scientist and wonderful person—our friend, teacher, and colleague—celebrated his 75th birthday. V.I. Perel' is a winner of the State Award, a full member of the Russian Academy of Sciences (RAS), the head of the department of the theory of optical and electrical phenomena in semiconductors, and the editor-in-chief of the journal Fizika i Tekhnika Poluprovodnikov. He has worked for almost half a century at the Ioffe Physicotechnical Institute, RAS. His studies in the field of quantum kinetics, plasma waves in metals, and spin polarization and recombination phenomena in semiconductors are widely known and recognized in the scientific community worldwide.

Perel' has been teaching for about 30 years at the St. Petersburg Electrotechnical University. His students give lectures in Russia, USA, France, Israel, Germany, Norway, and other countries. However, it is not only those that have attended his brilliant lectures that consider Perel' to be a teacher. It is difficult to find a researcher in the field of solid-state physics at the Ioffe Physicotechnical Institute who would not ask Perel' for help or advice. His encyclopedic knowledge, brilliant scientific intuition, extraordinary ability to understand a new problem rapidly and well and suggest a way of solving it, and his exceptional benevolence and sense of humor make communication with Perel' very pleasant and memorable. One cannot help wishing to meet him again and again.

His irreproachable reputation, high moral qualities, and worldly wisdom has won Perel' universal admiration and respect.

We congratulate Perel' on the occasion of his birthday and wish him happiness, good health, and the love of all those who are dear to him.

Friends, colleagues, and students

Editorial Board of the journal
Fizika i Tekhnika Poluprovodnikov

Translated by A. Spitsyn

1063-7826/03/3712-1430$24.00